Modelling of Metal Nanoimprinting

Proefschrift

ter verkrijging van de graad van doctor
aan de Technishe Universiteit Delft,
op gezag van de Rector Magnificus prof. ir. K.C.A.M. Luyben,
voorzitter van het College voor Promoties,
in het openbaar te verdedigen op maandag 19 mei 2014 om 10:00 uur

door

Yunhe ZHANG

Master of Science in Solid Mechanics,
Zhejiang University, China.

geboren te Tianjin, China

Dit proefschrift is goedgekeurd door de promotor:
Prof. dr. B.J. Thijsse

Copromotor:
Dr. ir. L. Nicola

Samenstelling promotiecommissie:

Rector Magnificus,	voorzitter
Prof. dr. B.J. Thijsse,	Technische Universiteit Delft, promotor
Dr. ir. L. Nicola,	Technische Universiteit Delft, copromotor
Prof. dr. S. Qu,	Zhejiang University
Prof. dr. ir. P.R. Onck,	Rijksuniversiteit Groningen
Prof. dr. A. Fasolino,	Radboud University Nijmegen
Prof. dr. ir. T.J.H. Vlugt,	Technische Universiteit Delft
Prof. dr. ir. A.S.J. Suiker,	Technische Universiteit Eindhoven
Prof. dr. ir. J. Sietsma,	Technische Universiteit Delft, reservelid

ISBN 978-94-6259-206-3

cloudycrane@gmail.com

Content

Chapter 1

Introduction

1.1 General introduction

Imprinting is a fabrication technique used in the electronic industry to create patterns on a substrate. These patterns are geometric shapes that make up part of the electronic device, see Fig. 1.1. Traditionally, patterning of metal is achieved by complex lithographic processes that require several steps to reach the final shape. Lithography makes use of photons or electrons to modify the properties of a polymer resist, thus exposing parts of the underlying metal. The exposed metal is then etched away. With increasing miniaturization, the last years have witnessed a growing demand for pushing feature sizes below the optical diffraction limits, forcing the lithographers to use shorter wavelengths and extremely costly optical systems. As an alternative, a technology called nanoimprint lithography has been recently investigated (Guo, 2007; Schift, 2007). Nanoimprint lithography involves pressing a stamp or template into a compliant layer, typically a thin polymer film whose structure can be thermally or chemically solidified to retain the pattern from the template. But, also this technique, requires several processing steps and etching of the metal.

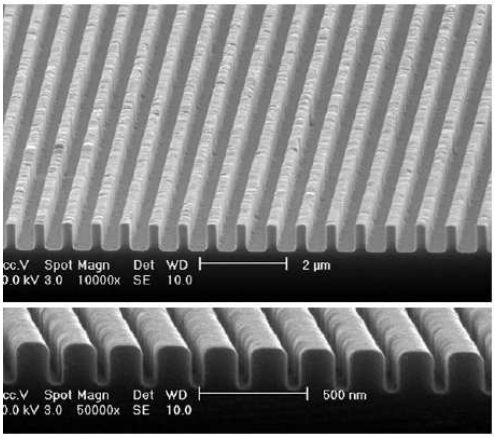

Figure 1.1. Examples of imprinted structures obtained by lithographic processes, from (Guo, 2007).

The process discussed in this thesis is similar to nanoimprint lithography but the essential difference is that the imprinting is made directly onto the metal instead of onto a polymer or photoresist. The basic idea is that a pattern on a rigid punch is transferred onto a metal specimen by plastic deformation of the metal itself (see Fig. 1.2).

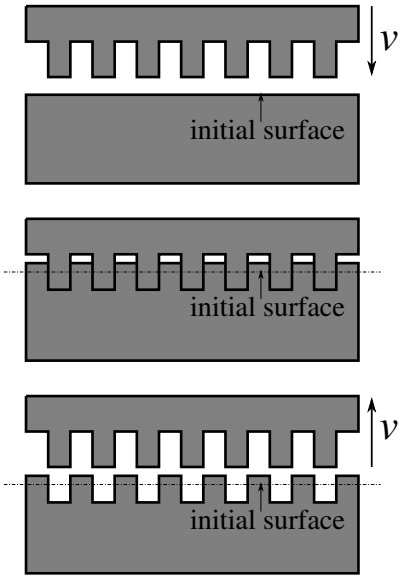

Figure 1.2. A schematic drawing showing direct nanoimprinting.

Several electronic devices make use of patterned metal layers. This is for instance the case of gratings for optical components like polarizers, polarization beam splitters and optical isolators (Ahn et al., 2005; Schnabel et al., 1999; Yu et al., 2001), microscale electromagnetic relays (Williams and Wang, 2004) and microchannel heat exchangers (Mei et al., 2008). Direct metal nanoimprinting is potentially an attractive technology for these and new other devices because it is a cost-effective and simple single step process that does not require etching and therefore does not require mask making and alignment.

Metals like copper and gold are difficult to dry-etch. Wet-etching processes are not very reproducible, because of chemical diffusion between exposed and unexposed portions of the resist and have the major disadvantage that they cannot be applied to non-planar structures. On the contrary, mechanical metal imprinting can be used at any indentation angle, even on curved surfaces, making it an interesting technology for 3D structures and roll-to-roll production.

The aim of this study is to understand, by conducting computer simulations, if it is possible to use direct imprinting to obtain reproducible patterns that closely resemble the shape of the template. The targeted size of the patterns in this work ranges from a micrometer to a few nanometers. The resolution that can be achieved with this technique is an important matter

of investigation: plastic deformation in the imprinted layer is expected to be far from homogeneous. The stress induced by the template is highly localized and plasticity is initiated and sustained by discrete carriers, dislocations, that glide on specific slip planes. Stochastics related to the exact location where dislocation appear are expected to play an increasingly important role when the size of the imprints is reduced.

In order to be able to correctly describe plasticity at the submicron scale our numerical analysis cannot rely on conventional finite element simulations based on classical continuum plasticity. The shortcoming of classical plasticity is that its formualtion does not contain a material length scale and therefore cannot predict the experimentally obsereved size depedent plastic behavior. We therefore use discrete dislocation plasticity simulations to analyse imprinting for patterns with features of a few hundred nanometers and molecular dynamics simulations for features of a few nanometers. Both numerical model contain the characteristic length scale of plasticity, the dislocation Burgers vector, and are therefore appropriate to capture possible size dependencies.

MD is suited to study nucleation of defects but can handle only very small size and time scale, while discrete dislocation plasticity is capable of tracking dislocation motion in a larger sample and for a longer time, making a comparison with experimental work possible (see first chapter).

1.2 Outline of thesis

This thesis consists of a general introduction and six chapters, organized as follows:

Chapter 2 is a comparison between direct nanoimprinting experiments and dislocation dynamics simulations. In the experiment, performed by our collaborators, a gold single crystal is imprinted by a tungsten indenter patterned with parallel lines. Dedicated dislocation dynamics simulations give insight on the plastic deformation occurring into the crystal during imprinting and help to identify the limitations of the experiments.

Chapter 3 focuses on the role of the interface between an imprinted metal film and the substrate on which it is deposited. The two limiting situations of a perfectly penetrable and impenetrable interfaces are investigated using discrete dislocation plasticity simulations. Deeper and better defined imprints are obtained when the interface is capable to absorbe dislocations.

The effect of template shape on imprinting is explored in Chapter 4 also by means of discrete dislocation plasticity simulations. To this end, metal thin films are imprinted by a rigid template, made of an array of equispaced

indenters of various shape, i.e. rectangular, wedge and circular. For a fair comparison the geometry of the indenters is chosen such that the contact area is approximately the same at final imprinting depth. Results show that for all template shapes the final patterns strongly depend on the local dislocation activity.

The possibility of obtaining a reproducible pattern with features of a few nanometers, is analysed in Chapter 5 using molecular dynamics simulations. The majority of the simulations show an unexpected competition between crack formation and dislocation plasticity upon retraction of the template, that leads in some cases to an imprint and in other cases to a flat surface.

Chapter 6 is about nanoindentation by a single wedge indenter and the related lattice rotation fields. Through discrete dislocation plasticity simulations we try to understand how the fields are affected by the density of dislocation sources and obstacles and whether there is a correspondence between the lattice rotation fields and the material hardness.

Chapter 7 has a different focus compared to previous chapters: it deals with the plastic behavior of a rough metal surface during contact loading. As previously mentioned a rough surface is obtained when a flat metal layer is imprinted. The imprinted metal is then flattened and its plastic behavior is compared to that of a metal layer with an identical surface but cleared of dislocations and residual stress fields before flattening. The goal of this study is to investigate the effect of loading history on the evolution of surface roughness during contact loading.

References

Ahn, S.W., Lee, K.D., Kim, J.S., Kim, S.H., Lee, S.H., Park, J.D., Yoon, P.W., 2005. Fabrication of subwavelength aluminum wire grating using nanoimprint lithography and reactive ion etching. Microelectron. Eng. 78-79, 314–318.

Guo, L., 2007. Nanoimprint lithography: Methods and material requirements. Adv. Mater. 19.

Mei, F., Parida, P.R., Jiang, J., Meng, W.J., Ekkad, S.V., 2008. Fabrication, assembly, and testing of Cu- and Al-based microchannel heat exchangers. J. Microelectromech. Syst. 17, 869–881.

Schift, H., 2007. Nanoimprint lithography: An old story in modern times? a review. J. Vac. Sci. Technol. B 26, 458–480.

Schnabel, B., Kley, E., Wyrowski, F., 1999. Study on polarizing visible light by subwavelength-period metal-stripe gratings. Opt. Eng. 38, 220.

Williams, J.D., Wang, W., 2004. Microfabrication of an electromagnetic power relay using SU-8 based UV-LIGA technology. Microsyst. Technol. 10, 699–705.

Yu, Z., Wu, W., Chen, L., Chou, S.Y., 2001. Fabrication of large area 100 nm pitch grating by spatial frequency doubling and nanoimprint lithography for subwavelength optical applications. J. Vac. Sci. Technol., B 19, 2816–2819.

Chapter 2

Nanoimprinting of single crystalline gold: experiments and dislocation dynamics simulations

Abstract

This paper addresses the feasibility of direct nanoimprinting and highlights the challenges involved in this technique. Our study focuses on experimental work supported by dislocation dynamics simulations. A gold single crystal is imprinted by a tungsten indenter patterned with parallel lines of various spacings. Dedicated dislocation dynamics simulations give insight in the plastic deformation occurring into the crystal during imprinting. We find that good pattern transfer is achieved when the lines are sufficiently spaced such that dislocation activity can be effective in assisting deformation of the region underneath each line. Yet, the edges of the obtained imprints are not smooth, partly due to dislocation glide.

2.1 Introduction

Direct metal nanoimprinting is of great technological interest due to its potential applications in miniaturized systems. Micro-devices made of metal possess advantages in specific applications as compared to the more common silicon based microelectromechanical systems (MEMS). It is for instance the case of gratings for optical components like polarizers, polarization beam splitters and optical isolators (Ahn et al., 2005; Schnabel et al., 1999; Yu et al., 2001), microscale electromagnetic relays (Williams and Wang, 2004) and microchannel heat exchangers (Mei et al., 2008). The latter, for instance, promise much better thermal and mechanical performances than silicon-based devices, but the technique to produce them is still at its early stages. While the most common technique to achieve nanoimprints is lithography (Guo, 2007; Schift, 2008), imprinting by mechanical indentation of the metal film has recently been suggested as a promising alternative approach (Buzzi et al., 2008; Cross et al., 2007; Lister et al., 2004; Yao et al., 2008). This technique consists of transferring a pattern on a rigid punch onto the metal specimen by plastically deforming the metal. What makes metal nanoimprinting attractive is that it is a single-step process. This means that it is highly cost effective and has the potential of being applicable for large-scale production of multilayer structures,

This chapter is published as:
J. Zhang, Y. Zhang, N.A. Mara, J. Lou, L. Nicola. Direct nanoimprinting of single crystalline gold: experiments and dislocation dynamics simulations, Appl. Surf. Sci. 290 (2014) 301-307

for which reducing the number of steps is a highly desirable asset. An additional reason for seeking an alternative approach to lithography is that metals like copper and gold are difficult to be dry-etched. Wet-etching processes have major disadvantages when applied to non-planar structures. Conversely, mechanical metal imprinting can be used at any indentation angle, even on curved surfaces, making it an interesting technology for 3D structures.

An important feature of nanoimprinting experiments is that the material around the imprinted area tends to either pile-up or sink-in with respect to the indented surface area (Alcalà et al., 2000; Nix, 1997; Pharr et al., 1992). Strain hardening near the indenter tip will cause plastic deformation to occur further and further away from the contact, causing material to be displaced far away from the indentation and resulting in sink-in behavior. By contrast, strain-hardened materials and metallic glasses that exhibit a low strain-hardening rate will deform more locally, creating a pile-up of materials against the sides of the indenter. Various authors have observed this phenomenon for many single crystals, such as Cu, W, Fe, Al, Ni, Ag and Au. Distinct pile-up patterns occur only in certain directions around the indent depending on the crystallographic orientation of the single crystal (Bouvier and Needleman, 2006; Flom and Komanduri, 2002; Gaillard et al., 2003; Tymiak et al., 2001; Zong and Soboyejo, 2005). These studies revealed a strong influence of the crystal orientation on the formation of surface patterns, which needs to be considered when performing nanoimprinting experiments.

In any case, it is well accepted that plastic deformation in metals hinges on dislocation formation, dislocation storage, and dislocation interaction. The responsible mechanisms for the onset of plastic deformation during nanoindentation are believed to be triggered by nucleation of dislocations, as confirmed by atomic and continuum simulations and analyses (Engels et al., 2012; Gao and Lou, 2008; Miller and Rodney, 2008). The theory of strain gradient plasticity has been widely used to explain the well reported indentation size effects (Abu Al-Rub and Voyiadjis, 2004; Lou et al., 2006; Nix and Gao, 1998), although a bi-linear behavior was shown to describe the indentation size effects between the micro- and nano-scales (Zong et al., 2006). However, strain gradient plasticity theories cannot capture size dependence arising from source limited plasticity or from dislocation starvation (Greer and Nix, 2006). Source limited plasticity is likely to play an essential role in direct metal nanoimprinting (Choi et al., 2003) because the size of the indenter, as well as the spacing between indenters, are comparable with the average spacing of dislocation sources in the metal. Locally underneath the indenter the stress concentration might be very high, but if no dislocation source is in the vicinity, dislocations

will not be nucleated and plastic flow will not be able to reduce the stress. Discrete dislocation plasticity is a modeling technique that can capture size dependence occurring not only from geometrically necessary dislocations and boundary constraints (Balint et al., 2008; Cleveringa et al., 1999; Nicola et al., 2003) but also from limited dislocation sources (Nicola et al., 2006; Senger et al., 2008). Nicola *et al* (Nicola et al., 2006) have demonstrated that not only qualitative, but also good quantitative agreement can be reached when comparing experiments and dislocation dynamics for the tensile loading of freestanding thin films.

In this paper we will address the feasibility of direct nanoimprinting of gold single crystal and highlight the challenges involved in this technique. Our study involves experimental work as well as dedicated dislocation dynamics simulations. The experiments are carried out by imprinting a gold single crystal with a tungsten indenter patterned with parallel lines of various width.

The purpose of performing the numerical simulations is twofold:

- idealize the experiment for a simpler interpretation of the results: in the simulations the metal has an initial flat surface, the template is rigid and the flat indenters are perfectly aligned with the metal surface. This cannot be achieved by the experiments, where the metal surface is rough, the indenter bends of an unknown quantity and the alignment during indentation cannot be controlled;

- assess to what extent source limited plasticity and size-dependent plasticity are a limitation to pattern transfer.

2.2 Experiments

2.2.1 Sample preparation and experimental procedures

One 3 mm side length single crystal gold cube (READE ADVANCED MATERIALS, Reno, NV) with all faces electro-polished was used in this study. All faces are (100) orientation, and root mean square (RMS) surface roughness was measured to be ~25.94 nm measured by atomic force microscopy (Agilent Technologies Picoplus 5500 AFM, Tempe, Arizona). The sample was chosen because of the absence of surface oxide and the weak crystalline orientation dependence of pile-up in Au crystals (Zong and Soboyejo, 2005).

The nanoimprinting process employed in this work is similar to the indentation with a flat punch. The nanoimprinting die was fabricated by focus ion beam (FIB) machining as described below. An electrochemical pre-etched tungsten wire (200 μm in diameter originally) with a sharp tip was further

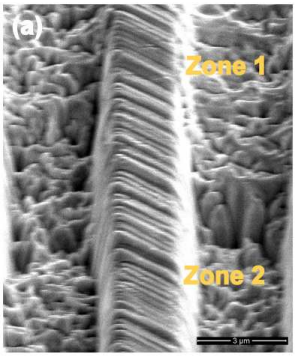

Figure 2.1. SEM image of the FIB machined tungsten nanoimprinting die.

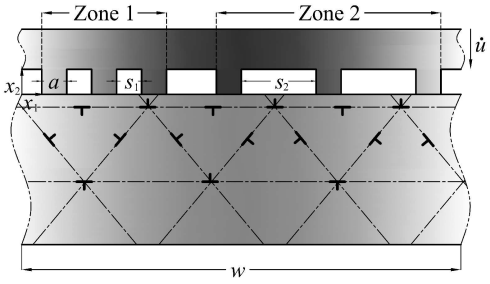

Figure 2.2. Sketch of the gold single crystal imprinted by a rigid die with line patterns spaced differently.

truncated on the tip, yielding a circular flat punch (60 μm in diameter). On the flat area, a rectangular block was created by FIB milling followed by machining of fine line patterns on the block. As shown in Figure 2.1 the surface of the block contained several parallel lines spaced at a few hundred nanometers that act as nanoimprinting die in our experiment. The exact dimensions of those lines were measured by scanning electron microscopy (SEM) and reported in Tab. 2.1. It is thus possible to identify two different zones in the line pattern: in Zone 1 the spacing s between lines is smaller (110 ± 8 nm) and in Zone 2 it is greater, i.e. 1414 ± 95 nm, while the line width a is comparable in both zones (see Figure 2.2).

The nanoimprinting experiments were performed at room temperature using a TI 900 TriboIndenter (Hysitron Inc, Minneapolis, MN) with self-

Table 2.1. The dimensions of the lines on the indenter head

	a (nm)	s (nm)
Zone 1	122 ± 12	110 ± 8
Zone 2	165 ± 13	1414 ± 95

machined nanoimprinting die. The TriboIndenter, which combines an *in-situ* scanning probe microscopy (SPM) head together with indentation capabilities enables quasi-static nanoindentation experiments with subsequent *in-situ* SPM imaging at the same location. The *in-situ* images could be obtained on the sample surface to allow for pre- and post-testing characterization of the material surface within tens of nanometers of the desired testing location. The indentation experiments were performed using the following procedure: the gold single crystal was first loaded to a pre-set maximum load level in 20 s, and then it was unloaded at the same rate. The load control mode was used to execute 9 nanoindentation cycles at different positions, while for each loading-unloading cycle the maximum load increased from 10^3 μN to 10^4 μN. Such experiments were repeated several times at different locations on Au single crystal surface. After each nanoindentation experiment, the resulted parallel groove features were carefully evaluated using the contact mode SPM scan and corresponding image analysis.

2.2.2 Experimental results

A typical SPM topography image of the imprinted gold crystal at a maximum load of $\sim 10^4$ μN is shown in Figure 2.3. The imprinted groove depth was evaluated at four different locations as indicated by the line depth profile shown in the inset of Figure 2.3. The choice of four line scans on the same imprinted pattern is to account for any possible misalignment between substrate and the nanoimprinting die. As shown in Figure 2.3, the depth profiles and the SPM topography image demonstrate a clear difference in the pattern transfer obtained by closely spaced lines (Zone 1) and widely spaced lines (Zone 2). The lines in Zone 1 seem to have produced a single large imprint on the Au substrate, although some features of small impression can also be seen possibly due to surface roughness of the die. The lines in Zone 2 with substantially larger spacing produced much more distinguishable discrete imprints in the gold crystal. It is worth noting that the imprinted grooves in both Zone 1 and 2 appeared at the same loading cycle, although Zone 1 impression depths are still generally deeper than Zone 2 impressions (Figure 2.3). This nanoimprinting behavior, consistently observed in our repeated experiments, is designated as

Type 1 behavior. In contrast, in other experiments a single large imprint on

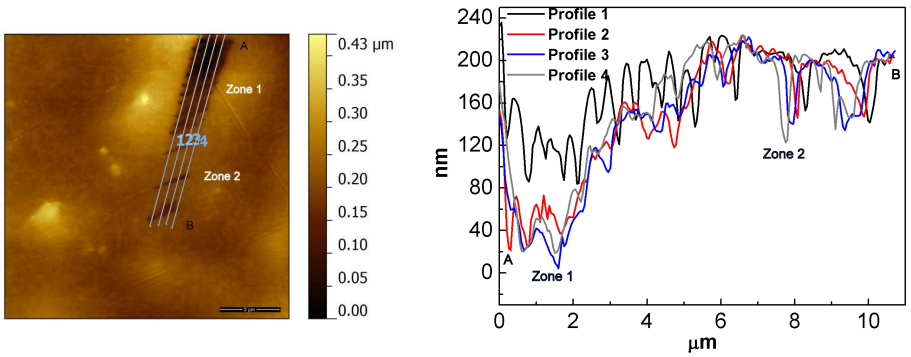

(a) (b)

Figure 2.3. (a) SPM image of the imprinted grooves on Au (100) single crystal, line profiles were collected at four different locations as shown by the lines 1-4. (b) The line profiles are designated as Type 1 behavior.

Au substrate appeared first in Zone 1, followed at a higher loading by the appearance of the clearly distinguishable discrete imprints in Zone 2. This resulted in a more pronounced difference in imprinted features between Zone 1 and Zone 2 as shown in Figure 2.4. It is very clear from the line scan profile shown in the inset of Figure 2.4 that the large imprint in Zone 1 is considerably deeper than discrete imprints in Zone 2. Such kind of behavior was repeatedly observed and is defined as Type 2 behavior in our experiments. Furthermore, there is oftentimes an upward extrusion of displaced gold known as material pile-up around the edge of the whole indentation area judging from the 3D SPM profile of the indentation site. On the other hand, there is also a tendency for the gold to be depressed between the two indentation zones, this behavior is known as sink-in behavior. Such phenomena have been observed for both Type 1 and Type 2 behaviors.

Finally, it is very important to point out a few non-negligible factors in the experiments: 1) the height of the line patterns on the die are not always constant, i.e. the line heights in Zone 1 might be larger than those in Zone 2. This can be one possible reason for which the imprints produced by Zone 1 are deeper than those produced by Zone 2 (see Figure 2.3 and 2.4); 2) the nanoimprinting die surface is likely to be not perfectly parallel but slightly tilted with respect to the top surface of the gold single crystal. The tilting can occur during assembly of the W wire into the plastic holder. As a consequence

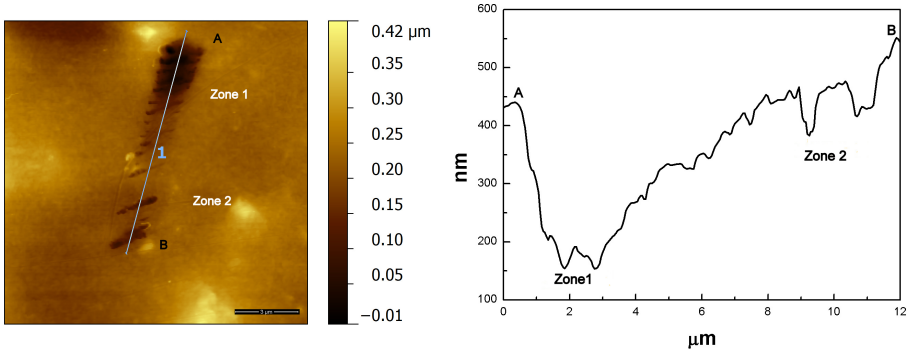

(a) (b)

Figure 2.4. (a) SPM image of the imprinted grooves for cross sectioning. (b) The line profiles are designated as Type 2 behavior.

of the misalignment the imprinting process is more likely to be edge indentation rather than surface indentation. The profile in Figure 2.4 indeed is rather skew and it is probably produced by a tilted template. These factors highlight the difficulties and limitations associated with the direct nanoimprinting experiments. To have a better mechanistic understanding of the underlying process, direct comparison to dislocation dynamic simulations is clearly desirable as will be described in details in the next section. Nonetheless, from our experimental observations it is obvious that imprinting patterns with spacing around or less than 100 nm will be quite challenging if not impossible, while imprints with spacing in the order of 1 μm could be achieved.

2.3 Modeling

2.3.1 Problem formulation

Simulations are carried out to model the ideal imprinting of a gold single crystal by a rigid template with lines of constant width $a = 200$ nm but different spacing (see Figure 2.2). Similarly to the experiment, two zones can be identified in the template: in Zone 1 the lines are spaced at $s_1 = 200$ nm and in Zone 2 the lines are spaced at $s_2 = 1400$ nm. The height of the crystal in the simulations is $h = 10$ μm. The choice of a small crystal height is motivated by the intention of limiting the elastic deformation of the crystal, that does not contribute to form retained imprints, and of focusing on

Table 2.2. A list of parameters used in the simulation.

$\dot{u}$ (m/s)	dt (ns)	τ_{nuc} (MPa)	t_{nuc} (ns)	τ_{obs} (MPa)	B (Pa$\cdot$s)	b (nm)
0.02	0.5	50	10	150	0.0001	0.25

obtaining plastic deformation and residual strain. The elastic properties of the gold crystal are described by its Young's modulus, $E = 78$ GPa, and Poisson's ratio, $\nu = 0.44$. The analysis is performed on a periodic unit cell of width $w = 10$ μm containing six contacts. Imprinting is performed by prescribing an increasing displacement, $\dot{u} = 0.02$ m/s, at the contacts. The rest of the surface which is initially perfectly flat remains traction free during the simulation, i.e.:

$$u_1(x_1, 0) = 0, \quad u_2(x_1, 0) = \dot{u}t \quad \text{if} \quad x_1 \in A_{\text{contact}} \tag{2.1}$$

$$\sigma_{12}(x_1, 0) = 0, \quad \sigma_{22}(x_1, 0) = 0 \quad \text{if} \quad x_1 \notin A_{\text{contact}} \tag{2.2}$$

where A_{contact} is the contact area.

The template is assumed to stick perfectly to the gold crystal. The crystal contains three sets of parallel slip planes oriented at 0° and ±60° with the x_1-axis, and is indented along the [001] direction, which corresponds to the x_2-axis. The slip planes are spaced at $100b$, where $b = 0.25$ nm is the dislocation Burgers vector. Point sources and obstacles are randomly placed on the slip planes. Dislocation dipoles nucleate from a point source when the resolved shear stress on the source is larger than its critical strength $\tau_{\text{nuc}} = 50$ MPa for a certain time span $t_{\text{nuc}} = 10$ ns. After nucleation the dislocations glide on their slip planes with

$$v = f_I/B, \tag{2.3}$$

where f_I is the Peach-Koehler force acting on dislocation I and $B = 0.0001$ Pa$\cdot$s is the drag coefficient. The moving dislocations can be pinned at an obstacle, if the resolved shear stress they experience is lower than the critical strength of the obstacle, τ_{obs}. The strength of the sources is taken to have a Gaussian distribution with average value $\tau_{\text{nuc}} = 50$ MPa and standard deviation 10 MPa; the critical strength of the obstacles is taken to be $\tau_{\text{obs}} = 150$ MPa. More details on the formulation can be found in Nicola *et al* (Nicola et al., 2007, 2008). The parameters used in the simulation are listed in Tab. 5.2.

2.3.2 Numerical results

The simulations are first performed for a template with equally long indenters (see Figure 2.2), with the aim of investigating the effect of line spacing on imprinting. The gold crystal is initially stress-free and dislocation-free. The dislocation source density is taken to be $\rho_{\text{nuc}} = 50\ \mu\text{m}^{-2}$ and the obstacle density $\rho_{\text{obs}} = 100\ \mu\text{m}^{-2}$. The surface profiles obtained at final imprinting depth and after unloading and relaxation are shown in Figure 2.5. To better visualize the final imprints the profile of the crystal surface is plotted using independent axes. In agreement with the experimental results, the part of the template indicated as Zone 1 does not leave discrete imprints in the crystal but only a single imprint, as if the closely spaced lines would act as a larger single line. The total width of the imprint produced by Zone 1 is approximately twice as large as the actual width of Zone 1, which is about 1000 nm. Similarly to

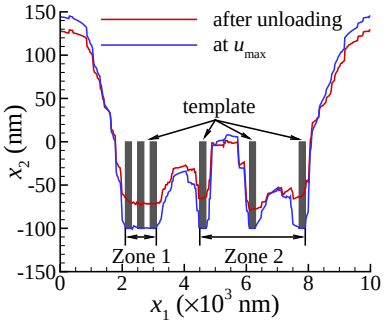

Figure 2.5. The profile of the top surface at the maximum imprinting depth and after unloading and relaxation.

the experiments the imprints obtained by this simulations are rather irregular and the surface is rough due to steps left by the dislocations that have glided out of the crystal top surface. Additional roughening can be noticed during unloading and relaxation. Also, large material pile-up can be observed at the borders of the two Zones, while between Zone 1 and 2 the material has 'sinked-in' below the original surface height. This is consistent with the experimental observations.

The simulation is repeated in order to assess the effect of (1) a larger source density and (2) an initial dislocation population. Figure 2.6 compares the profile obtained in Figure 2.5 with those obtained by imprinting a crystal that contains a three times as large source density, i.e $\rho_{\text{nuc}} = 150\ \mu\text{m}^{-2}$. For this simulation a smaller slip plane spacing is used, i.e. $s = 25\text{b}$. In the

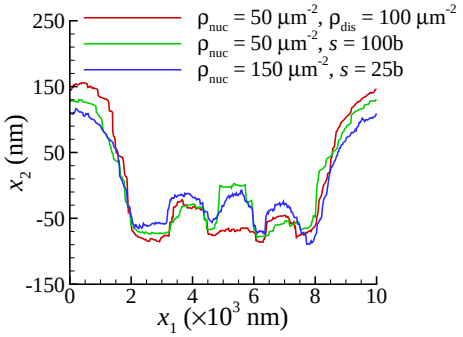

Figure 2.6. Top surface profile obtained by imprinting a crystals with initial dislocation density, with different values of source density and slip plane spacing.

limit of a continuum dislocation distribution much better imprints would be obtained, but clearly this larger source density and smaller slip plane spacing do not lead to an improvement of the profiles. The discreteness of dislocation sources in combination with the localized stress state in the imprinted metal are still responsible for irregular and rough imprints that poorly resemble the template. An initial dislocation density $\rho_{\text{dis}} = 100\ \mu\text{m}^{-2}$, with dislocations randomly distributed in the crystal has also a minor influence in the outcome of the imprints. We chose for randomly distributed dislocations to avoid a particular initial stress state that would make unfair the comparison with the dislocation-free crystal. A specific crystal growth process or loading history would clearly give a preferred initial dislocation structure and stress state. Unfortunately we fail to see a dislocation structure compatible with crystal growth or imposed deformation that would improve the quality of the imprints.

Notice that in these simulations the bottom of all retained imprints has approximately the same depth after relaxation, contrary to the experiments (see Figure 2.3 and 2.4) where the imprints underneath Zone 1 are much deeper than those underneath Zone 2. For a better resemblance of the experiments we then perform simulations (1) for a template with indenters of different length and (2) for a tilted template.

1. The template is designed such that the indenters in Zone 2 are 50 nm shorter than the indenters in Zone 1 (see Figure 2.7 for a sketch). The profiles obtained with this template are shown in Figure 2.8 and better

resemble the experimental profiles of Type 1 in Figure 2.3.

2. The template is not parallel to the single crystal surface but tilted by θ, as shown in Figure 2.9. The tilting angle is $\theta = 1°$. Clearly, the final depth of the residual imprints decreases from left to right, leading to a final profile (Figure 2.10) in good agreement with the experimental profiles of Type 2 in Figure 2.4. Note that the bottom of the imprints is approximately as tilted as the template. Since this simulation leads in our opinion to the best agreement with the experimental findings on the basis of the obtained surface profiles, we will use in the following section the tilted template to directly compare experiments and simulations of imprinting by cyclic loading of the single crystal.

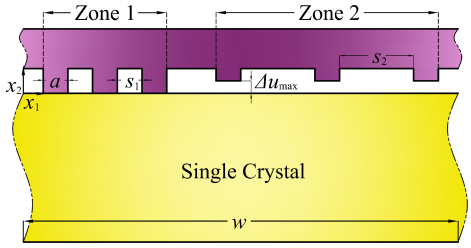

Figure 2.7. Sketch of the gold single crystal imprinted by a rigid template having shorter indenters in Zone 1 than in Zone 2.

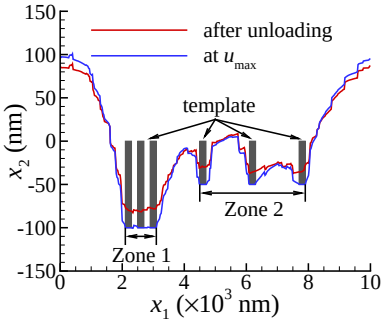

Figure 2.8. The profile of the top surface at the maximum imprinting depth and after unloading and relaxation when the length of the indenters in Zone 1 and Zone 2 is different.

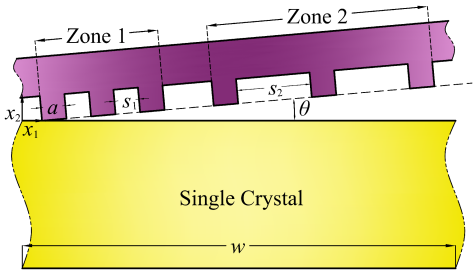

Figure 2.9. Sketch of the gold single crystal imprinted by a rigid template tilted by $\theta = 1°$.

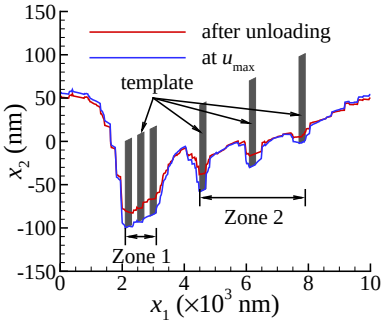

Figure 2.10. The profile of the top surface at maximum imprinting depth and after unloading and relaxation.

2.3.3 Cyclic loading: comparison between experiments and simulations

As previously mentioned the experiment is performed by loading and unloading the crystal nine times at an increasing load up to 10^4 μN. For the simulations the final imprinting depth of 100 nm is reached by stepwise increasing the displacement by 25 nm each cycle. We here choose to compare the experiments that lead to the final profile in Figure 2.4 to the simulations with the tilted template that lead to the profile in Fig 2.10. For conciseness we only show the outcome of three of the cycles in Figure 2.11, where we compare the experimental profiles with the profiles calculated numerically and the corresponding stress profiles and dislocation distributions in the gold crystal. Note that the comparison aims at being only qualitative and that the indentation

depths reached at each cycle do not match. In the first cycle, one single im-

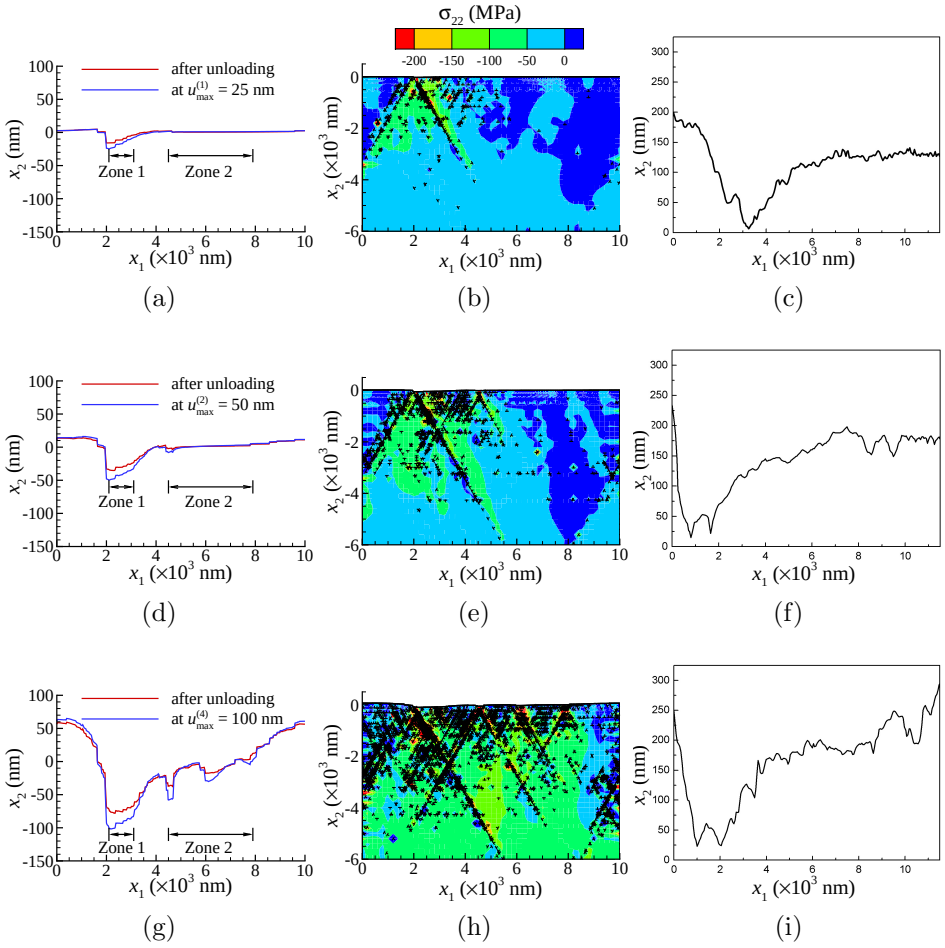

Figure 2.11. (a)(d)(g) Imprinting profiles obtained numerically at increasing imprinting depth; (b)(e)(h) corresponding distribution of σ_{22} and dislocation structure; (c)(f)(i)imprinting profiles obtained experimentally.

print is formed underneath Zone 1, both in the simulated and experimental profile. Dislocations generate mainly from the contact between the crystal and the edge of the leftmost indent, there is no evidence of dislocations nucleating underneath each of the three lines in Zone 1. The three lines are so close that the high contact stress state that each of them causes is too localized for

dislocation plasticity to accommodate the deformation. The likelihood that dislocation sources are located sufficiently close to all of the three contacts is in fact extremely small. A few sources will be in the neighborhood of Zone 1 and experience the stress state caused by the three contacts as if they were a single contact.

During the second simulated cycle the first imprint becomes deeper and an additional imprint is obtained. The new imprint corresponds to the leftmost indenter in Zone 2. More dislocations have been generated under the first contact and new dislocations have been nucleated from the new contact at about 4.2 μm and in between these contacts. Also in the experimental profile it is possible to distinguish the leftmost imprint of Zone 2, judging from the AFM image of the surface topography.

At final indentation depth all imprints transferred from Zone 2 are visible both in the simulated and experimental profile. From the dislocation distribution it is also possible to discern dislocation gliding from slip planes in the close neighborhoods of all indenters of Zone 2.

2.4 Concluding remarks

We have performed experiments and simulations for the direct nanoimprinting of a gold single crystal by means of a template made of differently spaced tungsten lines. The combination of experiments and simulations has shown that:

- good pattern transfer can be achieved when the lines are spaced from each other at a distance of about 1 μm;
- the edges of the obtained grooves are not smooth but rather stepped, due to dislocations gliding out of the edges and leaving displacement steps at the surface;
- if the lines are too close to each other, individual imprints cannot be retained. For zones of the template where the lines are close to each other (about 100 nm) the whole zone acts as a single wide line that indents the crystal. The reason for this behavior is the discrete nature of dislocations and dislocation sources and their limited availability at the sub-micron scale;
- material pile-up can be observed at the borders of the two indenter zones, while material sink-in is dominant between zones.

In conclusion this work has highlighted feasibility and limitations of the direct nanoimprinting process on metal. Note that our analysis has only considered two different spacings between lines in the template. We can therefore not determine a threshold value below which patterning cannot be transfered in the gold crystals, just state that we found good transfer for a spacing of about 1 μm, no transfer for 100 nm.

Acknowledgements

LN is grateful to the Dutch National Scientific Foundation NWO and Dutch Technology Foundation STW for their financial support (VENI grant 08120). JL gratefully acknowledges the financial support by the Air Force Office of Sponsored Research (AFOSR) YIP award FA9550-09-1-0084 and by NSF grant DMR-1128818. This work was performed, in part, at the Center for Integrated Nanotechnologies, an Office of Science User Facility operated for the U.S. Department of Energy (DOE) Office of Science. Los Alamos National Laboratory, an affirmative action equal opportunity employer, is operated by Los Alamos National Security, LLC, for the National Nuclear Security Administration of the U.S. Department of Energy under contract DE-AC52-06NA25396.

References

Abu Al-Rub, R.K., Voyiadjis, G.Z., 2004. Analytical and experimental determination of the material intrinsic length scale of strain gradient plasticity theory from micro- and nano-indentation experiments. Int. J. Plast. 20, 1139–1182.

Ahn, S.W., Lee, K.D., Kim, J.S., Kim, S.H., Lee, S.H., Park, J.D., Yoon, P.W., 2005. Fabrication of subwavelength aluminum wire grating using nanoimprint lithography and reactive ion etching. Microelectron. Eng. 78-79, 314–318.

Alcalá, J., Barone, A.C., Anglada, M., 2000. Influence of plastic hardening on surface deformation modes around Vickers and spherical indents. Acta Mater. 48, 3451–3464.

Balint, D.S., Deshpande, V.S., Needleman, A., Van der Giessen, E., 2008. Discrete dislocation plasticity analysis of the grain size dependence of the flow strength of polycrystals. Int. J. Plast. 24, 2149–2172.

Bouvier, S., Needleman, A., 2006. Effect of the number and orientation of active slip systems on plane strain single crystal indentation. Modelling Simul. Mater. Sci. Eng. 14, 1105–1125.

Buzzi, S., Robin, F., Callegari, V., Löffler, J.F., 2008. Metal direct nanoimprinting for photonics. Microelectron. Eng. 85, 419–424.

Choi, Y., Van Vliet, K.J., Li, J., Suresh, S., 2003. Size effects on the onset of plastic deformation during nanoindentation of thin films and patterned lines. J. Appl. Phys. 94, 6050–6058.

Cleveringa, H.H.M., Van der Giessen, E., Needleman, A., 1999. A discrete dislocation analysis of bending. Int. J. Plast. 15, 837–868.

Cross, G., O'Connell, B., Özer, H., Pethica, J., 2007. Room temperature mechanical thinning and imprinting of solid films. Nano Lett. 7, 357–362.

Engels, P., Ma, A., Hartmaier, A., 2012. Continuum simulation of the evolution of dislocation densities during nanoindentation. Int. J. Plast. 38, 159–169.

Flom, D.G., Komanduri, R., 2002. Some indentation and sliding experiments on single crystal and polycrystalline materials. Wear 252, 401–429.

Gaillard, Y., Tromas, C., Woirgard, J., 2003. Study of the dislocation structure involved in a nanoindentation test by atomic force microscopy and controlled chemical etching. Acta Mater. 51, 1059–1065.

Gao, Y.F., Lou, J., 2008. Dislocation Nucleation and Pileup under a Wedge Contact at Nanoscale. J. Nanomater 2008.

Greer, J.R., Nix, W.D., 2006. Nanoscale gold pillars strengthened through dislocation starvation. Phys. Rev. B 73.

Guo, L.J., 2007. Nanoimprint lithography: methods and material requirements. Adv. Mater. 19, 495–513.

Lister, K.A., Thoms, S., Macintyre, D.S., Wilkinson, C.D.W., Weaver, J.M.R., Casey, B.G., 2004. Direct imprint of sub-10 nm features into metal using diamond and SiC stamps. J. Vac. Sci. Technol., B 22, 3257–3259.

Lou, J., Shrotriya, P., S., A., Buchheit, T., Soboyejo, W.O., 2006. Strain gradient plasticity length scale parameters for LIGA Ni MEMs thin films. Mater. Sci. Eng., A 441, 299–307.

Mei, F., Parida, P., Jiang, J., Meng, W., Ekkad, S., 2008. Fabrication , Assembly , and Testing of Cu- and Al-Based Microchannel Heat Exchangers. Journal of Microelectromechanical Systems 17, 869–881.

Miller, R.E., Rodney, D., 2008. On the nonlocal nature of dislocation nucleation during nanoindentation. J. Mech. Phys. Solids 56, 1203–1223.

Nicola, L., Bower, A.F., Kim, K.S., Needleman, A., Van der Giessen, E., 2007. Surface versus bulk nucleation of dislocations during contact. J. Mech. Phys. Solids 55, 1120–1144.

Nicola, L., Bower, A.F., Kim, K.S., Needleman, A., Van der Giessen, E., 2008. Multi-asperity contact: A comparison between discrete dislocation and crystal plasticity predictions. Philos. Mag. 88, 3713–3729.

Nicola, L., Van der Giessen, E., Needleman, A., 2003. Discrete dislocation analysis of size effects in thin films. J. Appl. Phys. 93, 5920–5928.

Nicola, L., Xiang, Y., Vlassak, J.J., Van der Giessen, E., Needleman, A., 2006. Plastic deformation of freestanding thin films: Experiments and modeling. J. Mech. Phys. Solids 54, 2089–2110.

Nix, W.D., 1997. Elastic and plastic properties of thin films on substrates: Nanoindentation techniques. Mater. Sci. Eng., A 234–236, 37–44.

Nix, W.D., Gao, H.J., 1998. Indentation size effects in crystalline materials: A law for strain gradient plasticity. J. Mech. Phys. Solids 46, 411–425.

Pharr, G.M., Oliver, W.C., Brotzen, F.R., 1992. On the generality of the relationship among contact stiffness, contact area, and elastic modulus during indentation. J. Mater. Sci. 7, 613–617.

Schift, H., 2008. Nanoimprint lithography: An old story in modern times? A review. J. Vac. Sci. Technol., B 26, 458–480.

Schnabel, B., Kley, E., Wyrowski, F., 1999. Study on polarizing visible light by subwavelength-period metal-stripe gratings. Opt. Eng. 38, 220–226.

Senger, J., Weygand, D., Gumbsch, P., Kraft, O., 2008. Discrete dislocation simulations of the plasticity of micro-pillars under uniaxial loading. Scr. Mater. 58, 587–590.

Tymiak, N.I., Kramer, D.E., Bahr, D.F., Wyrobek, T.J., Gerberich, W.W., 2001. Plastic strain and strain gradients at very small indentation depths. Acta Mater. 49, 1021–1034.

Williams, J.D., Wang, W., 2004. Microfabrication of an electromagnetic power relay using SU-8 based UV-LIGA technology. Microsyst. Technol. 10, 699–705.

Yao, C.H., Wu, C.L., Sung, C.K., 2008. Effects of thin film properties on metallic pattern formation by direct nanoimprint. J. Mater. Process. Technol. 201, 765–769.

Yu, Z., Wu, W., Chen, L., Chou, S.Y., 2001. Fabrication of large area 100 nm pitch grating by spatial frequency doubling and nanoimprint lithography for subwavelength optical applications. J. Vac. Sci. Technol., B 19, 2816–2819.

Zong, Z., Lou, J., Adewoye, O.O., Elmustafa, A.A., Hammad, F., Soboyejo, W.O., 2006. Indentation size effects in the nano- and micro-hardness of fcc single crystal metals. Mater. Sci. Eng., A 434, 178–187.

Zong, Z., Soboyejo, W., 2005. Indentation size effects in face centered cubic single crystal thin films. Mater. Sci. Eng., A 404, 281–290.

Chapter 3

Effect of interface on metal nanoimprinting: a dislocation dynamics study

Abstract

Simulations of metal nanoimprinting by a rigid template are performed with the aim of finding the optimal conditions to retain imprints in a thin film on a substrate. Specifically, attention is focussed on the interface conditions between film and substrate and on the template shape. Deeper imprints are obtained when the interface between film and substrate is penetrable to dislocation motion. When the protruding contacts of the rigid template are closely spaced the interaction between neighboring contacts gives rise to material pile-ups between imprints.

3.1 Introduction

Metal nanoimprinting is of great technological interest due to its potential applications in miniaturized systems. While the most common technique to achieve nanoimprints in metal is lithography, e.g. (Guo, 2007), imprinting by mechanical indentation of the film has recently been suggested as a promising alternative approach, see e.g. (Cross et al., 2006). The objective of this study is to investigate numerically the ability of a metal film on substrate to retain imprints when indented by a rectangular wave pattern. We focus our attention on the nature of the interface between film and substrate, and on the effect of the spacing between protruding contacts. In this respect the size dependence of plastic properties at the sub-micron size scale is expected to cause a non-trivial interaction of the plastic zones underneath the contacts (Nicola et al., 2008).

At the length scale of interest for miniaturized devices, conventional finite element simulations based on classical continuum plasticity fail in predicting localized stresses and deformations. The approach used in this study is 2D discrete dislocation plasticity (Van der Giessen and Needleman, 1995), where plasticity in the metal film is described in terms of the collective motion of discrete dislocations. The discreteness of dislocations, with an evolving density, is the key element for size dependent plasticity, giving rise to a large deviation of submicron-structure behavior from that of bulk metal. In addition, large

This chapter is published as:
Y. Zhang, E. Van der Giessen and L. Nicola, Dislocation dynamic simulations of metal nanoimprinting, 2009 MRS Fall Meeting

number of dislocations gliding out the metal free surface leave surface steps that are comparable in size to the depth of the final imprint.

Dislocations are modeled as line singularities in an otherwise isotropic linear elastic medium. Constitutive rules are supplied for the glide of dislocations as well as their generation, annihilation and pinning at point obstacles. The simulations track the evolution of the dislocation structure during loading, unloading and relaxation and provides an accurate description of the final imprinted profile.

3.2 Model

The thin film is modeled as an infinitely long strip of metal of thickness h_f (see Fig. 6.1) bonded to an elastic substrate of height h_s. The film is constrained to deform in plane strain under the indentation by a rigid template with a rectangular wave profile. Each protruding flat contact of width a and spacing s is assumed to stick perfectly to the thin film during imprinting. The analysis is performed on a periodic unit cell containing three contacts.

In all simulations the metal film is $h_\mathrm{f} = 200$ nm thick and is taken to represent aluminum through its Young's modulus $E = 70$ GPa and Poisson's ratio $\nu = 0.33$. Imprinting occurs at a constant speed $\dot{u} = -2 \times 10^7$ nm/s (corresponding to a uniform strain rate $\dot{\epsilon} = \dot{u}/h_\mathrm{f} = -6.7 \times 10^4 s^{-1}$) to a maximum imprinting depth $u_\mathrm{max} = 10$ nm. Dislocations with a Burgers vector magnitude $b = 0.25$ nm can nucleate from surface sources only (see (Nicola et al., 2007)) with a fixed nucleation time t_nuc=10 ns. For this nucleation time, the strain rate is sufficiently low to capture all nucleation events and thus correctly describe the yield point. Dislocation glide occurs on two sets of parallel slip planes oriented at $\varphi = 60°$ and $120°$ with the x_1 axis. In the simulations, the active slip planes are spaced at $86b$ and contain a dislocation source just underneath the free surface with nucleation strength $\tau_\mathrm{nuc} = 50$ MPa, thus the linear density of surface sources is $\rho_\mathrm{nuc} = 80\ \mu\mathrm{m}^{-1}$. Obstacles, which represent forest dislocations in the material prior to loading and small precipitates, are distributed randomly on the slip planes in the metal, amounting to a density of $\rho_\mathrm{obs} = 30\ \mu\mathrm{m}^{-2}$. The critical strength of obstacles is $\tau_\mathrm{obs} = 150$ MPa. The substrate, of height $h_\mathrm{s} = 100$ nm, is treated as being elastic and has the same elastic constants as the film. Two limiting cases are considered for the interface between film and substrate, i.e. the interface is taken to be either impenetrable to dislocation motion or perfectly transparent. In the first case impenetrable obstacles prevent the dislocations from entering the substrate, in the second case dislocations are absorbed in the interface. A

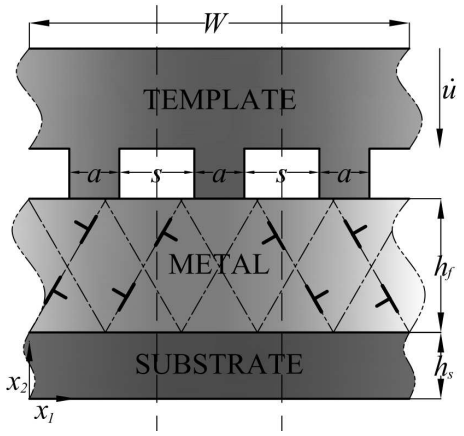

Figure 3.1. Two dimensional model of a metal thin film on substrate imprinted by a rigid template with rectangular wave profile. Each unit cell contains three flat contacts of size a and spacing s.

fully penetrable interface models the case that the adhesion is so poor that dislocations disappear at the interface without affecting the elastic substrate.

3.3 Effect of interface penetrability

To study the difference in imprinting when performed with a perfectly penetrable or an impenetrable interface, simulations are carried out for contacts with width $a = 100$ nm spaced 900 nm apart. The imprinting force during loading and unloading is shown in Fig. 3.2a. As forseeable, the film with impenetrable interface hardens more than that with penetrable interface, since dislocations that pile up at the interface with the substrate obstruct stress relaxation. During retraction of the indenter, the dislocations that have piled up in the film are available to glide in the opposite direction and to partly recover the deformation. This can be seen in Fig. 3.2b where the surface profiles are shown for the two films after complete unloading. The retained imprints are significantly more evident when the interface is penetrable. Figure 3.3 shows the stress state and dislocation structure in the films at $u_{\max} = 10$ nm. As expected, the dislocation density is clearly higher when the interface is impenetrable. The plastic zones underneath the contacts are separated from the neighboring ones in both films. In the following section we will analyze the effect of contact spacing on imprinting.

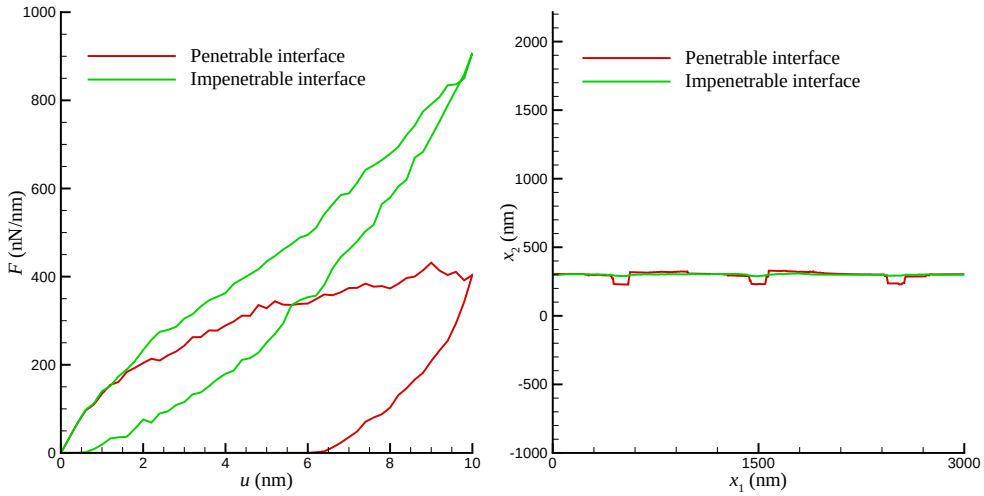

Figure 3.2. (a) The imprinting force during loading and unloading with an $s = 900$ nm template, and (b) the resulting surface profiles after unloading for different interface conditions. The deformation in x_2 direction is magnified by a factor 10.

3.4 Effect of template shape

The effect of the template shape is investigated for film-substrate systems with a penetrable interface. To this end simulations are carried out for values of the spacing between contacts ranging from 300 to 900 nm. Figure 3.4 shows the stress state and dislocation structure at final imprinting depth for a film indented by a template with $s = 300$ nm. By contrasting Fig. 3.4 with Fig. 3.3 one notices that when contacts are close to each other there is more material piling-up between contacts and that the plastic zones overlap.

Figure 3.5 compares the corresponding surface profile with that for $s = 900$ nm (cf. Fig. 3.2) as well as $s = 500$ nm. The displacements are magnified by a factor 20 for ease of visualization. The imprints are deeper when the contacts are closely spaced but they are less well defined, i.e. the surface becomes rougher with extrusions that are comparable in size to the imprinting depth. The maximum depth of the imprints relative to the original top surface is 9.6, 7.5 and 7.2 nm for the films with $s = 300$, 500 and 900 nm, respectively.

To quantify the effect of spacing between contacts on the final surface

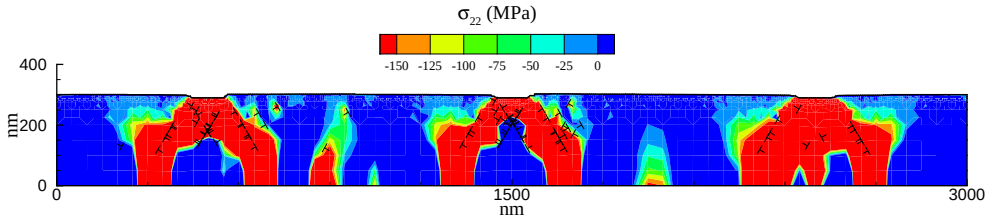

(a) penetrable interface

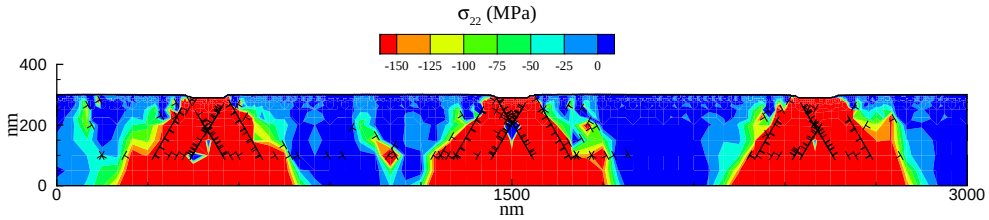

(b) impenetrable interface

Figure 3.3. Distribution of dislocations and σ_{22} for a film imprinted by a template with $s = 900$ nm and (a) penetrable interface (c) impenetrable interface with the substrate.

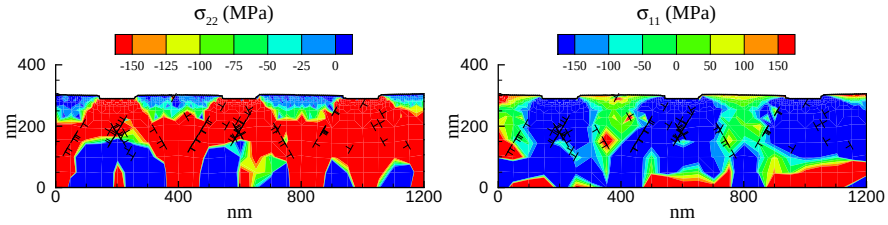

(a) (b)

Figure 3.4. Distribution of dislocations and stress components (a) σ_{22}, (b) σ_{11} for a film with contact spacing $s = 300$ nm and a penetrable interface.

profiles we use the root mean square roughness defined as

$$R_{\mathrm{m}} = \sqrt{\frac{1}{N}\sum_{i=1}^{N}(h_{\mathrm{i}} - h_{\mathrm{m}})^2}, \tag{3.1}$$

where N is the total number of nodes on the film surface; h_i is the x_2-coordinate of the ith node of the surface and h_{m} is the mean height of the top

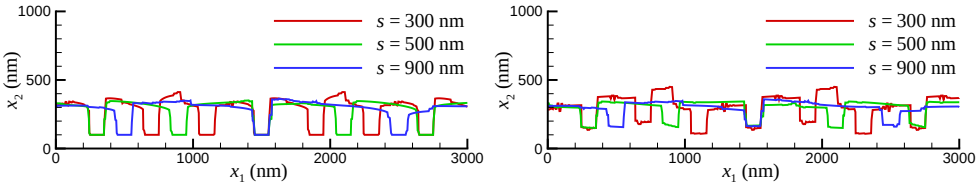

Figure 3.5. The film surface (a) at maximum imprinting depth; (b) after unloading and relaxation with different s for a penetrable interface. The displacement in x_2 direction has been magnified by a factor 20. Multiple replicas of the unit cell are shown when $s < 900$ nm.

surface. Results in Fig. 3.6 show that for all template shapes considered here the imprints are better retained when the spacing between contacts is smaller. Moreover, when the spacing is below 500 nm interaction between contacts clearly takes place, material piles up in between contacts during loading and the waviness of the surface is maintained and even increased during unloading (see Fig. 3.5).

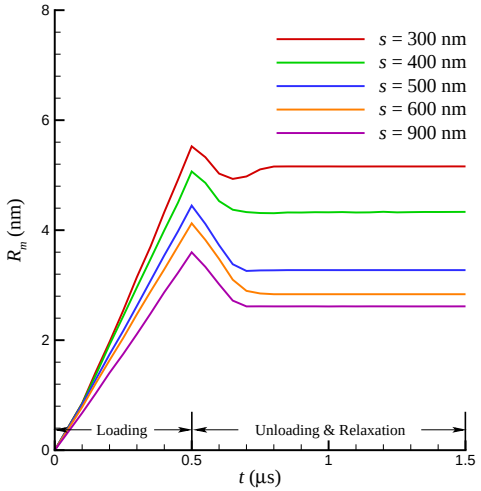

Figure 3.6. Evolution of the root mean square roughness during imprinting of films with a penetrable interface using different contact spacings s.

3.5 Conclusions

Interface conditions between film and substrate are essential in determining the success of the imprinting process: if the interface is perfectly penetrable to dislocation motion the retained surface indents are the deepest achievable. Thus, to the end of creating well-defined nanopatterns an interface that absorbes dislocations is clearly the preferable choice. For a 200 nm thick film, interaction between neighboring contacts occurs when the spacing is below 500 nm for a contact size of 100 nm. When such a spacing is used material pile-ups appear in between contacts and the surface profile becomes more wavy.

Acknowledgements

LN is grateful to the Dutch National Scientific Foundation NWO and Dutch Technology Foundation STW for their financial support (VENI grant 08120).

References

Cross, G. L. W.; OĆonnell, B. S.; Ozer, H. O., and Pethica, J. B. Room temperature mechanical thinning and imprinting of solid films. *Nano Lett.*, 7:357–362, 2006.

Guo, L. J. Nanoimprint lithography: methods and material requirements. *Adv. Mater.*, 19:495–513, 2007.

Nicola, L.; Bower, A. F.; Kim, K. S.; Needleman, A., and Van der Giessen, E. Surface versus bulk nucleation of dislocations during contact. *J. Mech. Phys. Solids*, 55:1120–1144, 2007.

Nicola, L.; Bower, A. F.; Kim, K.-S.; Needleman, A., and Van der Giessen, E. Multi-asperity contact: a comparison between discrete dislocation and crystal plasticity predictions. *Philos. Mag.*, 88:3713–3729, 2008.

Van der Giessen, E. and Needleman, A. Discrete dislocation plasticity: a simple planar model. *Modelling Simul. Mater. Sci. Eng.*, 3:689–735, 1995.

Chapter 4

Effect of template shape on metal nanoimprinting: a dislocation dynamics study

Abstract

Dislocation dynamics simulations are performed to investigate the effect of template shape on the nanoimprinting of metal layers. To this end metal thin films are imprinted by a rigid template, made of an array of equispaced indenters of various shape, i.e. rectangular, wedge and circular. The geometry of the indenters is chosen such that the contact area is approximately the same at final imprinting depth. Results show that for all template shapes the final patterns strongly depend on the dislocation activity and that each imprint differs from the neighboring ones. Large material pile ups appear between the imprints such that polishing of the metal layer is suggested for application of the patterns in electronics. Rectangular indenters require the lowest imprinting force and achieve the deepest retained imprints.

4.1 Introduction

Metal nanoimprinting is a fabrication technique currently applied to a wide variety of miniaturized systems (Guo, 2007). The pattern is generally transferred from a rigid template onto a polymer or photoresist and afterwards etched into the metal. A different way to go is to transfer the pattern directly from the template onto a metal layer, by plastically deforming the metal (Cross et al., 2006). The objective of this study is to investigate numerically the capability of the metal to retain imprints when directly indented by a template with protruding contacts of various shape. Specifically, each protruding contact is either rectangular, circular or wedge shaped.

The challenge originates from the size dependent plastic properties of metal layers at the sub-micron size scale (Zhong et al., 2007), for which conventional classical plasticity models have proven to be non-suitable. The approach used in this study is discrete dislocation plasticity (Van der Giessen and Needleman, 1995), where plasticity in the metal film originates from the collective motion of discrete dislocations. This simulation technique has been successfully employed in the prediction of size effects in metal by indentation (Widjaja et al., 2005) as well as by imprinting with equispaced contacts (Nicola et al., 2008; Zhang et al., 2010).

This chapter is published as:
Y. Zhang and L. Nicola, Effect of template shape on metal nanoimprinting: a dislocation dynamics study, J. Zhejiang Univ.-Sc. A 11 (2010) 722-726

The simulations show that the final patterns in the metal are very irregular in shape for all templates chosen. More specifically, each imprint in the unit cell has a unique shape, determined by the local dislocation activity.

4.2 Method

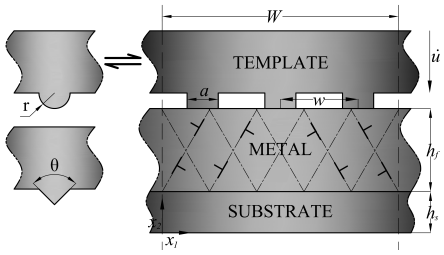

Figure 4.1. Two dimensional model of a metal thin film on substrate imprinted by a rigid template with protruding contacts with rectangular, wedge or circular shapes.

An infinitely long thin film of height $h_f = 200$ nm on an elastic substrate of height $h_s = 50$ nm is imprinted by a rigid template (see Fig.4.1). If the choice of a thicker elastic substrate were made, shallower retained imprints would be obtained for the same imprinting depth. The template is made of arrays of equispaced indenters of different shape, i.e. rectangular, wedge and circular. Imprinting occurs at a constant velocity $\dot{u} = 5 \times 10^6$ nm/s to the final imprinting depth $u_{\max} = 10$ nm. The 2D analysis is performed on a unit cell of width W comprising n indenters with center-to-center spacing w. Contact between template and metal is assumed to be perfectly sticking during indentation by prescribing:

$$\dot{u}_1(x_1, h) = 0,\ \dot{u}_2(x_1, h) = -\dot{u},\ x_1 \in A_{\text{contact}} \tag{4.1}$$

where $h = h_s + h_f$ and A_{contact} is the surface in contact. The remaining top surface is free:

$$\sigma_{12}(x_1, h) = \sigma_{22}(x_1, h) = 0,\ x_1 \notin A_{\text{contact}}$$

Because of the sticking nature of the contact, the bottom surface cannot expand during imprinting. Periodic boundary conditions are imposed at the left and right boundaries of the unit cell:

$$\dot{u}_1(0, x_2) - \dot{u}_1(W, x_2) = 0, \dot{u}_2(0, x_2) - \dot{u}_2(W, x_2) = 0,\ \forall x_2 \tag{4.2}$$

The metal layer is taken to have the elastic properties of aluminum: Young's modulus $E = 70$ GPa and Possion's ratio $\nu = 0.33$. For simplicity, plasticity in the substrate is ignored and the substrate is assigned the same elastic constants as the film. Equispaced dislocation sources with critical strength $\tau_{\text{nuc}} = 50$ MPa are positioned at the top surface. The source density is $\rho_{\text{nuc}} = 0.14$ /nm. Dislocations can glide on two sets of parallel slip planes, each of which contains one dislocation source. The slip planes are oriented alternatively either at 54.75° or at 125.25° with the x_1-axis. This mimics in two dimensions the slip planes for easy glide of an FCC crystal imprinted along the [010] direction (Rice, 1987). The magnitude of the Burgers vector is $b = 0.25$ nm. Obstacles with strength $\tau_{\text{obs}} = 150$ MPa are randomly distributed in the metal with density $\rho_{\text{obs}} = 30/\mu\text{m}^2$. Dislocation nucleation occurs when the resolved shear stress on a source exceeds its critical strength during the nucleation time $t_{\text{nuc}} = 1 \times 10^{-8}$ s. Then two dislocations with opposite Burgers vector are generated at a distance L_{nuc}. The glide velocity v^I of the Ith dislocation is proportional to the Peach-Koehler force f^I according to

$$f^I = Bv^I \tag{4.3}$$

with the drag coefficient $B = 10^{-4}$ Pa s.

4.3 Analysis

Simulations are performed for templates of different shape, all having indenters spaced by $w = 400$ nm. Each unit cell contains six indenters, in order to reduce statistical variations. The geometric characteristics of the indenters are the following: the width of the rectangular indenter is $a = 50$ nm, the angle of the wedge indenter is $\theta = 160°$ and the radius of the circular indenter is $r = 130$ nm. The particular geometries are chosen such to give approximately the same true contact area (projected on the x_1-axis) for the three indenter shapes at maximum imprinting depth. Force–displacement curves during indentation and unloading are shown in Fig. 4.2(a). The imprinting force is calculated at the top surface as $F := -\int_{A_{\text{contact}}} \sigma_{22}(x_1, h)\, dx_1$. To reach the maximum imprinting depth a force of approximately 1380 N/m is required for wedge and circular indenters, while a lower force, 840 N/m is needed for the rectangular indenter. This is a rather unexpected result in that the contact area for the rectangular indenter is larger than that of the other indenters for $u < 10$nm. This can be seen in Fig. 4.2(b), which gives the evolution of the contact area during loading and unloading. The contact area for the rectangular indenter during imprinting is clearly constant and qual to $a = 50$ nm. In the case of

the wedge and circular indenters the contact area plotted here is the real area of contact between the indenter and the metal layer, projected in x_1 direction. The contact area increases with a larger rate when the indenter is circular.

Figure 4.3(a) shows the metal top surface profile at the maximum imprinting depth $u_{\max} = 10$ nm. The material in between imprints forms in all cases very pronounced pile ups with irregular shape. The irregular shape of the pile ups and imprints is caused by the discrete nature of sources and dislocations. The dislocation sources distribution is non symmetric and therefore causes asimmetry in the deformation of the metal film. Also, a large number of dislocations glide out of the metal free surface during indentation and leave displacement steps there. These dislocation steps are also responsible for the discontinuous evolution of the contact area for the cases of wedge and circular indenters.

As the reader might have noticed, the profiles in Fig. 4.3(a) are shown by using independent axes for a better visibility of the imprints. In fact the correct proportions of each imprint is shown in Fig. 4.3(b), i.e. the real imprint is wider than it is deep (the impriting depth is only $u = 10$ nm, while the projected contact area is approximately 50 nm). After unloading and relaxation part of the deformation is lost due to elastic spring-back. The retained imprints are shown in Fig. 4.4. During unloading and relaxation the metal profile becomes even rougher and more irregular. This is particularly true for the imprints obtained by rectangular indenters, which are also the deepest. Since most

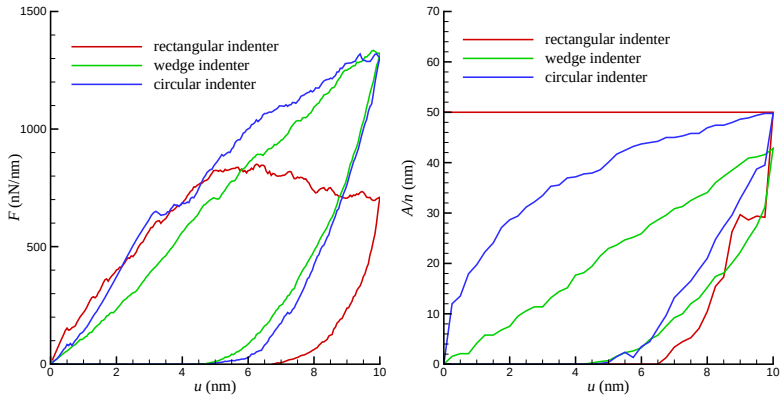

Figure 4.2. (a) The imprinting force and (b) the true contact area projected on the x_1-axis for different indenters shapes.

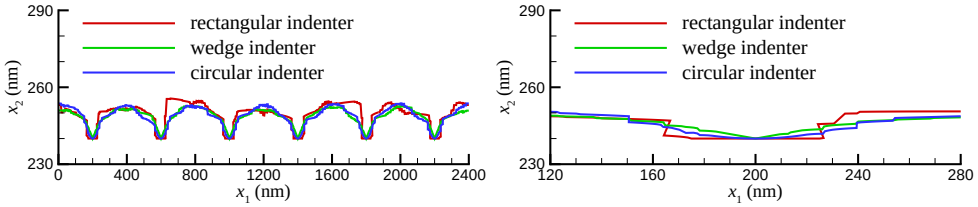

(a) (b)

Figure 4.3. (a) The top surface profile for different shapes at maximum imprinting depth $u_{\max} = 10$ nm. (b) One of the imprints in the unit cell (dependent axes).

electronic application require bonding of the patterned metal film with other layers, polishing of the final surface is advised to flatten the top surface.

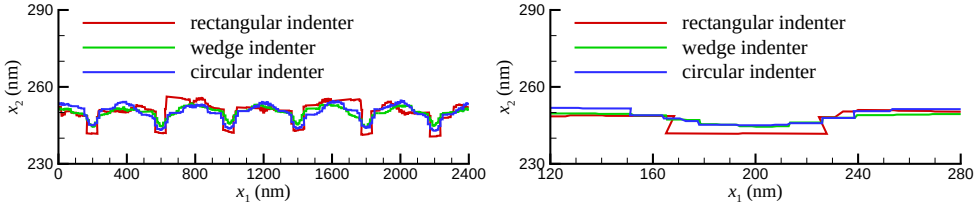

(a) (b)

Figure 4.4. (a) The top surface profile for different shapes after unloading and relaxation. (b) One of the imprints (dependent axes).

To demonstrate how the material piles up in between imprints during indentation, Fig. 4.5 shows the displacement distribution in x_2 direction and the corresponding dislocation distribution at the maximum imprinting depth. The flow of material appears the most evident in the case of rectangular indenters (Fig. 4.5(a)), where well defined triangular regions of materials are pushed up by the imprinting. The reason for which the triangular regions are very clearly defined is that the contact area is constant for the rectangular indenters during imprinting, therefore the locations of high stress concentration do not move. As a consequence only a few dislocation sources, those that are in the highly stressed region close to the edges of the contact, are very active and slip occurs on preferential slip planes. Those are the slip planes located at the borders of the triangular regions. The dislocation density in the metal is rather low,

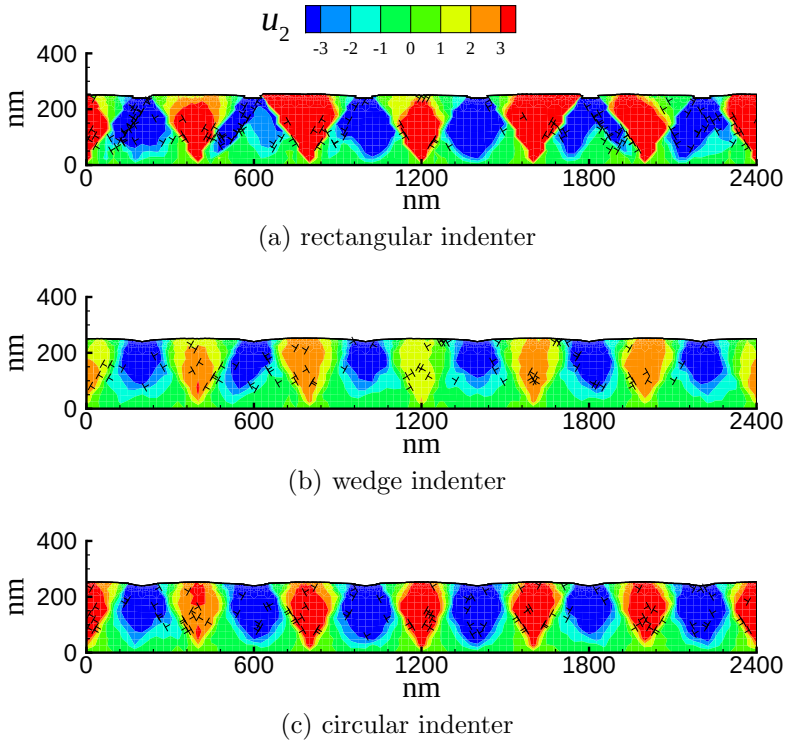

(a) rectangular indenter

(b) wedge indenter

(c) circular indenter

Figure 4.5. The distribution of displacement in x_2 direction for (a) rectangular , (b) wedge and (c) circular indenters at the maximum imprinting depth.

since many dislocations have left the material through the free top surface or have been absorbed into the interface between film and substrate.

To better characterize the final patterns Table 4.1 gives the depth of the center of the imprint d_{imp}, measured from the original film height $h = 250$ nm, and averaged over the imprints in the unit cell, i.e.:

$$d_{\text{imp}} = \frac{1}{n}\sum_{I=1}^{n} |h - x_2(wI - \frac{w}{2})|,$$

where n is the number of indenters in the unit cell. The deepest imprints are obtained by the rectangular indenters, while the shallowest by the circular indenter. We measure the width of the imprint w_{imp} at $h = 250$ nm and average over the number of imprints in the unit cell. The results are listed in Table 4.1 and show that the opening of the imprints has for all templates a

Table 4.1. Average imprint depth and width.

shape	d_{imp} (nm)	w_{imp} (nm)
rectangular	$8.08 \pm 9.96\%$	$107.28 \pm 65.28\%$
wedge	$5.02 \pm 9.39\%$	$153.27 \pm 38.34\%$
circular	$6.19 \pm 12.10\%$	$156.92 \pm 41.28\%$

rather large standard deviation. In the case of the rectangular indenters it is noteworthy that on average the opening of the imprint is twice the size of the indenter.

4.4 Conclusions

We have presented discrete dislocation simulations of the nanoimprinting of metallic thin films by a rigid template. The template is made of an array of equispaced indenters of various shape, namely rectangular, wedge and circular. The shape of the indenters is chosen such that the final contact area is approximately the same. Results show that for the chosen indenters spacing, $w = 400$ nm, the template with rectangular indenters appear the most suitable to pattern the metal, because

1. it requires a lower imprinting force than the other templates, and
2. produces the deepest retained imprints.

The reason for this is that imprinting with rectangular indenters occurs at constant contact area. Therefore, slip occurs only on selected slip planes, by that facilitating push up of material between the imprints.

Also, for all template shapes considered:

- the final surface profiles are strongly affected by the dislocation activity;
- the obtained patterns are rather irregular: each imprint is different from the neighboring ones;
- material pile ups between indenters are very pronounced. For electronic applications the metal would require polishing of the top surface.

Acknowledgements

LN is grateful to the Dutch National Scientific Foundation NWO and Dutch Technology Foundation STW for their financial support (VENI grant 08120).

References

Cross, G.L.W., O'Connell, B.S., Ozer, H.O., Pethica, J.B., 2006. Room temperature mechanical thinning and imprinting of solid films. Nano Lett. 7, 357–362.

Guo, L.J., 2007. Nanoimprint lithography: methods and material requirements. Adv. Mater. 19, 495–513.

Nicola, L., Bower, A.F., Kim, K.S., Needleman, A., Van der Giessen, E., 2008. Multi-asperity contact: a comparison between discrete dislocation and crystal plasticity predictions. Philos. Mag. 88, 3713–3729.

Rice, J.R., 1987. Tensile crack tip fields in elastic-ideally plastic crystals. Mech. Mater. 6, 317–335.

Van der Giessen, E., Needleman, A., 1995. Discrete dislocation plasticity: a simple planar model. Model. Simul. Mater. Sc. 3, 689–735.

Widjaja, A., Van der Giessen, E., Needleman, A., 2005. Discrete dislocation modelling of submicron indentation. Mat. Sci. Eng. A-Struct. 400-401, 456–459.

Zhang, Y.H., Van der Giessen, E., Nicola, L., 2010. Discrete dislocation simulations of the flattening of nanoimprinted surfaces. Model. Simul. Mater. Sc. 18.

Zhong, Z., Lou, J., Adewoye, O.O., Elmustafa, A.A., Hammad, F., Soboyejo, W.O., 2007. Indentation size effect in the nano and microhardness of FCC single crystal metals. Mater. Manuf. Process. 22, 228–237.

Chapter 5

Competition between dislocations and cracks in molecular dynamics simulations of metal nanoimprinting

Abstract

Direct metal nanoimprinting of a gold thin layer is studied by means of quasi-static molecular dynamics simulations. The aim of this study is to understand if it is possible to obtain a reproducible nanopattern with features of a few nanometers, that closely resembles the shape of the template.

The majority of our simulations show an unexpected competition between crack formation and dislocation plasticity upon retraction of the template, which leads in some cases to an imprint and in other cases to a flat surface. These results are at odds with previous simulations of metal nanoimprinting, which always predicted formation of an imprint. The reason for this discrepancy lies in the much lower (and thus more realistic) imprinting velocity used in this work.

The most interesting finding of this paper is that the competition between crack and dislocations for certain loading conditions and geometry of the crystals is driven by thermal fluctuations of the atomic velocities. Local events, namely atomic fluctuations and dislocation nucleation, determine the global mechanical response of the system, i.e. whether an imprint is obtained or not.

The relevance of thermal fluctuations is confirmed by the fact that any of the simulations presented here, if repeated at 10 K, leads to a brittle material behavior.

5.1 Introduction

Lithographic-free metal imprinting is a processing technique whereby a pattern on a rigid punch is transferred onto a metal layer by plastic deformation of the metal itself. This method has been recently proposed (Buzzi et al., 2008; Cheng et al., 2007; Youn et al., 2009) as a promising alternative to lithography, by virtue of its simplicity and cost effectiveness.

Research efforts have focused on finding the optimal processing parameters that can lead to high resolution and high reproducibility of the template pattern in the metal layer. The effects of thin film thickness (Cheng et al., 2007) and grain size (Yao et al., 2008) and the effect of template teeth size (Youn et al., 2009) and shape (Pei et al., 2007; Yao et al., 2010) have been investigated

This chapter is accepted as:
Y. Zhang, B. Thijsse and L. Nicola. Competition between dislocations and cracks in molecular dynamics simulations of metal nanoimprinting. Comp. Mater. Sci.

experimentally and numerically. Knowledge gained through these studies has led to the realization of very small nano-pattern features. For instance, on gold layers, the size of the imprints can be as small as 250 nm (Buzzi et al., 2008).

Reproducibility is the most delicate issue in metal nanoimprinting, because plastic deformation in the imprinted layer is far from homogeneous: the stress induced by the template is highly localized and plasticity is initiated and sustained by discrete carriers, dislocations, that glide on specific slip planes. Stochastics related to the exact location where dislocation partials and stacking faults appear play an increasingly important role when the pitch of the template, i.e. the spacing between its teeth, is reduced. The inhomogeneity related to plasticity at room temperature greatly affects the shape of the final imprint (Zhang et al., 2013).

The goal of this study is to understand to which extent stochastic effects influence the shape of very small nanoscale patterns. The question we aim to answer is: does a template always leave a pattern when retracted from a metal layer that it has plastically deformed, and if so, how closely does the pattern resemble the form of the template? To this end we will perform molecular dynamics simulations on gold single crystals imprinted by a tungsten template, shaped as an egg-slicer. The teeth of the template will be very closely spaced, i.e. about 15 nm. The imprinting velocity will be chosen so small that the simulation can be considered quasi-static. The reason for using a small imprinting velocity is twofold: we aim to reproduce experimental conditions as much as possible and we want to provide sufficient time to recovery processes to take place. High imprinting and unloading velocities and their effects have already been investigated in various molecular dynamics simulations of nanoimprinting and have been proven to affect imprinting pressure and final patterns significantly (Hsieh and Sung, 2007; Hsu et al., 2005; Wu et al., 2012).

The most striking feature of our simulations is an intriguing competition between dislocation plasticity and crack nucleation that leads in some cases to the formation of an imprint and in other cases to a practically flat gold metal surface. To the best of our knowledge a flat metal surface has never been reported in other studies on metal nanoimprinting (neither experimental nor numerical). However, such behavior is very similar to modeling results by (Hagelaar et al., 2007), who studied the contact formation and destruction between a tungsten tip and a tungsten substrate. In their study for certain surface orientations the contact necks before breaking, although tungsten at larger scales does not easily deform plastically.

What is actually really unexpected in our results, is that the competi-

tion between crack nucleation and dislocation plasticity seems to be critically controlled by local thermal fluctuations. Simulations only differing in the particular sample of the Maxwell-Boltzmann distribution of the initial atomic velocities, or even of the atomic velocities at maximum imprinting depth, lead in some cases to a well defined imprint and in other cases to no imprint at all.

We will demonstrate that the probability that the template leaves an imprint upon retraction is affected by the crystallographic orientation of the imprinted layer, by the maximum imprinting depth and in some cases by the dimensions of the unit cell chosen.

This study sheds light not only on nanoimprinting but more generally on the mechanical behavior of small scale metal specimens.

5.2 Model Problem

Molecular dynamics simulations are performed to study the mechanical imprinting of a gold crystal by means of a tungsten template. The template is made of equally spaced flat teeth that are intended to plastically deform the gold crystal during indentation and to leave a crenelation on the metal surface after retraction of the template, as illustrated in Fig. 5.1(a). Gold crystal and template are constructed to be infinitely repeating by periodic boundary conditions in x- and y-direction, so that the analysis is carried out on a unit cell, as indicated in Fig. 5.1(b). The width L_x and thickness L_y of the periodic crystal cell are constraint to be constant during the simulation.

Forces between atoms are calculated using the Embedded Atom Method (EAM) ((Daw and Baskes, 1984)). The EAM is widely recognized as an appropriate technique to model metal crystals, since it describes the cohesive energy of the atoms accounting for the pairwise potential between atomic neighbors as well as for the energy contributed by the electrons sea that embeds the atoms.

In this study we choose the interatomic potential function for gold and tungsten proposed by Zhou ((Zhou et al., 2004)). This potential was parametrized to match common crystal properties, cohesion energies, and heats of solution, but not compound formation. The latter is not really a restriction, since Au-W is a completely immiscible system in the solid phase. More details are given in Appendix A. In order to check whether this potential properly captures the elastic constants of gold a preliminary simulation is carried out in which a fully 3D periodic gold crystal is loaded under uniform tension by increasing the pressure from 0 MPa to 724 MPa in [001]-direction with a speed of 10 MPa/ps. The results in terms of stress–displacement curves are reported in

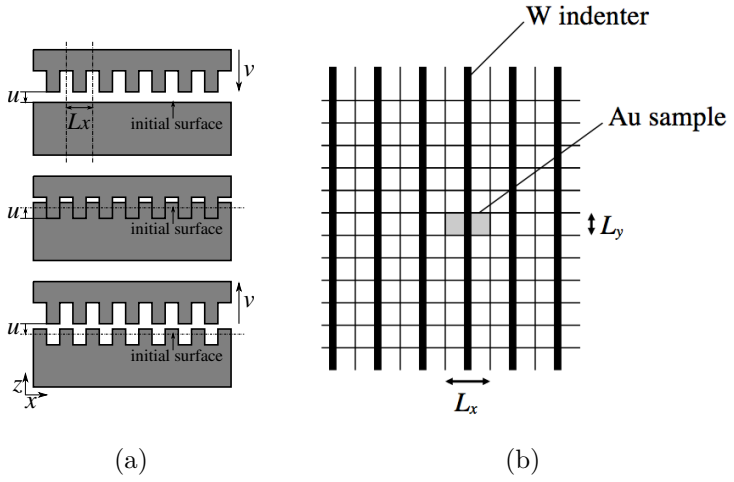

Figure 5.1. (a) Side view sketch of the modeled imprinting process. (b) Top view. The simulation unit cell is indicated in grey. Periodic boundary conditions are applied in x and y-directions.

Fig. 5.2 for two different temperatures (0 K and 300 K) and compared to experimental results by Neighbour and Alers (Neighours and Alers, 1958). The experimental and numerical results are in sufficiently good agreement, if one considers that it is common practice in the molecular dynamics community to use experimental data obtained at 300 K to fit potentials at 0 K.

Imprinting and retraction of the template occurs through the rigid motion in z-direction of so-called anchor points to which all atoms of the indenter are individually connected through springs of stiffness $k = 2000$ N/m. The anchor points are initially at the same position of the anchored atoms. The spring constant used to anchor the atoms is about six times larger than the elastic constant between tungsten atoms. This entails that the template is about six times more rigid than an actual tungsten indenter. Without full anchoring the indenter was found to deform, thereby making the reults of the imprinting simulations more difficult to interpret.

The force exerted by the template on the gold surface during imprinting and retraction is not calculated at the surface of the gold crystal but at its bottom, where the surface area is clearly identifiable. The bottom atoms (one layer) are also harmonically bound to anchor points, fixed at the initial position of the atoms and preventing the rigid body motion of the crystal. The spring constant used to connect the bottom atoms to the anchor points is $k = 20$

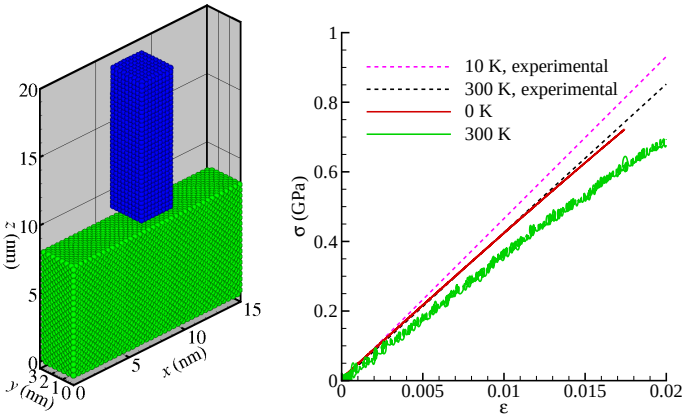

Figure 5.2. (a) The simulation unit cell before imprinting. (b) Stress-strain curves for crystals under ramping pressure from 0 to 724 MPa in z-direction at 0 K and 300 K, compared with experimental results.

N/m, thus very similar to the stiffness between gold atoms. In this way we aim to model only the top of a much thicker gold crystal. The use of fixed boundary conditions, which would mimic a gold specimen on an infinitely stiff substrate, was avoided since such conditions are known to lead to significant repulsion of the dislocations from the bottom((Choi et al., 2003)).

Each instance of the same simulation is repeated many times, each with a different selection of random initial atomic velocities from the same Maxwell-Boltzmann distribution (300 K). In the following we will refer to any of these instances with the term 'realization'.

5.3 Results

5.3.1 Reference simulation: always an imprint

The orientation of the gold crystal is chosen such that the [100]-direction aligns with the x-axis, the [010]-direction with the y-axis and the [001]-direction with the z-axis. The tungsten crystal has the same orientation as the gold crystal with respect to the reference axes. The gold crystal, periodic in x and y-directions, has dimensions L_x = 15.09 nm, L_y =2.85 nm and L_z =7.95 nm, corresponding to 74, 14 and 40 atomic planes, respectively. In order to have gold and tungsten crystals matching size in y-direction the gold crystal is

slightly compressed by 0.10% and the tungsten crystal is slightly stretched by 0.15% with respect to the 300 K lattice constants. These values are minor and given that the template behaves like a nearly rigid body, except for thermal fluctuations, the stretching is expected to have a negligible effect on the results of the simulations.

Before the imprinting is started the crystals are given 350 ps to relax to their thermal equilibrium condition. The time actually required to reach full thermal relaxation is much shorter, less than 1 ps. Relaxation of stress fields takes longer (sound velocity), but even if such fields would have been present (they are not) 350 ps would be enough.

The widths of the indenter in x-direction is $w = 2.84$ nm (18 atomic planes) and the pitch of the template is thus $p = 12.25$ nm. The temperature during imprinting and retraction is kept at 300K by a Berendsen thermostat ((Berendsen et al., 1984)).

In order to identify the velocity at which the process can be considered quasi-static preliminary simulations were performed and pressure-displacement curves were plotted for velocities ranging from $v = 4.87$ m/s to $v = 97.4$ m/s. Convergence of the curves was found for values of $v < 20$ m/s. To be conservative a velocity of $v = 9.74$ m/s was chosen. It was subsequently tested that performing the same simulations but introducing a pause where the indenter was held still at its deepest point for a 355 ps time interval did not lead to different results in terms of pressure-displacement curves.

The gold crystal is indented to a depth of $u_{\max} = 6.04$ nm which is about 3/4 of the crystal height. For a characteristic realization the pressure–displacement curves are shown in Fig. 5.3(a). The pressure is calculated by dividing the total force, exerted by the anchor points on the crystal bottom, by the constant area of the tungsten indenter 2.84×2.85 nm^2. Fluctuations in the pressure–displacement curves are smoothed by Fourier filtering. For the same realization a rough indication of the dislocation activity in the crystal is given in Fig. 5.3(b) in terms of a count of the number of atoms that during the simulation have local crystallinity HCP. The local crystallinity of the atoms is obtained by the Atomic Environment Type (AET) method, described in Appendix B. When a partial dislocation is formed and moves in a crystal the atoms on two adjacent (111) planes change their local crystallinity from FCC to HCP (and viceversa, when the trailing partial completes the passage of the full dislocation). An appreciable change in the number of HCP atoms can therefore be interpreted as an increase of dislocation activity in the crystal. A few points of interest are indicated on the curves in Fig. 5.3 with capital letters. For each of these points the distribution of σ_{zz} as well as the atoms

with HCP local crystallinity are presented in Fig. 5.4. The figure shows the front view of the body. The stress is calculated as the atomic virial stress,

$$\sigma_{\alpha\beta}^{(i)} = \frac{1}{\Omega^{(i)}} \left(\frac{1}{2} \sum_j r_\alpha^{(ij)} f_\beta^{(ij)} - m^{(i)} v_\alpha^{(i)} v_\beta^{(i)} \right), \tag{5.1}$$

where $\Omega^{(i)}$ is the atomic volume of atom i. $r_\alpha^{(ij)}$ is the component in α-direction of the vector between atoms i and j, and $f_\beta^{(ij)}$ is the component in β-direction of the force of atom i on atom j. Here, atoms i and j are first neighbors; $m^{(i)}$ and $v^{(i)}$ are the mass and velocity of atom i.

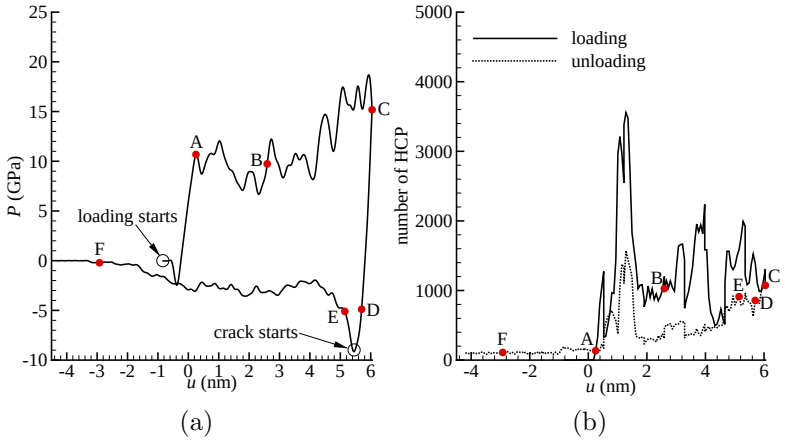

Figure 5.3. (a) Contact pressure versus imprinting depth during imprinting to $u_{\max} = 6.04$ nm and retraction of the template for a representative realization. (b) Count of atoms with HCP local crystallinity as a rough indication of dislocation activity.

By comparing Fig. 5.3 and Fig. 5.4 we aim to gain some insight in the plastic behavior of the crystal during imprinting and retraction of the template. It is noteworthy that the indenter displacement u is taken to be zero at the undeformed free surface of the gold crystal, thus at z=7.95 nm for this crystal height. Therefore the pressure–displacement curve starts from negative values of u, when the indenter has not yet approached the free surface of gold. The initial dip in the pressure–displacement curve occurring at $u = -0.44$ nm indicates that the indenter has come sufficiently close to the gold surface for the tungsten and gold atoms to attract each other. The gold surface here

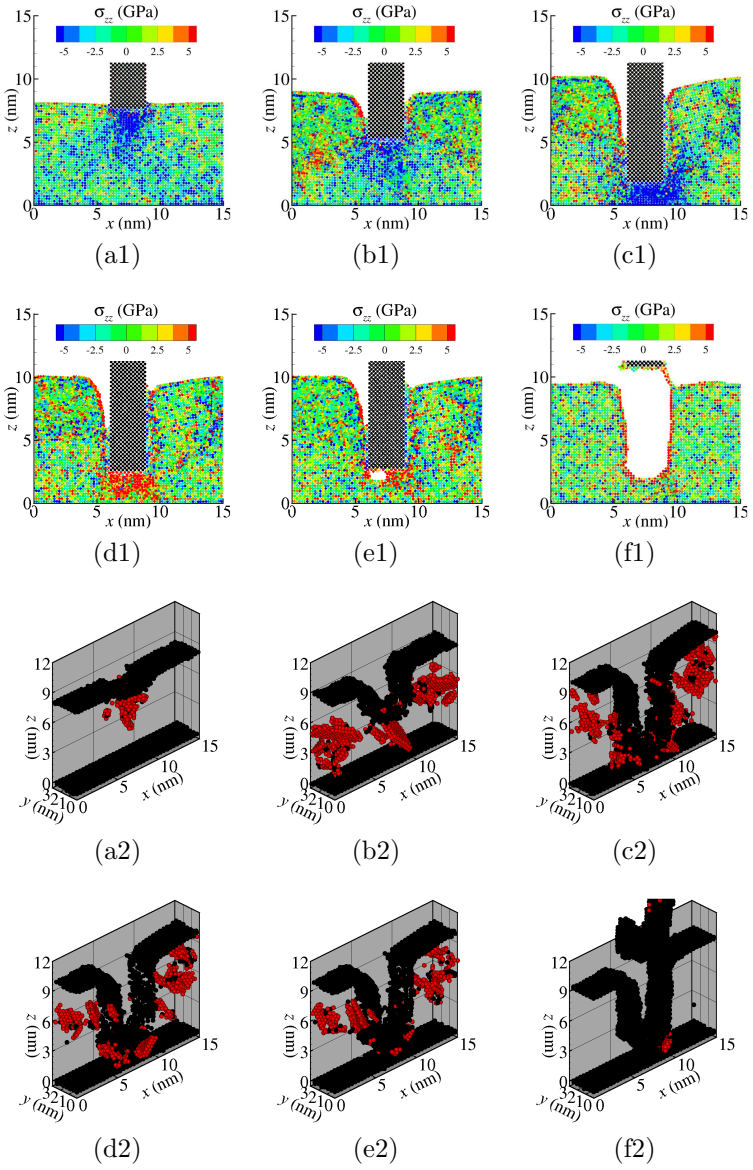

Figure 5.4. (a1-f1) Distribution of σ_{zz} corresponding to points A, B, C, D, E and F indicated in Fig. 5.3. For the same points (a2-f2): red atoms represent atoms with HCP local crystallinity, black atoms have an unclassified local crystallinity.

slightly bulges up to meet the indenter. Onset of plasticity takes place at a very large imprinting pressure, about 10 GPa, which is to be expected at this small scale and for a flat indenter (point A). In Fig. 5.4(a1) a large compressive normal stress is visible underneath the indenter. The corresponding large resolved shear stress underneath the edges of the indenter activates nucleation of the first dislocations on the (111) planes (see Fig. 5.4(a2)). The reason why the dislocations only appear as fragments in this configuration is that the periodic y-direction does not lie in a (111) slip plane. After yield the pressure–displacement curve indicates an elastic-perfectly plastic behavior up to an imprinting depth of about 4 nm. Consistently, Fig. 5.3(b) shows a sharp increase and decrease of the number of HCP atoms between point A and B and Fig. 5.4(b2) shows the presence of dislocations on the (111) planes, not only underneath the indenter but also beside it. At larger indentation depth strain-hardening can be observed in Fig. 5.3(a). This is an indication that plastic deformation becomes progressively less effective in accommodating the prescribed strain when the indenter approaches the bottom of the crystal and higher pressures have to be exerted. A decrease in dislocation activity between point B and C can also be observed in Fig. 5.3(b). The local stress underneath the indenter increases (Fig. 5.4(c2)) partly because of substrate effects, partly because it is more difficult for new dislocations to nucleate and propagate in the small region underneath the indenter (Fig. 5.4(c2)). By contrasting Fig. 5.4(a1) and (c1) one can see that at maximum imprinting depth the indenter has significantly deformed the gold crystal by pushing upwards many gold atoms (notice the height of the free surface of gold before and after loading). From the pressure–displacement curve we know that this deformation is almost entirely plastic.

The unloading slope of the pressure–displacement curve, between points C and D, does not show any deviation from the elastic slope. Indeed, between C and D the number of HCP atoms decreases only negligibly as can be seen in Fig. 5.3(b) and by comparing Fig. 5.4(c2) and (d2).

Soon after point D the pressure reaches a maximum absolute value close to 10 GPa, after which it fastly drops to very small values. This sudden drop corresponds to the displacement at which a crack nucleates and quickly propagates below the indenter (see Fig. 5.4(e1) and (e2)). Figure 5.3(b) shows that upon retraction of the template the number of atoms with HCP local crystallinity slightly decreases. These observations suggest that dislocation activity is very limited upon retraction of the template and that the nucleated crack releases the indenter and allows it to be pulled up with a small force, only needed to overcome friction at the side walls. Notice also that imme-

diately upon formation of the crack the pressure does not drop to zero but gradually decays, since the indenter side walls are in contact with the gold with a decreasing frictional area. This is confirmed in Fig. 5.4(f2) where it is possible to see gold atoms attached to the bottom but also to the sidewalls of the fully retracted indenter. In this specific run, between about $u = 2$ and $u = 0$ nm there is a new increase and decrease of HCP atoms, caused by dislocation activity that occurs when the indenter loses contact with the crystal. This dislocation activity was not found in any other realization and is considered an exceptional event.

The results presented in Fig. 5.3 and 5.4 refer to a single realization of the reference simulations. As to be expected the other nine realizations display the same overall response, with only little variations in the final profile of the imprint, and they are therefore not further discussed here.

5.3.2 A smaller imprinting depth: almost never an imprint

The reference simulation is repeated here with the only difference that the maximum imprinting depth has been reduced from $u_{\max} = 6.04$ nm to $u_{\max} = 2.60$ nm. Comparison of the pressure–displacement curves during unloading between the reference simulation and the new simulation (see Fig. 5.5(a)) indicates a striking difference: for a lower imprinting depth the pressure reaches a maximum at about 7 GPa upon retraction of the indenter after which the pressure does not suddenly decrease but reaches a constant value. This plateau is typical of an almost perfectly plastic behavior similar to the plataeu observed during imprinting, only at a lower stress level, and indicates that no crack has formed. Indeed when looking at Fig. 5.3(b) one observes an increase in the number of HCP atoms immediately after retraction of the indenter from $u_{\max} = 2.60$ nm, which signals plastic activity, and which is absent after retraction from $u_{\max} = 6.04$ nm. The snapshots of the atomic distributions and stress state during unloading in Fig. 5.6 confirm that there is no crack formation, thus no imprint retained in the gold. The tungsten indenter remains attached to the gold during full retraction and separates from it in a ductile manner, after necking of the gold, only when it is further than 1 nm from the original surface of the gold crystal.

Evidently, dislocation activity in this shallow-imprint simulation has been highly effective upon retraction of the indenter in decreasing the local stress concentration, and, as a consequence, the conditions necessary for a crack to form were never met. It is not trivial to understand why plastic deformation is more effective upon unloading after imprinting to a smaller depth than to a larger depth. Two possibilities seem the most likely: when unloading

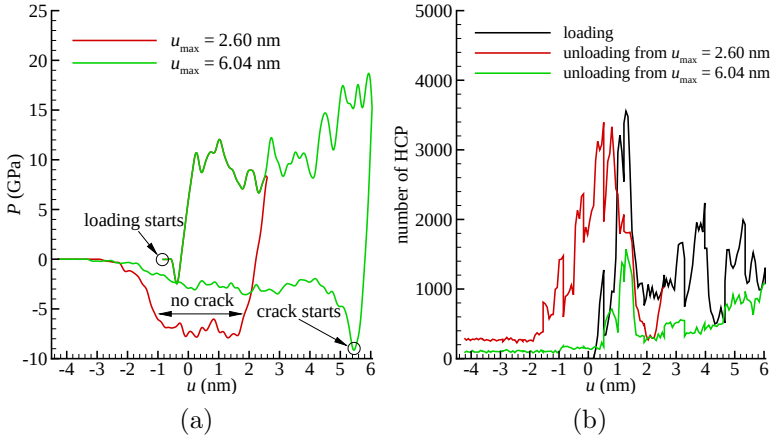

Figure 5.5. (a) Contact pressure versus imprinting depth for the simulation with maximum imprinting depth $u_{\max} = 2.60$ nm and for the reference simulation with $u_{\max} = 6.04$ nm. (b) Count of atoms with HCP local crystallinity as a rough indication of dislocation activity.

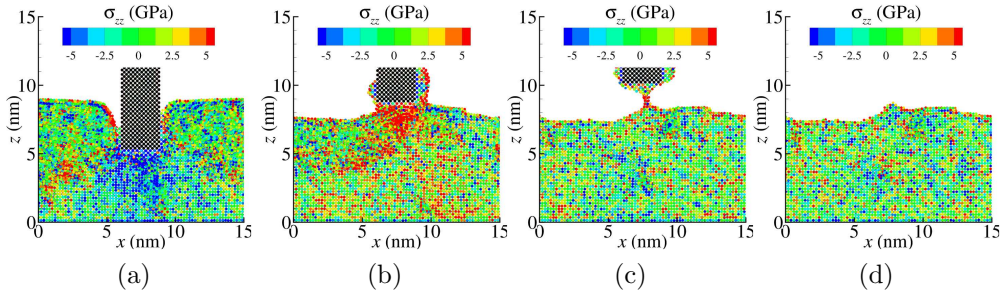

Figure 5.6. Snapshots of atomistic configurations and σ_{zz} at four different imprinting depths: (a) $u_{\max} = 2.60$nm; (b) $u = -0.85$ nm; (c) $u = -2.22$ nm; and (d) $u = -4.29$ nm.

from a lower indentation depth, either dislocation nucleation is easier (there is more room for new dislocations to form) or glide of dislocations that have been nucleated during loading is assisting plastic deformation. A couple of observations can be made by looking again at the pressure–displacement curves in Fig. 5.5: (1) the curve for the reference simulation at large imprinting depth

shows strain-hardening, which is an indication that, probably due to proximity to the bottom of the crystal, dislocation activity decreases; (2) upon retraction of the template, deviation from elasticity occurs for the simulation with lower imprinting depth at a much lower pressure (in absolute value) than during imprinting, and at a lower pressure than for the reference simulation. Both observations point towards the fact that a larger density of dislocations is present at the end of loading for the crystal indented at smaller depth. These dislocations are available to slip and thereby decrease the stress state and prevent the formation of a crack.

Note that these results are in disagreement with previous simulations of metal nanoimprinting by (Hsieh and Sung, 2007) and (Fang et al., 2009) who consistently found imprints upon retraction of the template. The reason for this disagreement seems to origin from the smaller and thus more realistic speed of retraction of the template used in this work compared to previous work on nanoimprinting. For a larger retraction velocity also our simulations consistently give a crack.

5.4 Competition between cracks and dislocations: the unexpected relevance of thermal fluctuations

5.4.1 A different crystal orientation

In this section the reference simulation is compared with a simulation that differs only by the orientation of the imprinted gold crystal. The new crystal is still indented in the [001]-direction but is now rotated such that the [110]-direction is along the x-axis, and the $[\bar{1}10]$-direction along the y-axis. Since the plane strain direction lies on a [111] slip plane, dislocations are now more effectively oriented to decrease the stress state caused by the imposed loading. The dimensions of this periodic crystal are negligibly different from those in the reference configuration, i.e. $L_{\mathrm{x}} = 14.99$ nm, $L_{\mathrm{y}} = 2.88$ and $L_{\mathrm{z}} = 7.95$ nm, corresponding to 104, 20 and 40 atomic planes, respectively.

Ten different realizations are carried out for this orientation and unexpected results are observed: some of the realizations have as outcome an imprint others no imprint.

The crystals after full retraction of the template are shown in Fig. 5.7. The atoms are colored by symmetry-index, according to the Atomic Environment Type (AET) method described in Appendix B. Green atoms are classified as having FCC local crystallinity, red atoms HCP, blue BCC, and black atoms

have no classified local crystal symmetry. An atom with local crystallinity FCC is an atom that resides in the B plane of an A-B-C (111) stacking, HCP means that the atom is in the B plane of an A-B-A (111) stacking and a BCC atom has the usual 8-neighbor BCC crystallinity.

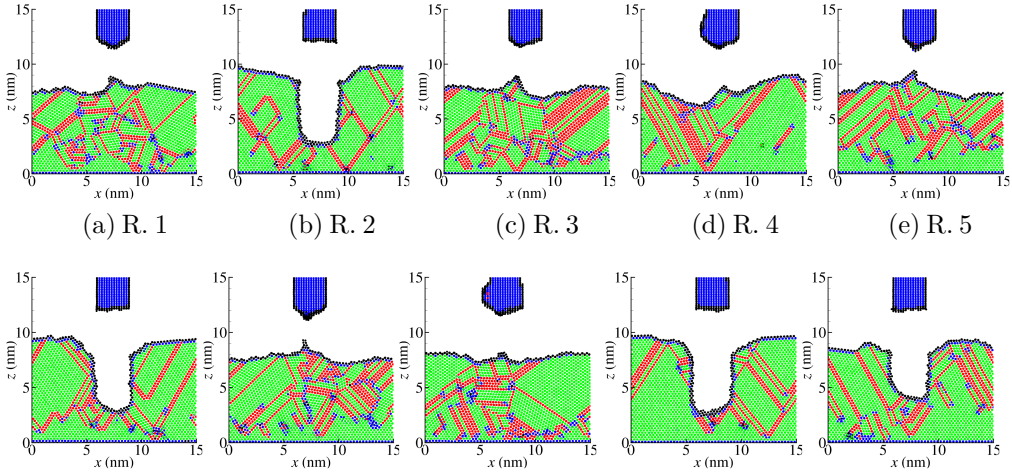

(a) R. 1 (b) R. 2 (c) R. 3 (d) R. 4 (e) R. 5

(f) R. 6 (g) R. 7 (h) R. 8 (i) R. 9 (j) R. 10

Figure 5.7. Crystals oriented with the [110]-direction along the x-axis and the $[\bar{1}10]$-direction along the y-axis after full retraction of the template. The atoms are colored according to their symmetry index. Realizations differ only by the initial atomic velocities.

Four out of ten crystals retain the imprint, and one of these imprints, in Fig. 5.7 (j), is less deep than the other three. Clearly the difference between these realizations is much more than small variations in the profiles. What do we learn from these figures? The fact that realizations differing only by the initial atomic velocities result in such a different mechanical response is surprising. It indicates that local thermal fluctuations affect the local stress state and local atomic mobility at the point that they determine whether or not a crack will nucleate or plastic deformation will take place. The coloring by symmetry index allows us to see more dislocations (two adjacent red lines of atoms) and twinning (one line of red atoms) in the crystals without a retained imprint. In those crystals separation of the crystal from the indenter occurs through ductile necking instead of through a crack.

The pressure–displacement curves for realization 1 (no imprint) and 2 (imprint) are compared in Fig. 5.8(a) with each other and with the reference simu-

lation shown earlier. Figure 5.8(b) shows for all three simulations the evolving number of HCP atoms. The location of the HCP atoms at five different imprinting depths, indicated in Fig. 5.8 with capital letters, are presented in Fig. 5.9 for realization 1 (top raw) and realization 2 (bottom raw). Differences

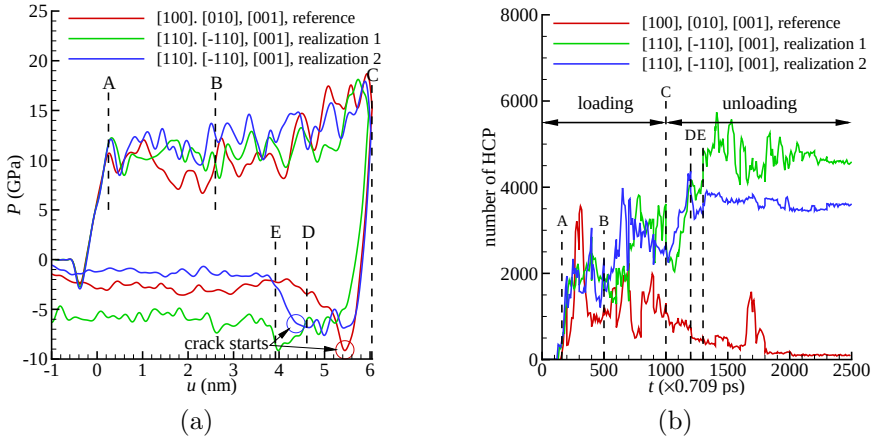

Figure 5.8. (a) Pressure–displacement curves for realization 1 (no imprint) and 2 (imprint) compared with the reference simulation (imprint). (b) Number of atoms with local crystallinity HCP.

in the loading part of the pressure-displacement curves are minor: yielding of the reference crystal occurs at a slightly smaller indentation depth, and hardening occurs in all crystals at about 4 nm imprinting depth. We can therefore conclude that hardening at larger imprinting depth is not a characteristic feature of simulations that lead to an imprint, contrary to what one could have inferred from the results in the previous section. More importantly, we can conclude that the global mechanical behavior of the crystal during loading does not determine whether or not there will be an imprint during unloading. What seems to be very relevant instead is the local stress distribution characteristic of the specific dislocation structure that develops in the crystal as a consequence of local thermal fluctuations.

During loading the number of dislocations, indicated roughly by the count of HCP atoms in Fig. 5.8(b), becomes significantly larger for the two crystals in the new orientation. In Fig. 5.9 it is possible to see that dislocations on the (111) slip planes nucleate just below the indenter for small imprinting depth (see Fig. 5.9(a1)(b1) and (a2)(b2)) while at maximum imprinting depth dislocations are also present beside the indenter. This implies that even though

new dislocations are generated at larger indentation depth, their effectiveness in decreasing the stress state underneath the indenter is apparently limited, and therefore the pressure increases.

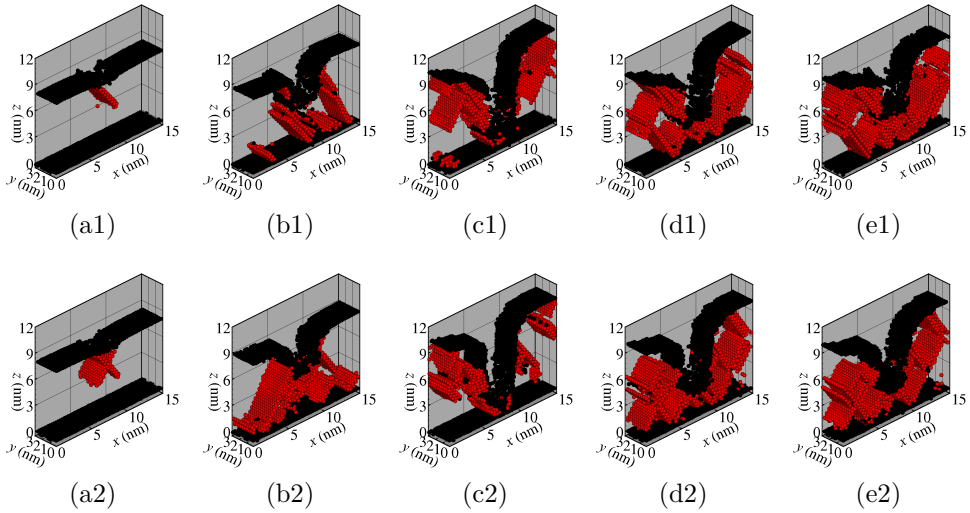

Figure 5.9. Snapshots of the atomic configurations corresponding to points A, B, C, D, E in Fig. 5.8. On the top row the figures represent realization 1 (no imprint), on the bottom row realization 2 (imprint). Red atoms have local crystallinity HCP, black atoms are unclassified. Atoms with FCC local crystallinity are not drawn in the figure.

It is interesting to observe in Fig. 5.8(a) that there is a difference in the slope of the initial unloading curves between the simulation that gives rise to a crack and the ones that do not. Initial elastic unloading is typical of the simulations that lead to a crack, while an immediate deviation from elasticity is characteristic of the crystals where the competition is won by dislocation plasticity. In the curve showing the count of HCP atoms this immediate plasticity corresponds to a sudden drop of the HCP atoms only for the case that leads to no imprint (green curve). This again indicates that in the cases where the imprint forms, dislocations that have nucleated during loading are available to glide and partly release the high stress concentration that would otherwise lead to a crack. Only in some case dislocations formed during loading are in a convenient location to become sufficiently effective in the release of the stress below the indenter.

In the reference orientation the crack nucleates almost immediately after

retraction of the indenter (see Fig. 5.8(a)), while in the new orientation there is plastic activity up to about $u = 4.4$ nm. This is visible in terms of an increase in the number of HCP atoms in Fig. 5.8(b) as well as in Fig. 5.9(d1) and (d2). When contrasting these two figures one also notices that a smaller number of HCP atoms is present underneath the indenter in the crystal that will give rise to a crack (d2).

For a better understanding of the deformation mechanisms taking place upon retraction of the indenter in two realization with different outcome, Fig. 5.10 shows at $u = 4.61$ nm (point D), thus at maximum imprinting depth, realization 1 (no imprint) on the top row and realization 2 (imprint) on the bottom row. The coloring scheme in Fig. 5.10 (a1) and (a2) indicates atomic neighbor changes (see details of the method in Appendix C) having occured in the previous displacement interval $\Delta u = 0.34$ nm. If a dislocation, or a partial dislocation, has passed over a slip plane between displacement u and $u - \Delta u$, the atoms in the (111) planes on either side of the slip plane will have changed their neighbors. In the figure this is visible as pairs of equally colored lines of atoms. In order to distinguish between the passage of a full dislocation and a partial dislocation we also plot in Fig. 5.10 (b1) and (b2) the change in local crystallinity: red indicates atoms that underwent a change from FCC to HCP local crystallinity and blue from HCP to FCC. Green are all atoms that did not undergo such a change. The glide of a full dislocation would not be detected in Fig. 5.10 (b1) and (b2) while the movement of a partial dislocation will give rise to a change from HCP to FCC or viceversa. Figures 5.10 (c1) and (c2) show again the local crystallinity at maximum imprinting depth, but here in a front view of the crystal. On the right the figures show the σ_{zz} stress distribution, relevant for normal opening of the crack. Comparison of Fig. 5.10 (a1) and (a2) with (b1) and (b2) reveals that plastic deformation takes place through motion of partial dislocations, while the contribution of full dislocations is negligible in this displacement interval. Dislocations in the two configurations have clearly nucleated at different locations, and realization 1 has, just below the indenter, a larger number of atoms with local crystallinity different from FCC than realization 2 (contrast Fig. 5.10(c1) with (c2)). This entails that in the case of realization 1 plastic activity has been more effective in decreasing the stress below the indenter than in realization 2. Confirmation of this can be found by comparing Fig. 5.10(d1) with (d2): in realization 2 the stresses are highly localized below the indenter and this stress concentration is relieved by crack nucleation and opening. This can be seen in Fig. 5.11 where the changes in atomic neighbors and local crystallinity between $u = 4.27$ and $u = 3.92$ nm together with the local crystallinity and the stress state are

reported for $u = 3.92$ nm, thus immediately after formation of the crack in realization 2. Particularly noteworthy is that there has been more dislocation partials moving between $u = 4.27$ and $u = 3.92$ nm in the crystal that leads to no crack than the one that leads to a crack, in agreement with the hypothesis that crack nucleation is prevented by dislocation glide, when dislocations are available and properly located.

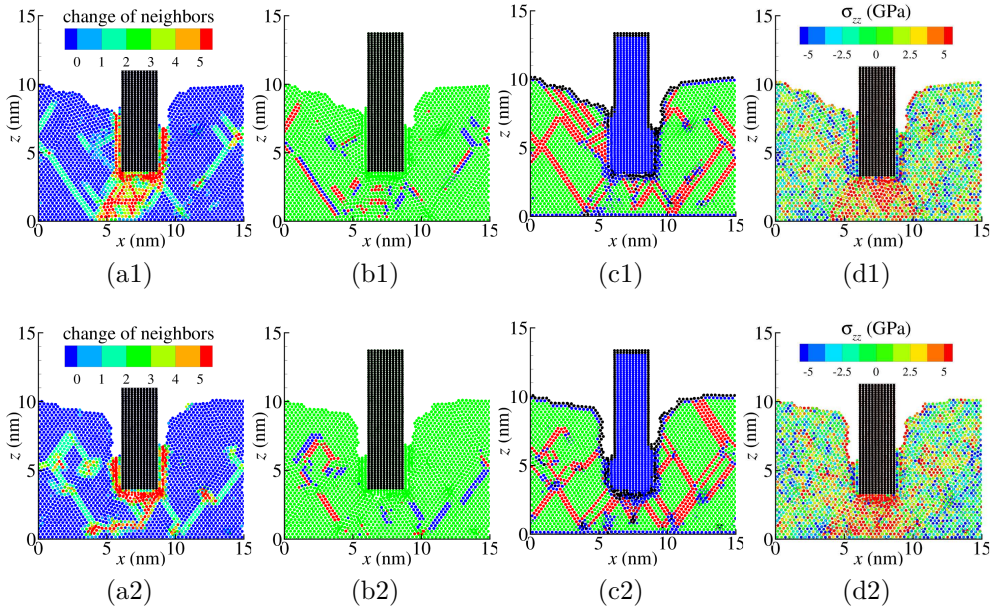

Figure 5.10. Snapshot taken at $u = 4.61$ nm for a crystal that leads to an imprint (top row) and one that leads to no imprint (bottom row). The colors in the figure indicate ((a1) and (a2)) atomic neighbor changes between $u = 4.61$ and $u = 4.27$ nm; ((b1) and (b2)) change in local crystallinity between $u = 4.61$ and $u = 4.27$ nm; ((c1) and (c2)) local crystallinity ; ((d1) and (d2)) σ_{zz}.

Can we conclude from the simulations in this section that the dependence of the final imprint on initial velocities is specific for this crystal orientation? We will show in the following section that the answer to this question is no.

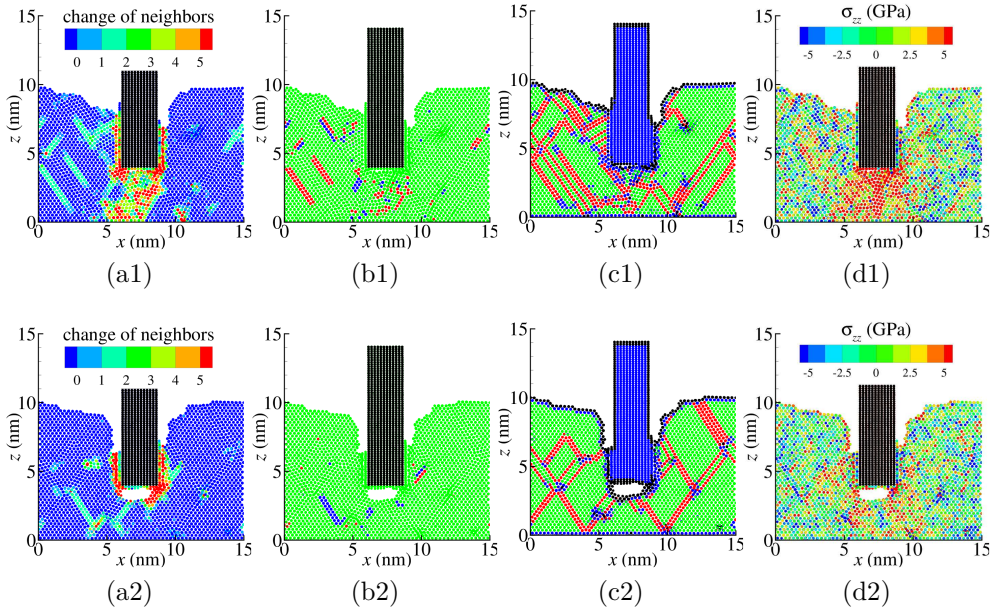

Figure 5.11. Snapshot taken at $u = 3.92$ nm for a crystal that leads to an imprint (top row) and one that leads to no imprint (bottom row). The colors in the figure indicate ((a1) and (a2)) atomic neighbor changes between $u = 4.27$ and $u = 3.92$ nm; ((b1) and (b2)) change in local crystallinity between $u = 4.27$ and $u = 3.92$ nm; ((c1) and (c2)) local crystallinity; ((d1) and (d2)) σ_{zz}.

5.5 Probability of obtaining an imprint

In section 5.3.1 we have analyzed the reference simulation for which we obtained an imprint for all ten realizations. The reference simulation is listed in Tbl. 5.1 as simulation 1. The table presents an overview of the outcome (imprint or no imprint) of all simulations performed in this study. Apart from varying imprinting depth and crystal orientation we have also varied crystal dimensions and temperature.

As already discussed in section 5.4.1 of a crystal oriented such that the (111) plane contains the periodic y-direction, four out of ten realizations lead to a final imprint (simulation 2 in the table). This crystal orientation in combination with the imposed periodic boundary conditions favors dislocation nucleation, therefore there is a large probability that an imprint does not

Table 5.1. Probability of obtaining an imprint for various crystal orientations, unit cell dimensions and imprinting depths. The length unit is nanometer.

simulation	orientation	L_x	L_y	L_z	u_{max}	imprints/runs
1	[100], [010], [001]	15.09	2.85	7.95	6.04	10/10
2	[110], [$\bar{1}$10], [001]	14.99	2.88	7.95	6.04	4/10
3	[100], [010], [001]	15.09	2.85	7.95	2.60	2/10
4	[110], [$\bar{1}$10], [001]	14.99	2.88	7.95	2.60	0/5
5	[100], [010], [001]	15.09	2.85	15.70	6.04	7/10
6	[110], [$\bar{1}$10], [001]	14.99	2.88	15.70	6.04	0/10
7	[110], [$\bar{1}$10], [001]	14.99	10.38	7.95	6.04	8/10
8	[110], [$\bar{1}$10], [001]	30.17	2.88	7.95	6.04	5/10

develop. When the crystals are imprinted to a smaller depth the probability of obtaining an imprint decreases for both crystal orientation tested (see simulation 3 and 4). At large imprinting depth, the proximity of indenter and bottom of the crystal is a limiting factor to dislocation nucleation and slip, and therefore crack formation upon unloading is more likely to occur. To test this hypothesis, simulations 5 and 6 were performed, which differ from simulations 1 and 2 only in the double height of the crystal, i.e. L_z=15.70 nm. The results of these simulations confirm that for both crystal orientations a larger spacing between indenter surface and bottom of the crystal at maximum imprinting depth leads to a smaller probability of obtaining an imprint.

Simulation 7 differs from simulation 2 in that the crystal thickness L_y is more than three times as large. As previously mentioned, the periodic y-direction lies in a (111) plane in this orientation. When L_y is very small this can lead to an artifact: nucleation of dislocations is facilitated by the periodicity and therefore affect the competition between dislocations and crack. Indeed simulation 7 shows a much higher incidence of crack formation than simulation 2 (8/10 instead of 4/10).

Simulation 8 differs from simulation 2 only in the double width of the unit cell, L_x=30.17 nm. This larger unit cell width, which also corresponds to a larger spacing between periodic indenters, has a negligible effect on the results: the probability of finding an imprint is 5/10.

Finally, it is important to mention that all the simulations reported here lead to an imprint if they are performed at 10 K instead of at 300 K. This

confirms that the competition between cracks and dislocations is driven by thermal fluctuations and that, as expected, reducing the temperature leads to brittle material behavior.

5.6 Conclusions

Molecular dynamics simulations are carried out to study the mechanical nanoimprinting of gold crystals by means of a template with the shape of an egg slicer. The majority of the simulations show that upon unloading there is a competition between crack formation and plastic deformation through the movement of dislocation partials. The exact location where dislocation nucleate turns out to be determined not only by the local stress state but also by local thermal fluctuations. Upon unloading, the density and location of dislocation partials, nucleated during loading, determine whether stress relaxation will occur through plastic deformation or through crack nucleation and propagation. Also here thermal fluctuations prove to be important. Even in exactly the same configurations just prior to unloading, differences in the instantaneous velocity fluctuations map may lead to plastic deformation (no imprint) or to crack nucleation and propagation (imprint) upon unloading. For crystals where the dislocation density after loading is largest, the probability of finding an imprint after unloading is smallest. This is the reason why crystals oriented such that the (111) plane contains the in-plane periodic direction, are less likely to lead to an imprint than crystals with other orientations.

The probability of finding an imprint decreases with decreasing indentation depth and generally increases with increasing dimensions of the unit cell of analysis.

A confirmation that the competition between cracks and dislocations is driven by thermal fluctuations comes from the fact that if any of the simulations presented here is repeated at 10 K the material behaves consistently in a brittle manner.

Appendix A

In this study we use the EAM potential by Zhou et al. (Zhou et al. (2004)). For convenience we give the full set of definitions and parameters. The total energy E of a configuration of atoms is defined as the sum of pair energies ϕ and embedding energies F,

$$E = \frac{1}{2} \sum_{i,j,i \neq j} \phi_{ij} + \sum_i F_i \tag{5.2}$$

For a single element the pair energy ϕ is a double exponential function of the distance r_{ij} between atom i and j,

$$\phi(r) = \frac{Ae^{-\alpha(r/r_e-1)}}{1+(r/r_e-\kappa)^{20}} - \frac{Be^{-\beta(r/r_e-1)}}{1+(r/r_e-\lambda)^{20}} \tag{5.3}$$

where A, B, α and β are adjustable parameters, r_e is the equilibrium distance between nearest neighbors, and κ and λ are cutoff parameters.

The embedding energy F_i is a function of the electron density ρ_i at the location of atom i, where ρ_i is built up from density contributions from the surrounding atoms,

$$\rho_i = \sum_{j,j \neq i} f_j(r_{ij}). \tag{5.4}$$

Here $f_j(r)$ is the electron density supplied by an atom of chemical element j at a distance r. This function has the same form as the attractive term of the pair potential (but without the minus sign) and with the same parameters β, r_e, and λ,

$$f(r) = \frac{f_e e^{-\beta(r/r_e-1)}}{1+(r/r_e-\lambda)^{20}}. \tag{5.5}$$

The parameter f_e is an additional adjustable parameter for each element. The pair potential function for two different elements a and b is expressed as

$$\phi^{ab}(r) = \frac{1}{2}\left[\frac{f^b(r)}{f^a(r)}\phi^{aa}(r) + \frac{f^a(r)}{f^b(r)}\phi^{bb}(r)\right]. \tag{5.6}$$

Finally, the embedding energy function $F(\rho)$ is built up over different ranges

Table 5.2. EAM potential parameters for gold and tungsten by Zhou *et. al.* (Zhou et al., 2004).

	r_e (Å)	ρ_e (e/Å^3)	ρ_s (e/Å^3)	α	β	A (eV)	B (eV)
Au	2.885034	19.991632	19.991509	9.516052	5.075228	0.229762	0.356666
W	2.740840	37.234847	37.234847	8.900114	4.746728	0.882435	1.394592
	κ	λ	f_e (e/Å^3)	F_{n0} (eV)	F_{n1} (eV)	F_{n2} (eV)	F_{n3} (eV)
Au	0.356570	0.748798	1.529021	-2.937772	-0.500288	1.601954	-0.835530
W	0.139209	0.278417	3.487340	-4.946281	-0.148818	0.365057	-4.432406
	F_0 (eV)	F_1 (eV)	F_2 (eV)	F_3 (eV)	F_e (eV)	η	
Au	-2.98	0	1.706587	-1.134778	-2.978815	1.021095	
W	-4.96	0	0.661935	0.348147	-4.961306	-0.582714	

of the electron density,

$$\begin{aligned} F(\rho) &= \sum_{i=0}^{3} F_{ni} \left(\frac{\rho}{\rho_n} - 1 \right)^i, && \rho < \rho_n, \qquad \rho_n = 0.85\rho_e \\ F(\rho) &= \sum_{i=0}^{3} F_i \left(\frac{\rho}{\rho_e} - 1 \right)^i, && \rho_n \leq \rho < \rho_0, \quad \rho_0 = 1.15\rho_e \\ F(\rho) &= F_e \left[1 - \ln \left(\frac{\rho}{\rho_s} \right)^\eta \right] \left(\frac{\rho}{\rho_s} \right)^\eta, && \rho_0 \leq \rho. \end{aligned} \tag{5.7}$$

In these equations, ρ_e is the equilibrium electron density, i.e. the electron density at an atom in the equilibrium crystal of the element. The full parameter set for gold and tungsten is given in Tbl. 5.2.

Appendix B

In order to assign a local crystal structure to every individual atom, we use the so-called Atomic Environment Type (AET), discussed by Timonova (**?**). The AET of atom i is defined by the direction vectors that connect i to its z neighboring atoms j. One way to express the AET of atom i is through the rotationally invariant parameters $w_i^{(l)}$, which were expressed by Steinhardt *et al* (Steinhardt et al., 1983) as

$$w_i^{(l)} = \frac{4\pi}{2l+1} \sum_{m=-l}^{l} \left| \sum_j Y_{(m)}^{(l)}(\theta_{ij}, \phi_{ij}) \right|^2, \qquad l = 0, 1, 2 \ldots \tag{5.8}$$

Table 5.3. Reference values $Q_{\mathrm{ref}}^{(l)}$ for different crystal structures.

l		2	4	6	8	10	12
$Q_{\mathrm{ref}}^{(l)}$	FCC	0.000	0.191	0.575	0.404	0.013	0.600
	HCP	0.000	0.097	0.485	0.317	0.010	0.565
	BCC	0.000	0.036	0.511	0.429	0.195	0.405

where $Y_{(m)}^{(l)}$ is the l, m spherical harmonic function and θ_{ij}, ϕ_{ij} are respectively the polar and azimuthal angles of the ij-vector with respect to the z-direction. Here we use slightly differently normalized parameters $Q_i^{(l)}$, defined as

$$Q_i^{(l)} \equiv \frac{\sqrt{w_i^{(l)}}}{z}. \tag{5.9}$$

For each atom i the actual values of $Q_i^{(l)}$ are calculated for $l = 2, 4, 6, 8, 10, 12$ and compared with the corresponding numbers $Q_{\mathrm{ref}}^{(l)}$ in selected reference crystal structures, of which the values are listed in Tbl. 5.3. The difference between the actual angular environment of atom i, $Q_i^{(l)}$, and the angular environment of an atom in each of the reference structures $Q_{\mathrm{ref}}^{(l)}$ is calculated as an rms difference,

$$\Delta S_i = \sqrt{\frac{1}{6}\sum_{\lambda=1}^{6}\left(Q_i^{(2\lambda)} - Q_{\mathrm{ref}}^{(2\lambda)}\right)^2}. \tag{5.10}$$

We consider the local structure of atom i as sufficiently similar to a specific reference structure if for that structure ΔS_i is smaller than for other reference structures and if the value of ΔS_i is less than 0.11. If not, the local structure around atom i is considered 'unclassified'.

Note that in the calculation of the direction angles in Eq.(5.8) the coordinates of the atoms are not used as they actually are. Instead, the position of each atom is replaced by the average position of its neighboring atoms. This has the effect of filtering out a substantial part of the thermal vibrations in the atomic coordinates. A small disadvantage is that the method produces biased results for surface atoms. Note that average coordinates are used in the calculations only, not in the structural displays of the atoms.

Appendix C

To analyze structural changes taking place in a simulation, we make use of a quantity N_c, the number of neighbor changes of an atom. N_c is defined for every atom i in a certain time interval Δt as the number of neighbor atoms that i has lost in the interval plus the number of new neighbor atoms that i has gained. In an FCC crystal, therefore, the theoretical maximum value of N_c is 24. To illustrate this with an example, suppose that at the beginning of a time interval an atom has neighbors with numbers 5, 72, 103 and 188, and at the end it has neighbors with numbers 2, 5, 72, 105, and 188, then $N_c = 3$: neighbor 103 was lost, and neighbors 2 and 105 were gained.

References

Berendsen, H.J.C., Postma, J.P.M., van Gunsteren, W.F., DiNola, A., Haak, J.R., 1984. Molecular dynamics with coupling to an external bath. J. Chem. Phys. 81, 3684–3690.

Buzzi, S., Robin, F., Callegari, V., Löffler, J.F., 2008. Metal direct nanoimprinting for photonics. Microelectron. Eng. 85, 419–424.

Cheng, M.C., Sung, C.K., Wang, W.H., 2007. The effects of thin-film thickness on the formaton of metallic patterns by direct nanoimprint. J. Mater. Process. Technol. 191, 326–330.

Choi, Y., Van Vliet, K.J., Li, J., Suresh, S., 2003. Size effects on the onset of plastic deformation during nanoindentation of thin films and patterned lines. J. Appl. Phys. 94, 6050–6058.

Daw, M.S., Baskes, M.I., 1984. Embedded-atom method: derivation and application to impurities, surfaces, and other defects in metals. Phys. Rev. B 29, 6443–6453.

Fang, T.H., Wu, C.D., Chang, W.J., Chi, S.S., 2009. Effect of thermal annealing on nanoimprinted Cu-Ni alloys using molecular dynamics simulation. Appl. Surf. Sci. 255, 6043–6047.

Hagelaar, J.H.A., Bitzek, E., Flipse, C.F.J., Gumbsch, P., 2007. Atomistic simulations of the formation and distruction of nanoindentation contacts in tungsten. Phys. Rev. B 73, 045425.

Hsieh, C.W., Sung, C.K., 2007. Atomic-scale friction in direct imprinting process: molecular dynamics simulation. Jpn. J. Appl. Phys. 46, 6387–6390.

Hsu, Q., Wu, C., Fang, T., 2005. Studies on nanoimprint process parameters of copper by molecular dynamics analysis. Comput. Mater. Sci. 34, 314–322.

Lazić, I., 2009. Atomic scale simulation of oxide and metal film growth. Ph.D. thesis. Delft University of Technology.

Neighours, J.R., Alers, G.A., 1958. Elastic constants of silver and gold. Phys. Rev. 111, 707–712.

Pei, Q.X., Lu, C., Liu, Z.S., Lam, K.Y., 2007. Molecular dynamics study on the nanoimprint of copper. J. Phys. D: Appl. Phys. 40, 4928–4935.

Steinhardt, P.J., Nelson, D.R., Ronchetti, M., 1983. Bond-orientational order in liquids and glasses. Phys. Rev. B 28, 784–805.

Wu, C.D., Fang, T.H., Sung, P.H., Hsu, Q.C., 2012. Critical size, recovery, and mechanical property of nanoimprinted Ni-Al alloys investigation using molecular dynamics simulation. Comput. Mater. Sci. 53, 321–328.

Yao, C., Wu, C., Sung, C., 2008. Effects of thin film properties on metallic pattern formation by direct nanoimprint. J. Mater. Process. Technol. 201, 765–769.

Yao, C.H., Chang, C.H., Hsieh, C.W., Sung, C.K., 2010. Effects of mold shape and sidewall roughness on nanoimprint by molecular dynamics simulation. Microelectron. Eng. 87, 864–868.

Youn, S.W., Ueno, A., Okuyama, C., Takagi, H., Takahashi, M., Maeda, R., 2009. Direct imprint of Al foil for metallization of high-aspect ratio al lines in nano/micro patterned SiO_2/Si. Microelectron. Eng. 86, 600–603.

Zhang, J., Zhang, Y., Mara, N., Lou, J., Nicola, L., 2013. Direct nanoimprinting of single crystalline gold: Experiments and dislocation dynamics simulations. Appl. Surf. Sci. .

Zhou, X.W., Johnson, R.A., Wadley, H.N.G., 2004. Misfit-energy-increasing dislocations in vapor-deposited CoFe/NiFe multilayers. Phys. Rev. B 69, 1–10.

Chapter 6

Lattice rotation caused by wedge indentation of a single crystal: dislocation dynamics compared to crystal plasticity simulations

Abstract

A number of recent experimental efforts such as electron back scattering technique and three-dimensional x-ray structural microscopy have revealed the intriguing formation of sectors of lattice rotation fields under indentation. In the case of wedge indentation, the in-plane rotation changes sign from one sector to another. Although the lattice rotation fields can be used to compute the geometrically necessary dislocation (GND) densities, it remains unclear how these sectors can be related to the hardness and therefore to the indentation size effects, i.e., the increase of indentation hardness with the decrease of indentation depth. Crystal plasticity simulations in this work reproduce the experimental findings at large indentation depth. On the contrary, discrete dislocation plasticity can only capture the sectors found experimentally when there is a high obstacle density and large obstacle strength. Obstacle density and strength, however, have little effect on the hardness. In other words, there is no one-to-one correspondence between the lattice rotation patterns and the indentation size effects. The presence of obstacles favors the dislocation arrangements that lead to the experimentally found rotation sectors. Using the similarity solutions of indentation fields and the solution of localized deformation fields near a stationary crack, a simple model is developed that explains the dislocation pattern evolution, its relationship to the lattice misorientations, and more importantly its dependence on obstacles.

6.1 Introduction

The inelastic deformation of crystalline materials has been found to be scale dependent. For instance, the material hardness increases with the decrease of the indentation depth for a wide range of crystalline materials (Pharr et al., 2010). These experimental findings have motivated the development of a number of continuum strain-gradient plasticity theories, most of which are based on the concept of geometrically necessary dislocations (GNDs) (Fleck et al., 1994; Gudmundson, 2004; Gurtin, 2002; Nix and Gao, 1998). During plastic

This chapter is accepted as:
Y. Zhang, Y. Gao and L. Nicola. Lattice rotation caused by wedge indentation of a single crystal: dislocation dynamics compared to crystal plasticity simulations. J. Mech. Phys. Solids

deformation, dislocations may be generated and arrested by forest hardening processes, leading to statistically stored dislocations (SSDs), while GNDs are required for compatible deformation of the crystal lattice. Although these theories have successfully captured the size dependence of the indentation hardness, the predictive capabilities of these models clearly rely on validations by measurement of the dislocation microstructure.

Such microstructure can be indirectly determined from the measurements of lattice misorientation fields, using the electron back scatter diffraction (EBSD) technique which measures the surface orientation (Kysar et al., 2007; Saito and Kysar, 2011; Saito et al., 2012) or three-dimensional x-ray structural microscopy which is a non-destructive bulk measurement (Barabash et al., 2010a,b; Larson et al., 2007; Yang et al., 2004). Both techniques will give submicron resolutions and thus are ideal for the indentation size effect study. The measured lattice orientation and lattice curvature fields can be used to evaluate Nye's dislocation density tensor (Nye, 1953), and the GND density (Arsenlis and Parks, 1999; Kysar et al., 2010; Larson et al., 2007). Both techniques have revealed the formation of sectors of positive and negative rotations under wedge/Berkovich/spherical indentations. Recently, crystal plasticity simulations have been performed (Bouvier and Needleman, 2006; Saito and Kysar, 2011; Saito et al., 2012), that have successfully reproduced the sectors under blunt wedge indentation. Since these simulations are based on continuum size-independent plasticity, the rotation sectors seem to be unrelated to the indentation size effects.

Discrete dislocation plasticity (DDP) is a numerical technique that allows to capture size dependent plasticity by virtue of the intrinsic length it contains, the dislocation Burgers vector. DDP simulations of indentation of thin films presented by Balint *et al.* (Balint et al., 2006) were indeed able to predict an ISE in good agreement with the Nix-Gao law. Such agreement is an indication that strain gradients and the related generation of GNDs is a very likely origin of a size effect in their simulations. An additional cause of the predicted ISE is source limitation. In this study we will consider a broad range of dislocation source densities. For the smaller source densities source limitation is expected to be the main origin of the size effect, while for the larger source densities, strain gradients and GNDs are expected to give the main contribution.

In this paper we are interested in the role of dislocation source density, obstacle density and strength, and crystallographic orientation on the hardness and on the lattice rotation sectors. Results presented in this paper confirm that in DDP simulations there is no one-to-one correspondence between the lattice rotation sectors and hardness variations, so there is also no correspon-

dence between misorientation sectors and size effects. Assuming that DDP is capable of capturing all mechanisms that cause an ISE in experiments, the lattice rotation measured experimentally can also not be related to the ISE. The lattice rotation sectors measured experimentally can be coupled to material hardness only at a sufficiently large indentation depth, where hardness is size independent. Unexpectedly, in absence of dislocation obstacles, even with a large density of dislocation sources, the discrete dislocation plasticity simulations could not capture the four rotation sectors predicted at large indentation depth experimentally and by the crystal plasticity simulations. Obstacles are the crucial ingredient that determines the dislocation microstructure that leads to the four rotation sectors.

A micromechanical model is developed to explain this finding and insights on mechanisms of indentation size effects are also discussed.

6.2 Model

A metal single crystal indented by a rigid wedge with tip angle $\omega = 170^\circ$ is modeled in two dimensions considering plane strain conditions (see Fig. 6.1). The crystal is indented along the $[0\bar{1}0]$-direction. Figure 1(a) shows the geometry of the FCC crystal. The plane on which the 2D analysis is carried out is the $(10\bar{1})$ plane. The figure indicates the slip planes of easy glide and the dislocation loops. The x_1-axis is taken along the [101]-direction, the x_2-axis along the [010]-direction and the x_3-axis along the $[10\bar{1}]$-direction. For an FCC crystal dislocations glide occurs on the (111) planes and the slip directions are the face diagonals of the crystal. In order to be consistent with our assumption of plane strain deformation, in the case of the (111) plane simultaneous slip should occur along the $[1\bar{1}0]$ and $[0\bar{1}1]$ directions; effectively this means slip in the $[1\bar{2}1]$ direction. The $[1\bar{2}1]$-direction lies in the $(10\bar{1})$ plane inclined at -54.7° with the x_1-axis. Similarly, slip occurs on slip plane $(\bar{1}1\bar{1})$, corresponding to a slip plane trace parallel to the x_1-axis. The only other deformation possibility compatible with plane strain deformation is simultaneous and equal slip in the [101]-direction on slip planes $(\bar{1}11)$ and $(11\bar{1})$. This corresponds to the slip plane trace inclined at 0° with the x_1-axis. The 2D model is presented in Fig. 6.1(b). The slip plane traces are oriented at $\varphi = 0^\circ$ and $\varphi_\pm = \varphi \pm 54.7^\circ$ with the x_1-direction (Rice, 1987).

The indentation velocity is constant $\dot{u} = 4 \times 10^5$ μm/s and sufficiently small to ensure a quasi-static response. Indentation is imposed by prescribing a normal displacement rate along the contact surface S:

$$\dot{u}_1(x_1, h) = 0, \quad \dot{u}_2(x_1, h) = -\dot{u}, \tag{6.1}$$

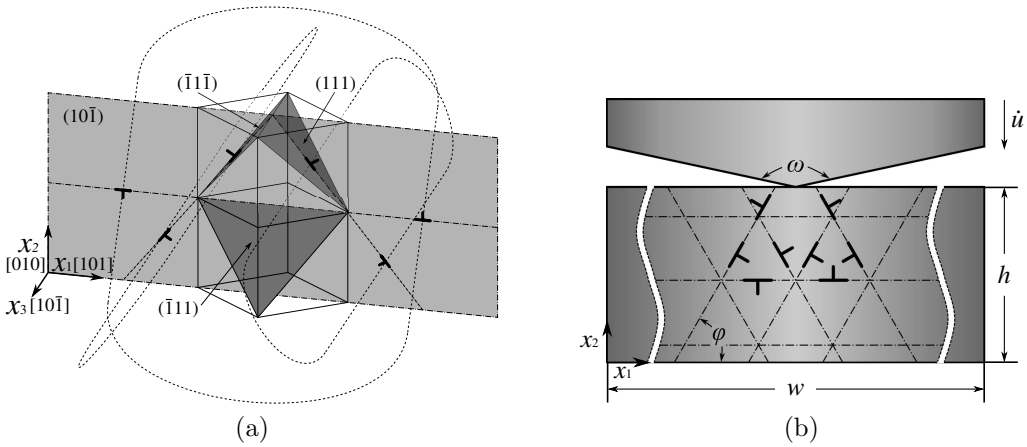

Figure 6.1. (a) Geometry of the FCC crystal indicating the plane of the 2D analysis, the dislocation loops and the planes of easy glide. (b) The corresponding 2D plane strain model of an FCC single crystal indented by a wedge rigid indenter.

where $x_1 \in S$. The contact surface S is defined as the sum of areas where two or more adjacent surface nodes are in contact with the indenter. Note that the first condition in Eq. (6.1) indicates that there is no slip at the contact. The rest of the crystal surface is traction free. Also the vertical boundaries of the crystal are taken to be traction free and sufficiently far away from the contact region, such that the results of indentation are independent of the width of the crystal.

The boundary conditions along the bottom of the crystal are:

$$\dot{\sigma}_{12}(x_1, 0) = 0, \quad \dot{u}_2(x_1, 0) = 0. \tag{6.2}$$

6.2.1 Discrete dislocation plasticity

Following Van der Giessen and Needleman (Van der Giessen and Needleman, 1995), the solution to the boundary value problem formulated in Section 6.2 is obtained by superposing the ($\tilde{}$)-fields that describe analytically the individual dislocations in an infinite medium and the ($\hat{}$)-image fields that correct numerically for the prescribed boundary conditions.

At each time step of the simulation the dislocation structure is updated through a set of constitutive rules that control nucleation, glide, annihilation and pinning of dislocations at point obstacles. Nucleation occurs by activation of Frank-Read sources, which are taken to be initially present in the crystal

and whose density does not change during the simulation. A critical shear stress τ_{nuc} must act on a source for a given time t_{nuc} in order to activate it and form a new dislocation dipole. In some of our simulations, also a given density of obstacles representing precipitates or forest dislocations is initially present in the crystal. The obstacles, characterized by a critical strength τ_{obs}, prevent dislocations from gliding pass them, until the resolved shear stress acting on the pinned dislocation is higher than the obstacle strength. Dislocation sources and obstacles (when present) are randomly positioned on the slip planes and their density is assumed to be constant during the simulation.

After nucleation the dislocations will glide on their slip plane. The velocity of dislocation I, v^I, is taken to be proportional to the Peach-Koehler force f^I acting on the dislocation, according to $f^I = Bv^I$ where B is the drag coefficient.

Dislocation annihilation occurs when opposite-signed dislocations on the same slip plane collide. This is modeled by removing dislocations of opposite sign from the simulation when they are closer to each other than the critical distance L_{ann}. Dislocations can escape from the crystal from the top free surface.

6.2.2 Crystal plasticity

The boundary value problem in section 6.2 is solved by means of size-independent viscoplastic continuum crystal plasticity, following Peirce's formulation and numerical implementation (Peirce et al., 1983). The total strain rate is written as the sum of an elastic and a viscoplastic part

$$\dot{\epsilon}_{ij} = \dot{\epsilon}^{\text{e}}_{ij} + \dot{\epsilon}^{\text{p}}_{ij}. \tag{6.3}$$

The elastic part is described by Hooke's law,

$$\dot{\sigma}_{ij} = \mathcal{L}_{ijkl}\dot{\epsilon}^{\text{e}}_{kl}, \tag{6.4}$$

where $\mathcal{L}_{ijkl}$ is the tensor of isotropic elastic moduli. The plastic part of the strain rate is given by

$$\dot{\epsilon}^{\text{p}}_{ij} = \sum_{\varphi} \dot{\gamma}_{\varphi}\mu^{(\varphi)}_{ij}, \qquad \mu^{(\varphi)}_{ij} = \frac{1}{2}\left[s_i{}^{(\varphi)}m_j{}^{(\varphi)} + s_j{}^{(\varphi)}m_i{}^{(\varphi)}\right], \tag{6.5}$$

where $m_i{}^{(\varphi)}$ and $s_i^{(\varphi)}$ are, respectively, the components of the slip plane normal and the slip direction of slip systems φ and $\dot{\gamma}_{\varphi}$ is the intrinsic slip rate. The

slip rate is given by the power law relation

$$\dot{\gamma}_\varphi = \dot{\gamma}_0 \frac{\tau_\varphi}{g_\varphi} \left| \frac{\tau_\varphi}{g_\varphi} \right|^{(m-1)} , \tag{6.6}$$

with $\tau_\varphi = m_i^{(\varphi)} \sigma_{ij} s_j^{(\varphi)}$ the resolved shear stress on slip system φ; $\dot{\gamma}_0$ is a reference slip rate, m is the strain rate sensitivity exponent and g_φ is the hardness of slip system φ which has initial value τ_0 for all φ and evolves according to

$$\dot{g}_\varphi = h_0 \sum_\varphi |\dot{\gamma}^{(\varphi)}| . \tag{6.7}$$

The finite element discretization uses a mesh of quadrilateral elements, each consisting of four triangles to avoid locking problems associated with near incompressibility.

6.3 Choice of parameters

In all simulations the crystals width is $w = 1000$ μm and its height is $h = 50$ μm. The elastic constants of the crystal are taken to be those of aluminum: $C_{11} = 103.7$ GPa and $C_{12} = 51.1$ GPa, corresponding to shear modulus $G = 26$ GPa and Poisson's ratio $\nu = 0.33$.

In the DDP simulations, to limit simulation time, only the central part of the metal (from $x_1 = 475$ μm to $x_1 = 525$ μm) is taken to behave plastically. If dislocations reach the border of the plastic region the simulation is stopped. The finite element mesh used to compute the image fields is coarse in the region where the material behaves elastically and progressively refined in the region where plasticity can take place. The maximum refinement is in the central region of width 10 μm (wider than the maximum contact size) and height 0.02 μm where the square elements are 0.005 μm $\times$ 0.005 μm. Such a small element size is necessary to reach convergence of the results in terms of real contact area, and therefore hardness, during plastic deformation.

In the discrete dislocation plasticity simulations the dislocation sources are characterized by a critical strength taken from a Gaussian distribution with mean $\bar{\tau}_{\text{nuc}} = 50$ MPa and standard deviation $\tau_{\text{dev}} = 10$ MPa. When the resolved shear stress on the source reaches the critical nucleation strength value for a time span $t_{\text{nuc}} = 10$ ns the source emits a dipole. The drag coefficient is $B = 10^{-4}$ Pa s. The density of point obstacles is $\rho_{\text{obs}} = 98$ μm^{-2} and critical strength $\tau_{\text{obs}} = 150$ MPa.

The crystal plasticity (CP) simulation parameters are chosen to fit as much as possible the discrete dislocation simulations. Initially, simulations are performed to model the uniform compression of the crystal. The strength of the slip systems in the CP simulations that gives the best fit for the yield point was found to be $\tau_0 = 20$ MPa; the initial slip rate was fixed to $\dot{\gamma}_0 = 0.002$ s^{-1} and the rate sensitivity exponent $m = 1/200$. Since the DDP simulations give a non-hardening response after yield the hardening coefficient was initially chosen as small as possible, but large enough to avoid numerical difficulties, i.e. $h_0/\mu = 2.7 \times 10^{-7}$. The finite element mesh is chosen identical to the mesh used for the DDP simulations.

6.4 Crystals without dislocation obstacles

As already shown by Balint *et al.* (Balint et al., 2006) the hardness calculated by the DDP simulations (see Fig. 6.2) is size dependent for small indentation depth. The hardness-displacement curves calculated by DDP converge to the CP results for a source density of about 144 μm^{-2} at $u = 0.22$ μm and approach the classical hardness at $u = 0.4$ μm. Note that the size dependent response is more evident in crystals that have a low dislocation source density. At the indentation depth of $u = 0.4$ μm the hardness of crystals with large source density has already converged to the continuum limit, while the hardness of the crystals with small source density is higher. Here, we will compare

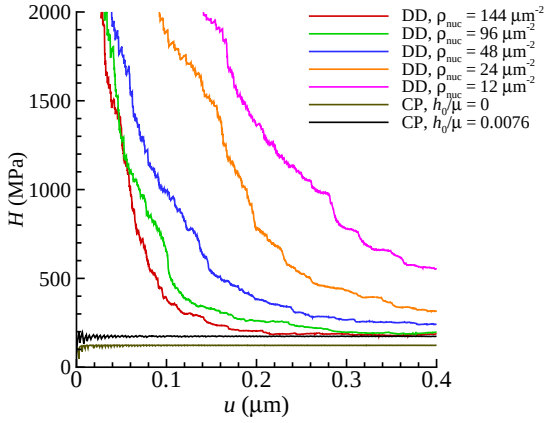

Figure 6.2. Hardness-displacement curves for various dislocation source densities.

the elastic and total lattice rotation obtained by DDP and CP simulations

at final indentation depth, $u = 0.4$ μm. In the DDP simulations the lattice rotation is calculated as

$$\theta = \frac{1}{2}(\hat{u}_{2,1} + \tilde{u}_{2,1} - \hat{u}_{1,2} - \tilde{u}_{1,2}), \tag{6.8}$$

where $\tilde{u}$ is the displacement caused by the dislocations in an infinite medium and $\hat{u}$ is the image displacement that corrects for the boundary conditions.

The elastic lattice rotation is obtained by analytically deriving the displacement fields of every edge dislocation, so that the displacement discontinuities associated with the dislocations, which cause the plastic part of the rotation, are eliminated,

$$\begin{aligned} \tilde{u}_{1,2} &= \frac{b}{2\pi(1-\nu)}\left[\frac{x_1(x_1^2 - {x_2}^2)}{2({x_1}^2 + {x_2}^2)^2} + (1-\nu)\frac{x_1}{x_1^2 + x_2^2}\right] \\ \tilde{u}_{2,1} &= -\frac{b}{2\pi(1-\nu)}\left[\frac{x_1 {x_2}^2}{({x_1}^2 + {x_2}^2)^2} + \frac{1}{2}(1-2\nu)\frac{x_1}{{x_1}^2 + {x_2}^2}\right]. \end{aligned} \tag{6.9}$$

Here, the edge dislocation is located at the origin of the coordinate axes and has Burgers vector in x_1-direction. The total lattice rotation is instead obtained by numerically evaluating Eq. 6.8 at the finite element nodes.

Figure 6.3 shows the elastic lattice rotation calculated by CP (a) and by DDP for (b) $\rho_{\text{nuc}} = 24$ μm^2 and (c) $\rho_{\text{nuc}} = 144$ μm^2. There are no initial obstacles in the DD simulations. There is a remarkable difference between the lattice orientation distribution obtained by CP simulations, that present the expected four misorientation sectors, and the results obtained by DDP, where only two regions with opposite orientation are visible.

As previously shown, the crystal hardness is largely dependent on the source density. However, the source density gives a negligible effect on the formation of elastic lattice rotation sectors as can be seen by contrasting Fig. 6.3(b) and (c). A larger source density leads to a larger dislocation density, as can be seen in Fig. 6.3(d) and (e) but evidently even a larger dislocation density is not sufficient to reproduce the lattice rotation distribution obtained by CP, even though it is sufficient to lead to the same hardness.

6.5 Crystals with dislocation obstacles

In this section the effect of obstacles to dislocation motion is highlighted. To this end, wedge indentation is modeled for single crystals containing a source density of $\rho_{\text{nuc}} = 144$ μm^2 as well as a constant density of dislocation obstacles. These obstacles represent forest hardening caused by deformation preceding

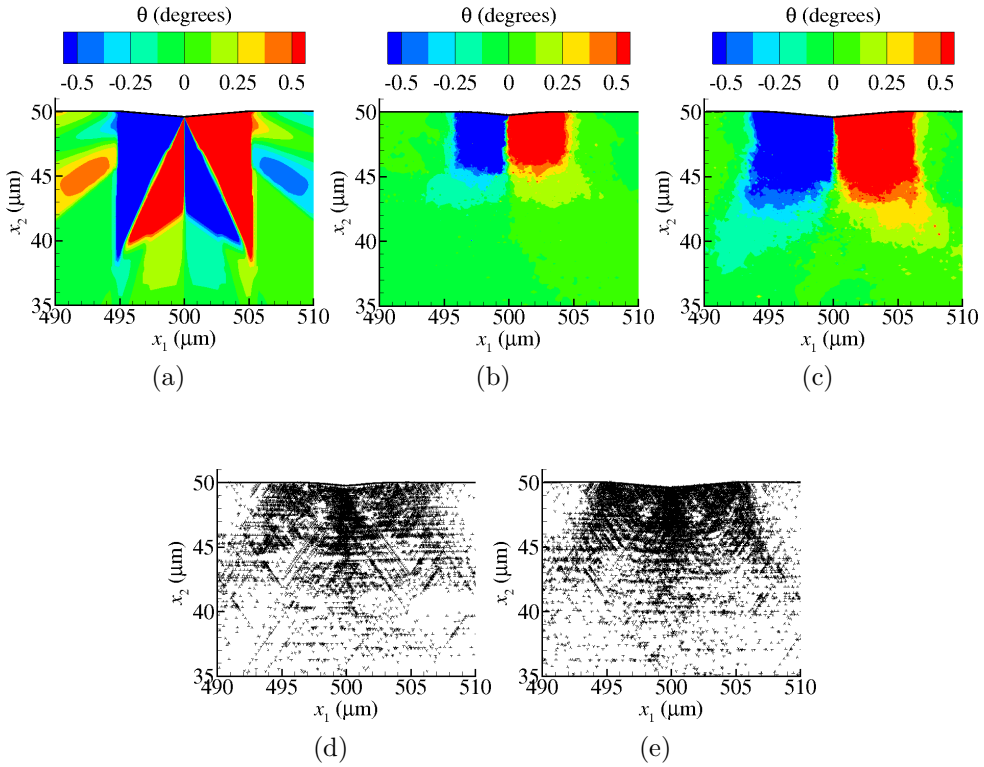

Figure 6.3. The distribution of elastic lattice rotation at $u = 0.4$ μm is calculated by (a) CP and DDP for source density (b) 24 μm^{-2} and (c) 144 μm^{-2}. Dislocations in the plastic region for source density (d) 24 μm^{-2} and (e) 144 μm^{-2}.

indentation, or other defects like hard inclusions in the material. Figure 6.4(a) and (b) show the profile of lattice rotation for two different obstacle densities, i.e. $\rho_{\text{obs}} = 200$ μm^{-2} and $\rho_{\text{obs}} = 400$ μm^{-2}. Unexpectedly, the obstacle density has a major effect on lattice rotation and the difference with the lattice rotation obtained for obstacle free crystals is remarkable (compare Fig. 6.4(a) with Fig. 6.3c). Qualitatively, the lattice mismatch obtained when a distribution of obstacles is present in the crystal resembles the results of crystal plasticity simulations. The localized differences and the fact that the lattice distribution obtained by DDP simulations present less defined sectors are caused by the discreteness intrinsic to the DDP method. It is also very inter-

esting to notice from Fig. 6.4(c) that the hardness is instead only marginally affected by the obstacle densities considered: at $u = 0.4$ μm $H = 180$ MPa for an obstacle-free crystal and $H = 210$ MPa for a crystal with $\rho_{\text{obs}} = 400$ μm^{-2}. Increasing the critical strength of the obstacles from 150 MPa to 1000 MPa

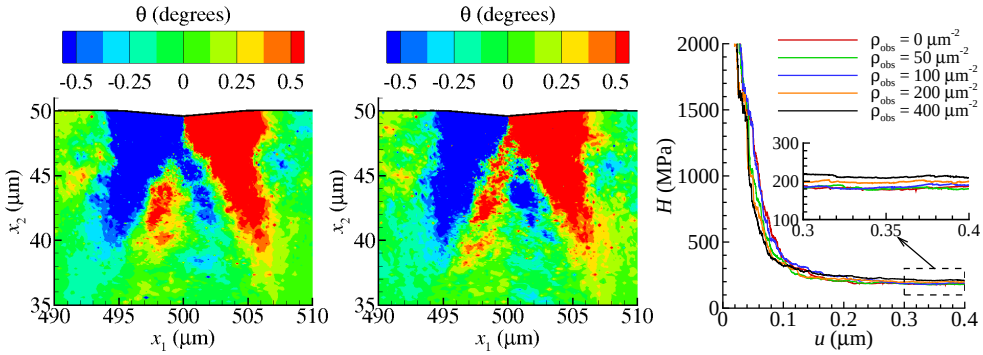

Figure 6.4. The distribution of lattice rotation for (a) $\rho_{\text{obs}} = 200$ μm^{-2} and (b) $\rho_{\text{obs}} = 400$ μm^{-2}, the obstacle strength is for all cases $\tau_{\text{obs}} = 150$ MPa. (c) The crystal hardness for various obstacle density.

does also not affect the calculated hardness and leads to lattice rotation profiles even closer to those obtained by CP (see Fig. 6.5). Clearly, obstacles limit the distance that dislocation can glide and therefore new dislocation dipoles are generated in the material to accommodate the imposed deformation. Therefore it is to be expected that the dislocation density in the presence of obstacles is much larger than in obstacle-free crystals. Figure 6.6 shows the dislocations present in the crystals without (a) and with obstacles (b) at final indentation depth. The dislocations are colored based on the slip system they belong to, nevertheless it is difficult to distinguish specific dislocation patterns that indicate whether obstacles favor specific lattice misorientations. To further investigate what is the link between obstacles, dislocation density and lattice orientation we will attempt in the following section an analysis of the geometrically necessary dislocations generated in the presence and absence of obstacles.

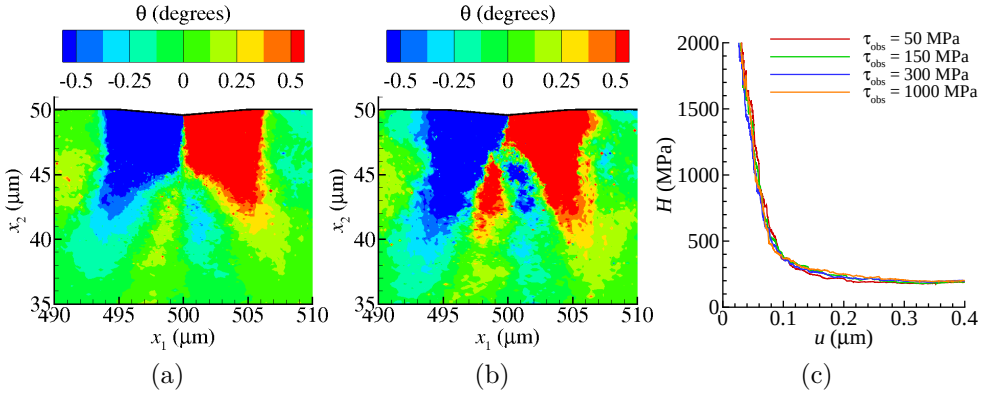

Figure 6.5. The distribution of lattice rotation for (a) $\tau_{\text{obs}} = 50$ MPa and (b) $\tau_{\text{obs}} = 1000$ MPa. (c) The hardness for different obstacle strength. The source density is $\rho_{\text{nuc}} = 144\ \mu\text{m}^{-2}$ and the obstacle density is $\rho_{\text{obs}} = 100\ \mu\text{m}^{-2}$.

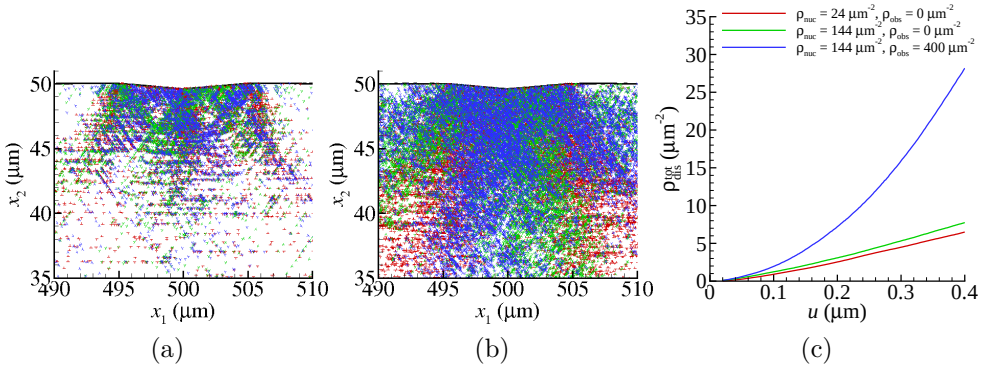

Figure 6.6. The distribution of dislocations for (a) $\rho_{\text{obs}} = 0\ \mu\text{m}^{-2}$, (b) $\rho_{\text{obs}} = 400\ \mu\text{m}^{-2}$. (c) The evolution of total dislocation density in the plastic region for different source and obstacle density.

6.5.1 Obstacles and dislocation structure

It is not possible to determine which of the dislocations that have produced the lattice rotation in the crystals are geometrically necessary and which ones are statistically stored. Yet, it is possible to calculate the lower bound of the

GNDs on each slip system, by making use of their relationship with Nye's dislocation density tensor, α_{ij} (Kysar et al., 2007, 2010). For infinitesimal lattice rotations Nye's tensor is defined as follows,

$$\alpha_{ji} = -\kappa_{ij} + \delta_{ij}\kappa_{kk} + e_{ipk}\epsilon^{el}_{jk,p} \tag{6.10}$$

where κ_{ij} is the non-symmetric crystal lattice curvature tensor and ϵ^{el}_{jk} is the elastic strain of the crystal lattice. The lattice curvature tensor is defined as $\kappa_{ij} = \partial\theta_i/\partial x_j$, where θ_i represent the rotation with respect to the three coordinate axes. This equation can be simplified for this problem to $\alpha_{ij} = -\kappa_{ji}$, by virtue of the following considerations: (1) for a plane strain problem rotations can only occur with respect to the in-plane axis, so that θ_3 is the only non-zero component; (2) the gradient of elastic strain is expected to be negligible if compared to the lattice rotation (Drugan and Rice, 1984). This means that lattice rotation we calculated previously is the only quantity necessary to determine Nye's dislocation density tensor (Nye, 1953). The density of GND is related to α_{ij} as follows:

$$\alpha_{ij} = \sum_{\alpha=1}^{3} \rho^{(\alpha)}_{\mathrm{GND}} b^{(\alpha)} s^{(\alpha)}_i t^{(\alpha)}_j, \tag{6.11}$$

where $b^{(\alpha)}$ is the magnitude of Burgers vector on the αth slip plane, $\mathbf{s}^{(\alpha)}$ and $\mathbf{t}^{(\alpha)}$ are the unit vectors along and normal to the αth slip plane.

For the specific crystal orientation used in this study equating the Nye's tensor to the density of GNDs leads to the following two equations with three unknowns:

$$\begin{bmatrix} \alpha'_{13} \\ \alpha'_{23} \end{bmatrix} = \begin{bmatrix} \frac{\sqrt{3}}{4} & \frac{\sqrt{3}}{3} & -\frac{\sqrt{3}}{4} \\ \frac{\sqrt{6}}{4} & 0 & \frac{\sqrt{6}}{4} \end{bmatrix} \begin{bmatrix} \rho^{(1)}_{\mathrm{GND}} b^{(1)} \\ \rho^{(2)}_{\mathrm{GND}} b^{(2)} \\ \rho^{(3)}_{\mathrm{GND}} b^{(3)} \end{bmatrix} \tag{6.12}$$

The GND densities are governed by the under-determined equations in 6.12. Following Arsenlis and Parks (Arsenlis and Parks, 1999) we find a lower bound for the density of GNDs, that is not only unique, but that can be apportioned uniquely on the slip systems as demonstrated by Kysar (Kysar et al., 2010).

The total GND density and the density of GNDs apportioned on the different slip systems are presented in Fig. 6.7. In the presence of obstacles the density of GNDs is clearly much larger. It is interesting to see that the distribution of GNDs on the slip planes oriented at $\varphi = 0^\circ$ is qualitatively different in the crystals with and without obstacles. For obstacle-free crystals the central region of the plastic zone contains a large density of negative GNDs, while

the positive ones are confined to the edges of the plastic zone. In the presence of obstacles negative GNDs form a V-shape that originates from the contact. Thus from Fig. 6.7 it appears that the presence of obstacles, besides an in-

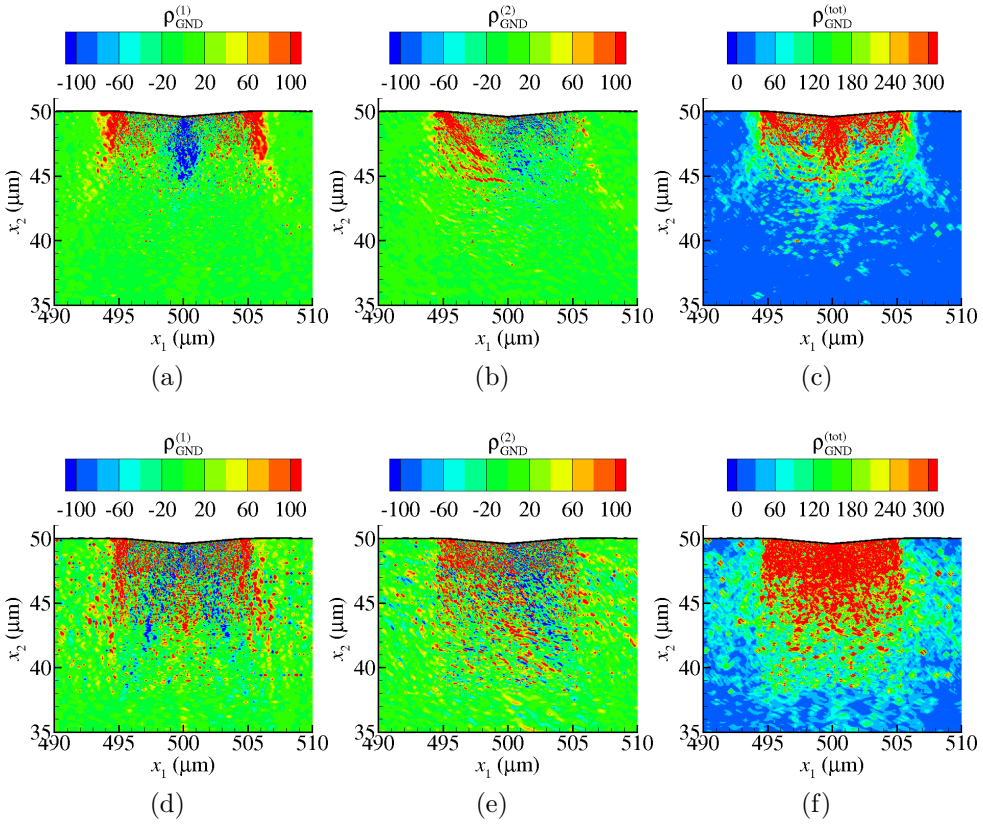

Figure 6.7. The distribution of GNDs for an obstacle-free crystal and for a crystal with a density of obstacles $\rho_{\text{obs}} = 0\ \mu\text{m}^{-2}$ and $\rho_{\text{obs}} = 400\ \mu\text{m}^{-2}$ on slip system 1 (a)(d), 2 (b)(e) and on all slip systems (c)(f) .

crease in dislocation density, also gives rise to a different distribution of GNDs. This is particularly evident if one contrasts Fig. 6.7(a) and (d). Indeed, if only the dislocations on the horizontal slip planes are plotted for crystals with and without obstacles, see Fig. 6.8, it is evident that not only the density but also the spatial distribution of the dislocations is influenced by the presence of obstacles. To further investigate the role of obstacles on lattice rotation, we

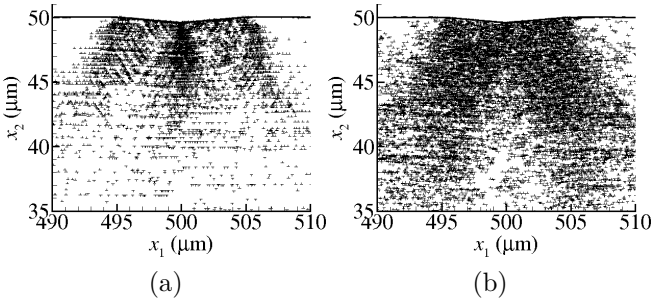

Figure 6.8. The distribution of dislocations on 0°-slip planes for (a) $\rho_{\text{obs}} = 0\ \mu\text{m}^{-2}$ and (b) $\rho_{\text{obs}} = 400\ \mu\text{m}^{-2}$.

perform a simulation for a crystal that contains dislocation obstacles only on the horizontal slip planes. As expected the lattice rotation obtained at final indentation depth, see Fig. 6.9, does present the two misorientation regions, that are typical of CP simulations. The dislocation density generated dur-

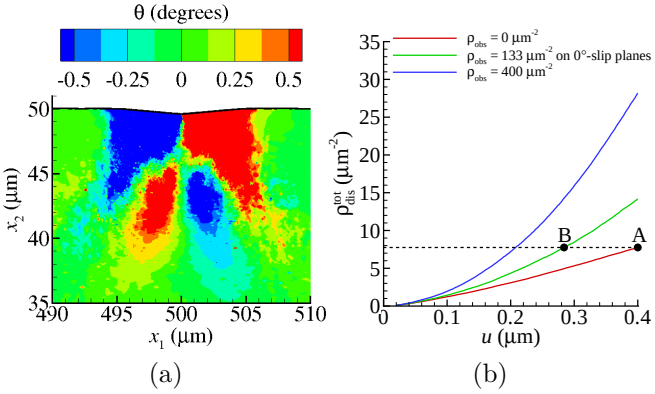

Figure 6.9. (a) The distribution of elastic lattice rotation for $\rho_{\text{obs}} = 133\ \mu\text{m}^{-2}$, only distributed on 0°-slip planes. (b) The evolution of total dislocation density in the plastic region for different obstacle distributions.

ing indentation of this crystal is intermediate between the density obtained during indentation of a crystal with obstacles on all slip planes and a crystal

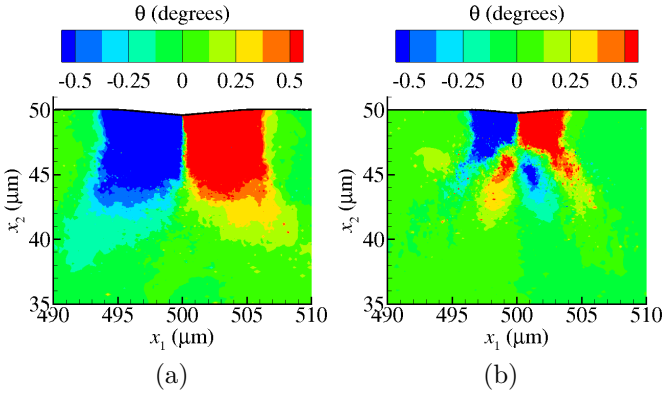

Figure 6.10. The distribution of lattice rotation for (a) $\rho_{\text{obs}} = 0\ \mu\text{m}^{-2}$, at $u = 0.4\ \mu$m and for (b) $\rho_{\text{obs}} = 133\ \mu\text{m}^{-2}$ only on 0°-slip planes, at $u = 0.284\ \mu$m. The total dislocation density in the plastic region is $\rho_{\text{dis}}^{\text{tot}} = 7.75\ \mu\text{m}^{-2}$.

without obstacles, as can be seen in Fig. 6.9. Nevertheless, demonstration that a higher dislocation density is not the reason for which the lattice rotation obtained with obstacles agrees with CP simulations is given in Fig. 6.10. Here the lattice rotation obtained in the two crystals is compared at the same dislocation density $\rho_{\text{dis}}^{\text{tot}} = 7.75\ \mu\text{m}^{-2}$. The dislocation density is the same but the misorientations appear only in the presence of obstacles.

6.5.2 Crystal orientation

To investigate whether the strong obstacle dependence on lattice rotation is only a specific feature of an FCC crystal having a set of slip planes exactly normal to the indentation direction or if it is a more general feature, we repeat the simulations after rotating the crystal by 10°. Figure 6.11 shows the distribution of lattice rotation obtained by CP simulations (a) and by DDP simulations in the absence (b) and in the presence of obstacles (c). Similarly to the case of the unrotated crystal, the lattice rotation obtained by CP simulations is in qualitative agreement only with the DDP simulations with obstacles. Even if the crystal is rotated by 90°, see Fig. 6.12, the lattice misorientation obtained by CP can only be achieved by DDP in the presence of obstacles. We conclude thus that obstacles influence the lattice misorientation strongly, independently of crystal orientation.

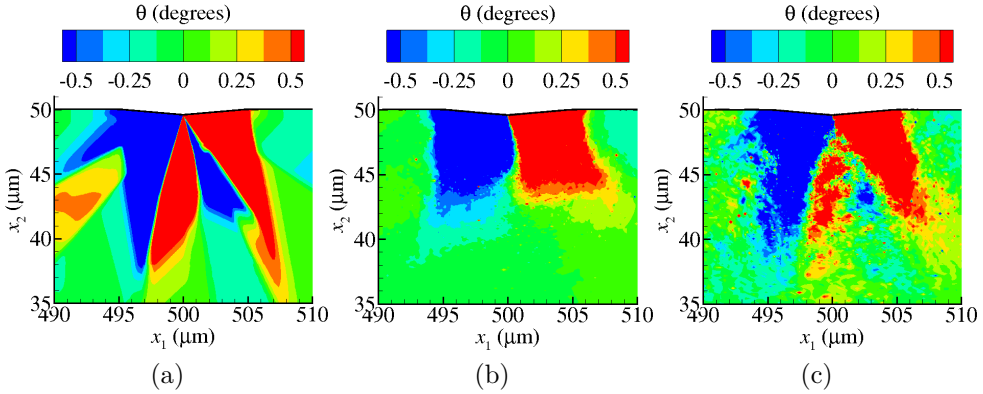

Figure 6.11. The distribution of lattice rotation for slip systems at 10°, 64.7° and −44.7° by (a) CP and DDP with obstacle density (b) $\rho_{\text{obs}} = 0\ \mu\text{m}^{-2}$ and (c) $\rho_{\text{obs}} = 400\ \mu\text{m}^{-2}$.

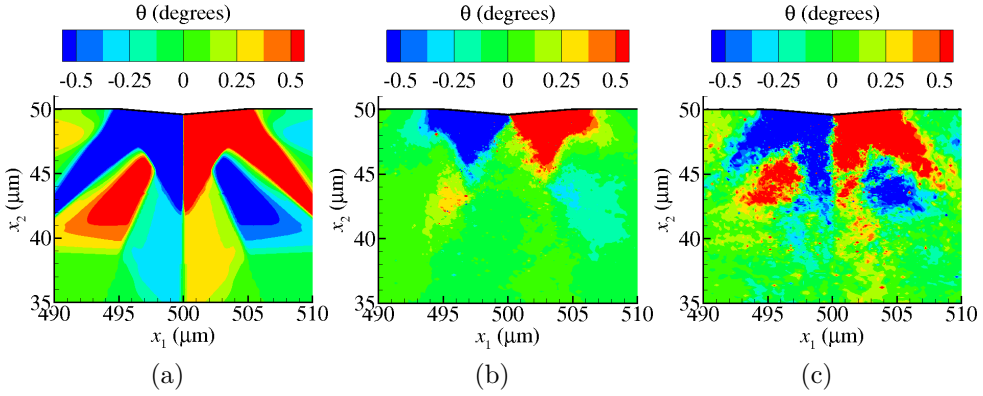

Figure 6.12. The distribution of lattice rotation for slip planes at 90° and ±35.3° by (a) CP and DDP with obstacle density (b) $\rho_{\text{obs}} = 0\ \mu\text{m}^{-2}$ and (c) $\rho_{\text{obs}} = 400\ \mu\text{m}^{-2}$.

6.6 Dislocation arrangements from similarity contact analysis

The dislocation arrangements that can be expected during wedge indentation, can be deduced from the similarity contact analysis by Bower et al. (Bower

et al., 1993), who pointed out that for arbitrary contacts, the strain rates and stresses at any particular instant in a pure creeping solid are independent of the loading history and only depend on the instantaneous velocities and contact radius prescribed on the surface. Consequently, in any load interval δP, for which the contact size increases from a to δa, the strain increments and stress fields are identical to those under a rigid flat-ended punch under a load δP as shown in Fig. 6.13(a). The crystal plasticity solution for a flat-ended punch is just opposite to the solution of a Mode-I crack by Rice (Rice, 1987). As shown in Fig. 6.13(a), this includes two inclined slip bands at $\pm 54.7^\circ$ and a vertical kink band that corresponds to the 0°-slip plane. Only elastic deformation occurs between these arrays of dislocations. As shown in Fig. 6.13(b), using the similarity contact analysis, the dislocation arrangements under our wedge contact will result from a cumulative superposition of the basic solution in Fig. 6.13(a).

In Fig. 6.14 the lattice rotation changes and the dislocation sign changes for the DDP simulations are shown along a horizontal path that crosses the four sectors. Corresponding to the four sectors formation, the dislocation density changes sign as a rotation sector boundary is crossed over. That is, moving in x1 direction, a change from negative (positive) to positive (negative) rotation corresponds to a negative (positive) average Burgers vector density as shown in Fig. 6.14(c).

The dislocation sign change suggests that sectors similar to those in Fig. 6.14(a) could be obtained by dislocation arrays of the type shown in Fig. 6.15.

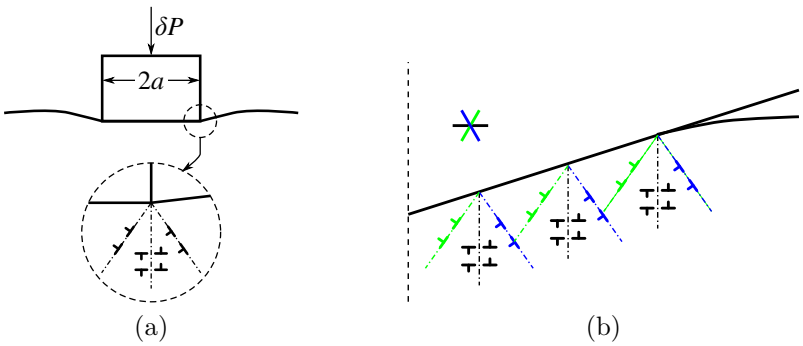

Figure 6.13. (a) Schematics showing a flat-ended punch and the dislocation arrangements caused in crystal by the edge of the punch, which is exactly opposite to the Mode-I crack solution by Rice (Rice, 1987). (b) The dislocation arrangements under the wedge contact result from the cumulative superposition of solutions in (a).

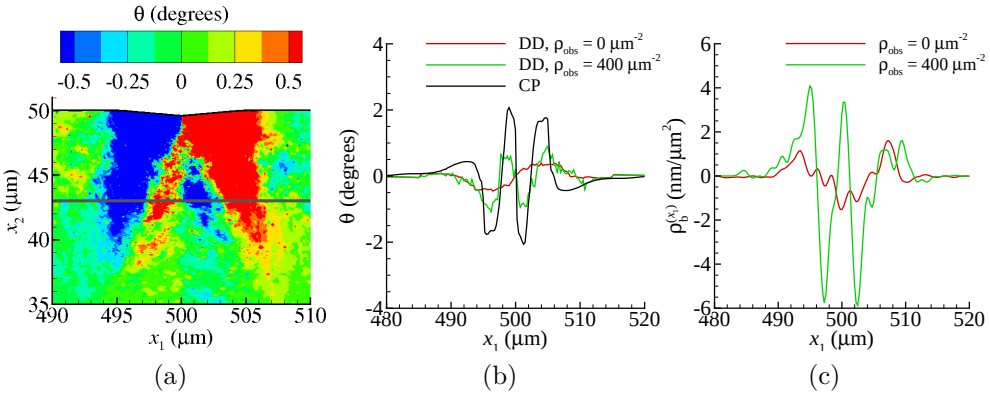

Figure 6.14. (a)The path chosen to measure the dislocation sign and lattice rotation $x_2 = 43$ μm. (b) The average lattice rotation and (c) the projection in x_1-direction of the average Burgers vector.

Referring back to Fig. 6.13 which shows the right half of the contact, dislocations on the 54.7° slip plane (green) will move towards the contact center and those on the −54.7° slip plane (blue) will move away from the contact center. Similar scenario occurs in the left half of the contact, thus leading to the schematics in Fig. 6.15 (middle column). Dislocation interactions cannot be intuitively derived from Fig. 6.13(b), but results in Figs. 6.6(a) and (b) show that the dislocations on these two symmetric slip planes are qualitatively similar to the schematic drawings in Fig. 6.15. Dislocation arrangements on the ±54.7° are not much affected by the presence of dislocation obstacles, while dislocations on the 0°-slip plane are very sensitive to the obstacles. The dislocation dipoles in Fig. 6.13(b) are not expected to separate much if strong obstacles are present. Therefore, in this right half of the contact, the dislocations with negative Burgers vector will accumulate near (but still at some distance away from) the contact center, while the ones with positive Burgers vector will lie outside of the contact zone. Such an argument will lead to the schematic drawing in Fig. 6.15 (lower left figure), which is qualitatively similar to Fig. 6.4. The total effects of these dislocation arrangements in the lower row of Fig. 6.15 will lead to the formation of four rotation sectors. The above model can also explain the absence of four sectors when the dislocation obstacles are turned off. In such a case, the dislocation dipoles on the horizontal slip planes will be easily separated. Referring to the simulations in Fig. 10(a), we find that the dislocations with negative Burgers vector will be located right underneath the indenter, while the opposite ones will be at the two sides. This

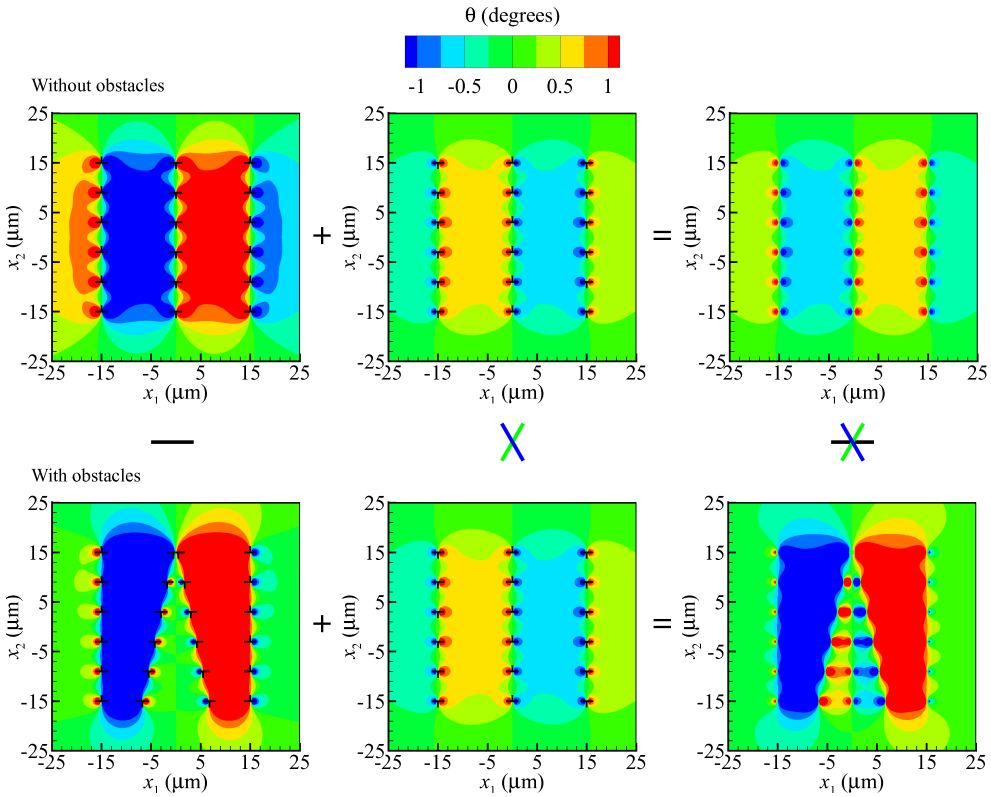

Figure 6.15. Lattice rotation fields obtained by simple arrangements of dislocation arrays that give similar features to the DD simulations: the first column represent the lattice rotation caused by the dislocations on the 0°-slip plane, the second column the lattice rotation caused by the dislocations on the ±54.7°-slip planes and the third column is a sum of the first two contributions.

leads to the schematic illustration in the upper left of Fig. 6.15. However, the absence of obstacles only changes the dislocation density on the inclined slip planes, but not their arrangements. Consequently, the resulting dislocation arrangements in the upper row in Fig. 6.15 will lead to the formation of two rotation sectors.

Therefore it may be concluded that the lattice rotation patterns are primarily governed by the slip systems when the dislocation obstacle density and strength are both high, which agree with continuum crystal plasticity that predicts the four rotation sectors. When the density and strength of obstacles

are low, the dislocation dipoles on the kink bands will lead to a different microstructural feature. In both cases the microstructure is uncorrelated to the indentation size effects.

6.7 Conclusions

The lattice misorientations caused in a single crystal by wedge indentation were studied by crystal plasticity and discrete dislocation plasticity simulations. The results were contrasted at the indentation depth of $u = 0.4$ μm for a source density in the DDP simulations of 144 μm^{-2}, such that the hardness calculated by the two numerical techniques was similar.

- In DDP simulations lattice rotation is majorly influenced by the presence in the crystal of obstacles to dislocation motion: when obstacles are present the discrete lattice misorientations are in good agreement with the continuum lattice rotation calculated by crystal plasticity simulations; when obstacles are absent the misorientation sectors typical of CP simulations fail to form. The effect of obstacles is twofold: it increases the dislocation density but more importantly it gives rise to different dislocations structures, and a different distribution of GNDs. It is here demonstrated that the increased dislocation density is not the reason for a better agreement between CP and DDP results.

- The lattice mismatch obtained by DDP simulations when a distribution of obstacles is present in the crystal resembles the results of crystal plasticity simulations. The localized differences and the fact that the lattice distribution obtained by DDP simulations present less defined sectors are caused by the discreteness intrinsic to the DDP method.

- In DDP simulations lattice orientation is only marginally affected by dislocation source density.

- On the contrary, the indentation size effect depends largely on source density and only minorly on obstacle density.

- The dependence of lattice rotation on obstacle density is not specific of an indentation direction but affects all the crystal orientations tested in this study.

- Based on the solution of deformation fields near a stationary crack (which is equivalent to, but in opposite sign, a flat punch contact) and similarity

properties of indentation fields, we have developed a simple model that explains the dislocation pattern evolution and its relationship to the observed lattice misorientation fields.

Acknowledgments

L.N. is grateful to the Dutch National Scientific Foundation NWO and Dutch Technology Foundation STW for their financial support (VENI Grant 08120). Y.G. acknowledges the support of the U.S. Department of Energy, Basic Energy Sciences, Materials Sciences and Engineering Division.

References

Arsenlis, A., Parks, D.M., 1999. Crystallographic aspects of geometrically-necessary and statistically-stored dislocation density. Acta Mater. 47, 1597–1611.

Balint, D.S., Deshpande, V.S., Needleman, A., Van der Giessen, E., 2006. Discrete dislocation plasticity analysis of the wedge indentation of films. J. Mech. Phys. Solids 54, 2281–2303.

Barabash, R.I., Bei, H., Gao, Y.F., Ice, G.E., 2010a. Indentation-induced localized deformation and elastic strain partitioning in composites at submicron length scale. Acta Mater. 58, 6784–6789.

Barabash, R.I., Bei, H., Gao, Y.F., Ice, G.E., George, E.P., 2010b. 3D X–ray microprobe investigation of local dislocation densities and elastic strain gradients in a NiAl-Mo composite and exposed Mo micropillars as a function of prestrain. J. Mater. Res. 25, 199–206.

Bouvier, S., Needleman, A., 2006. Effect of the number and orientation of active slip systems on plane strain single crystal indentation. Modelling Simul. Mater. Sci. Eng. 14, 1105–1125.

Bower, A.F., Fleck, N.A., Needleman, A., Ogbonna, N., 1993. Indentation of a power law creeping solid. Proc. R. Soc. Lond. A 441, 97–124.

Drugan, W.J., Rice, J.R., 1984. Restrictioins on quasi-statically moving surfaces of strong discontinuity in elastic-plastic solids. Mechanics of Material Behavior: The D.C. Drucker Anniversary Volume .

Fleck, N.A., Muller, G.M., Ashby, M.F., Hutchinson, J.W., 1994. Strain gradient plasticity: theory and experiments. Acta Metall. Mater. 42, 475–487.

Gudmundson, P., 2004. A unified treatment of strain gradient plasticity. J. Mech. Phys. Solids 52, 1379–1406.

Gurtin, M.E., 2002. A gradient theory of single-crystal viscoplasticity that accounts for geometrically necessary dislocations. J. Mech. Phys. Solids 50.

Kysar, J.W., Gan, Y.X., L., M.T., Chen, X., Jones, M.E., 2007. High strain gradient plasticity associated with wedge indentation into face-centered cubic single crystals: geometrically necessary dislocation densities. J. Mech. Phys. Solids 55, 1554–1573.

Kysar, J.W., Saito, Y., Oztop, M.S., Lee, D., Huh, W.T., 2010. Experimental lower bounds on geometrically necessary dislocation density. Int. J. Plast. 26, 1097–1123.

Larson, B.C., El-Azab, A., Yang, W., Tischler, J.Z., Liu, W., Ice, G.E., 2007. Experimental characterization of the mesoscale dislocation density tensor. Phil. Mag. 87, 1327–1347.

Nix, W.D., Gao, H., 1998. Indentation size effects in crystalline materials: a law for strain gradient plasticity. J. Mech. Phys. Solids 46, 411–425.

Nye, J.F., 1953. Some geometrical relations in dislocated crystals. Acta Metall. 1, 153–162.

Peirce, D., Asaro, R.J., Needleman, A., 1983. Material rate dependence and localized deformation in crystalline solids. Acta Metall. 31, 1951–1976.

Pharr, G.M., G., H.E., F., G.Y., 2010. The indentation size effect: a critical examination of experimental observations and mechanistic interpretations. Annu. Rev. Mater. Res. 40, 271–292.

Rice, J.R., 1987. Tensile crack tip fields in elastic-ideally plastic crystals. Mech. Mater. 6, 317–335.

Saito, Y., Kysar, J.W., 2011. Wedge indentation into elastic–plastic single crystals, 1: Asymptotic fields for nearly-flat wedge. Int. J. Plast. 27, 1640–1657.

Saito, Y., Oztop, M.S., Kysar, J.W., 2012. Wedge indentation into elastic-plastic single crystals, 2: simulations for face-centered cubic crystals. Int. J. Plast. 28, 70–87.

Van der Giessen, E., Needleman, A., 1995. Discrete dislocation plasticity: a simple planar model. Modelling Simul. Mater. Sci. Eng. 3, 689–735.

Yang, W., Larson, B.C., Pharr, G.M., Ice, G.E., Budai, J.D., Tischler, J.Z., Liu, W., 2004. Deformation microstructure under microindents in single-crystal cu using three-dimensional x-ray structural microscopy. J. Mater. Res. 19, 66–72.

Chapter 7

Discrete dislocation simulations of the flattening of nanoimprinted surfaces

Abstract

Simulations of rough surface flattening are performed on thin metal films whose roughness is created by nanoimprinting flat single crystals. The imprinting is carried out by means of a rigid template with equal flat contacts at varying spacing. The imprinted surfaces are subsequently flattened by a rigid platen, while the change of roughness and surface profile is computed. Attention is mainly focused on comparing the response of the film surfaces with those of identical films cleared of the dislocations and residual stresses left by the imprinting process. The aim of these studies is to understand to which extent the loading history affects deformation and roughness during flattening. The limiting cases of sticking and frictionless contact between rough surface and platen are analyzed. Results show that when the asperities are flattened such that the contact area is up to about one third of the surface area, the loading history strongly affects the flattening. Specifically, the presence of initial dislocations facilitates the squeezing of asperities independently of the friction conditions of the contact. For larger contact areas, the initial conditions affect only sticking contacts, while frictionless contacts lead to a homogeneous flattening of the asperities due to yield of the metal film. In all cases studied the final surface profile obtained after flattening has little to no resemblance to the original imprinted surface.

7.1 Introduction

Surface roughness plays a crucial role during metal forming processes, since it controls the friction properties until the moment that possibly all asperities are flattened. Deformation of the asperities depends on their distribution, height and on their plastic response.

Models of rough surface contact have shown that surfaces cannot be just treated as a collection of single asperities and that the choice of the description of surface roughness is critical. So far rough surfaces have been mainly described either as statistical (Greenwood and Williamson, 1966; Jackson and Green, 2006) or fractal (Ciavarella et al., 2006; Gao and Bower, 2006; Majumdar and Bhushan, 1991; Yan and Komvopoulos, 1998), but recent models,

This chapter is published as:
Y. Zhang, E. Van der Giessen and L. Nicola, Discrete dislocation simulations of the flattening of nanoimprinted surfaces, Model. Simul. Mater. Sc. 18 (2010) 034006

e.g. (Wilson et al., 2009) derive their rough surface profile description directly from experimentally measured surfaces.

The evaluation of rough surface profiles has been made possible in the past years by a variety of new experimental techniques, including atomic force microscopy, phase shifting interferometry and laser confocal scanning microscopy. Meanwhile, significant numerical effort has been devoted to artificially reproduce two or three-dimensional rough surfaces that have realistic characteristics, e.g. (Bakolas, 2003; Patir, 1978; Wu, 2000).

But how relevant is the precise topography of the surface in the prediction of rough surface evolution under contact loading? To which extent would current models profit by such an accurate description?

The aim of this paper is to investigate, by numerical simulations, whether the plastic behavior of a surface is uniquely determined by its profile or if it is affected by the loading history that has created the profile. To this end, numerical simulations are performed in which first surface roughness is created by nanoimprinting, and subsequently the rough surface is flattened by contact with a rigid platen.

The numerical procedure follows the discrete dislocation plasticity method by Van der Giessen and Needleman (Van der Giessen and Needleman, 1995), that allows for a size dependent treatment of plastic deformation of (sub)micron scale asperities, through the computation of the collective motion of discrete dislocations. In order to create a rough surface, single crystal metal thin films are imprinted by an array of equally spaced rigid indenters. Surfaces with different roughness are obtained by changing the template profile, specifically the spacing between indenters. The rough surfaces thus obtained are then flattened by a rigid platen, and the results are compared to those for films with the same surface profile but cleared from the loading history, i.e. dislocation- and stress-free at the beginning of compression. In principle, this could be achieved experimentally by a heat treatment. The presence of an initial dislocation structure may either facilitate or obstruct the flattening of the surface. Our results reveal that the presence of dislocations in the subsurface region significantly influences the subsequent deformation process.

7.2 Imprinting

7.2.1 Model

The metal to be imprinted is idealized as an infinitely long single crystal, which is constrained to deform in plane strain perpendicular to the x_1–x_2 plane (see Fig. 7.1). The crystal is assumed to be in the form of a thin film, with thickness

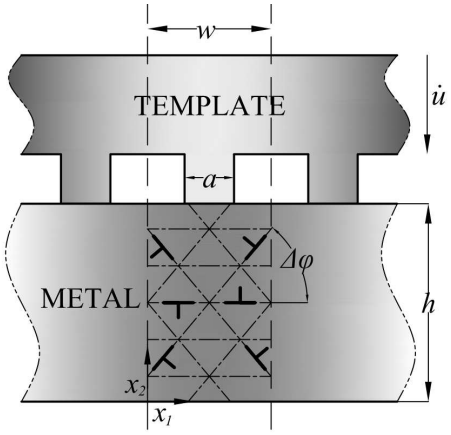

Figure 7.1. Two-dimensional model of a metal single crystal imprinted by a rigid template with a rectangular wave profile. The width of the contacts is a and the center-to-center contact spacing is w. Calculations are carried out for a unit cell of width w, unless otherwise specified.

h so that the elastic displacement during indentation is small compared with what it would be in a bulky metal specimen; this allows for larger retained imprints at the same indentation depth. The film is elastically isotropic, with Young's modulus E and Poisson's ratio ν. Plastic flow occurs in the crystal as a result of the nucleation and motion of edge dislocations that glide along three sets of slip systems as indicated in Fig. 7.1. The Burgers vector of the dislocations has magnitude b, and direction parallel to the slip plane. The line direction of the dislocations is perpendicular to the plane of deformation, consistently with the assumption of plane strain.

The film is imprinted by an infinitely long rigid template with a rectangular wave profile. Each flat contact has length a and the center-to-center spacing between contacts is w. Dislocations are assumed to nucleate from Frank-Read sources in the metal; surface nucleation from dislocation steps is not accounted for. The distribution of dislocation sources and obstacles is taken to be periodic in the x_1–direction with period w and the calculations are carried out for a unit cell that lies between $0 < x_1 < w$. The metal is taken to have the elastic properties of aluminum: Young's modulus $E = 70$ GPa and a Poisson's ratio $\nu = 0.33$. There are three potentially active slip systems in the 2D crystal (Nicola et al., 2004; Rice, 1987), with discrete slip planes oriented at $\varphi = 0°$, $60°$ and $120°$ (see Fig. 7.1), and spaced at $173b$. The magnitude of the Burgers vector is taken to be $b = 0.25$ nm. Initially, the

crystal is dislocation free. However, it contains a density $\rho = 30\ /\mu\text{m}^2$ of obstacles and of dislocation sources distributed randomly on the slip planes in the crystal. The mean nucleation strength is given as $\bar{\tau}_{\text{nuc}} = 50$ MPa with a standard deviation of 10 MPa for a Gaussian distribution, and the time t_{nuc} for nucleation is taken to be 0.1 ns.

Nucleation from point sources occurs when the resolved shear stress on the source exceeds its critical strength, τ_{nuc} for a given time span t_{nuc}. After nucleation, the glide velocity v^I of the Ith dislocation is proportional to the Peach-Koehler force f^I according to

$$f^I = Bv^I \tag{7.1}$$

with B the drag coefficient. Two nearby dislocations with opposite Burgers vector are taken to annihilate when they are within a distance L_{ann}. Obstacles to dislocation motion are modeled as points on the slip planes and stop dislocations that attempt to pass through them. An obstacle releases a pinned dislocation when the Peach-Koehler force on the dislocation exceeds $\tau_{\text{obs}}b$, where the obstacle strength is here taken to be $\tau_{\text{obs}} = 150$ MPa.

Boundary conditions

The loading is imposed by prescribing normal displacement under the contacts

$$u_2(x_1, h) = -\int \dot{u}\mathrm{d}t, \qquad \frac{w}{2} - \frac{a}{2} \le x_1 \le \frac{w}{2} + \frac{a}{2}\,. \tag{7.2}$$

We assume that the contact between metal and indenters be perfectly sticking. Thus, the lateral displacement on the contact surface satisfies

$$u_1(x_1, h) = 0, \qquad \frac{w}{2} - \frac{a}{2} \le x_1 \le \frac{w}{2} + \frac{a}{2}\,. \tag{7.3}$$

The traction distribution along the contact determines the imprinting force F (per unit of length):

$$F := -\int_{w/2-a/2}^{w/2+a/2} \sigma_{22} dx_1\,.$$

Outside the contact region, the top surface ($x_2 = h$) is traction free, which requires

$$\sigma_{12}(x_1, h) = \sigma_{22}(x_1, h) = 0, \qquad 0 < x_1 < \frac{w}{2} - \frac{a}{2} \text{ and } \frac{w}{2} + \frac{a}{2} < x_1 < w\,. \tag{7.4}$$

The boundary conditions along the bottom of the unit cell, $x_2 = 0$, are taken to be

$$u_2(x_1, 0) = 0 \quad \sigma_{12}(x_1, 0) = 0. \tag{7.5}$$

Periodic boundary conditions are imposed on the sides of the simulation cell by requiring

$$u_1(0, x_2) = u_1(w, x_2) = 0 \qquad u_2(0, x_2) = u_2(w, x_2) \,, \tag{7.6}$$

thereby incorporating the lateral constraint imposed by the rigid, sticking indenters.

Even though the computations assume small strains, the contact between the rigid template and the film is based on the deformed film surface. The calculation is performed incrementally. At each time step, the stress and deformation state is determined using superposition of a singular field and an image field solution, (Van der Giessen and Needleman, 1995). The singular field is associated with the discrete dislocations and is calculated analytically. The image field is obtained from the finite element solution of the associated non-singular linear elastic boundary value problem. Once the stresses have been determined, the incremental change in position of each dislocation is calculated, and conditions are checked for nucleation, annihilation of dipoles, and pinning at or release from obstacles. Details on the numerical procedure for solving the governing field equations and constitutive equations are presented in (Nicola et al., 2008).

7.2.2 Imprinting Simulations

Thin films are imprinted by rigid templates with different spacing between indenters in order to obtain surfaces with various roughness. Simulations are performed for contacts whose center-to-center spacing w ranges from 1 to 10 μm. The contact width of each indenter is $a = 0.1$ μm and the film height is $h = 2$ μm. The films are imprinted to a maximum depth of $u_{\max} = 0.05$ μm with an indentation speed of $\dot{u} = 4 \times 10^4$ μm/s. The films are then unloaded at the same speed and subsequently allowed to relax.

The imprinting force for various w is plotted in Fig. 7.2a. When the template contacts are closely spaced (small w) a larger force is required to imprint the films. This is partly due to the different elastic stress state developing during loading, but mainly to a different plastic behavior: the plastic zones underneath closely spaced contacts interact with each other and give rise to a harder response (see also (Nicola et al., 2007, 2008)). Figure 7.3a, b, c shows the stress σ_{22} and dislocation distribution in the unit cells for $w = 2$, 5 and 10 μm at the maximum imprinting depth ($u = 0.05$ μm). The dislocations mainly distribute underneath the indenter in the central region of the unit cell. The plastic region is isolated from neighboring contacts in the film with largest spacing between indenters, but when contacts are close to each other like in

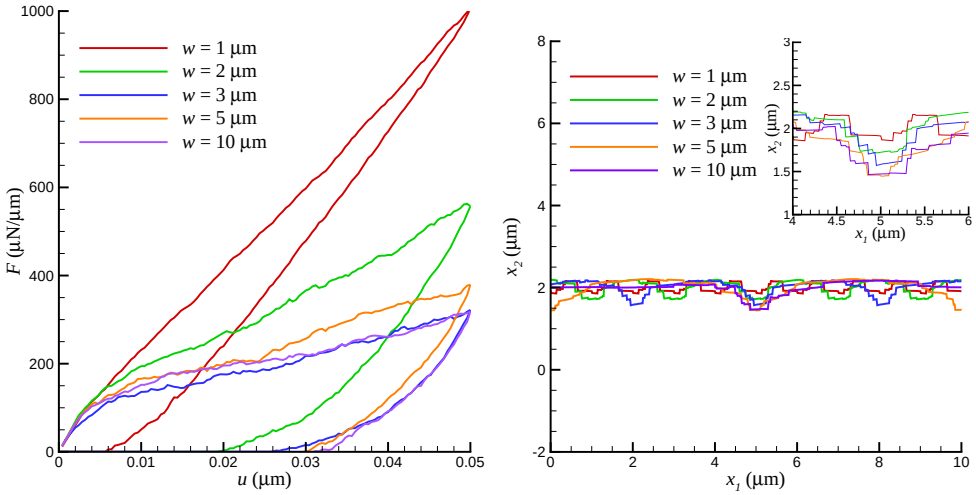

Figure 7.2. (a) Force response during imprinting with contacts of $a = 0.1$ μm for values of the spacing w from 1 μm to 10 μm. (b) Profile of the top surface after unloading and relaxation for the various templates (i.e. different spacing between indenters). The maximum imprinting depth is $u_{\max} = 0.05$ μm. The vertical displacements of the top surface are magnified by a factor 20 for ease of visualization.

the case $w = 1$ μm the plastic zones interact and cause a harder response (see Fig. 7.2a). For the simulations just shown the center-to-center contact spacing w corresponds to the unit cell width. It is reasonable to suspect that the different plastic response for different w could be attributed to the different size in the unit cell and therefore related to the boundary conditions imposed on the unit cell. To investigate this issue we perform a simulation in which the center-to-center contact spacing is $w = 2$ μm and the unit cell width is $5w = 10$ μm, therefore comprising five contacts. A larger unit cell with more contacts has the additional advantage that statistical effects, related to the sampled source distribution, are reduced. The stress state for this simulation is presented in Fig. 7.3d. A comparison between Fig. 7.3a, d and c shows that there is no artifact due to boundary conditions in case (a) and confirms that hardening in case (a) and (d) is indeed caused by interactions between plastic zones.

In the loaded state, the surface profile seen in Fig. 7.3 clearly exhibits imprints that are significantly wider than the contact size $a = 0.1$ μm. Also,

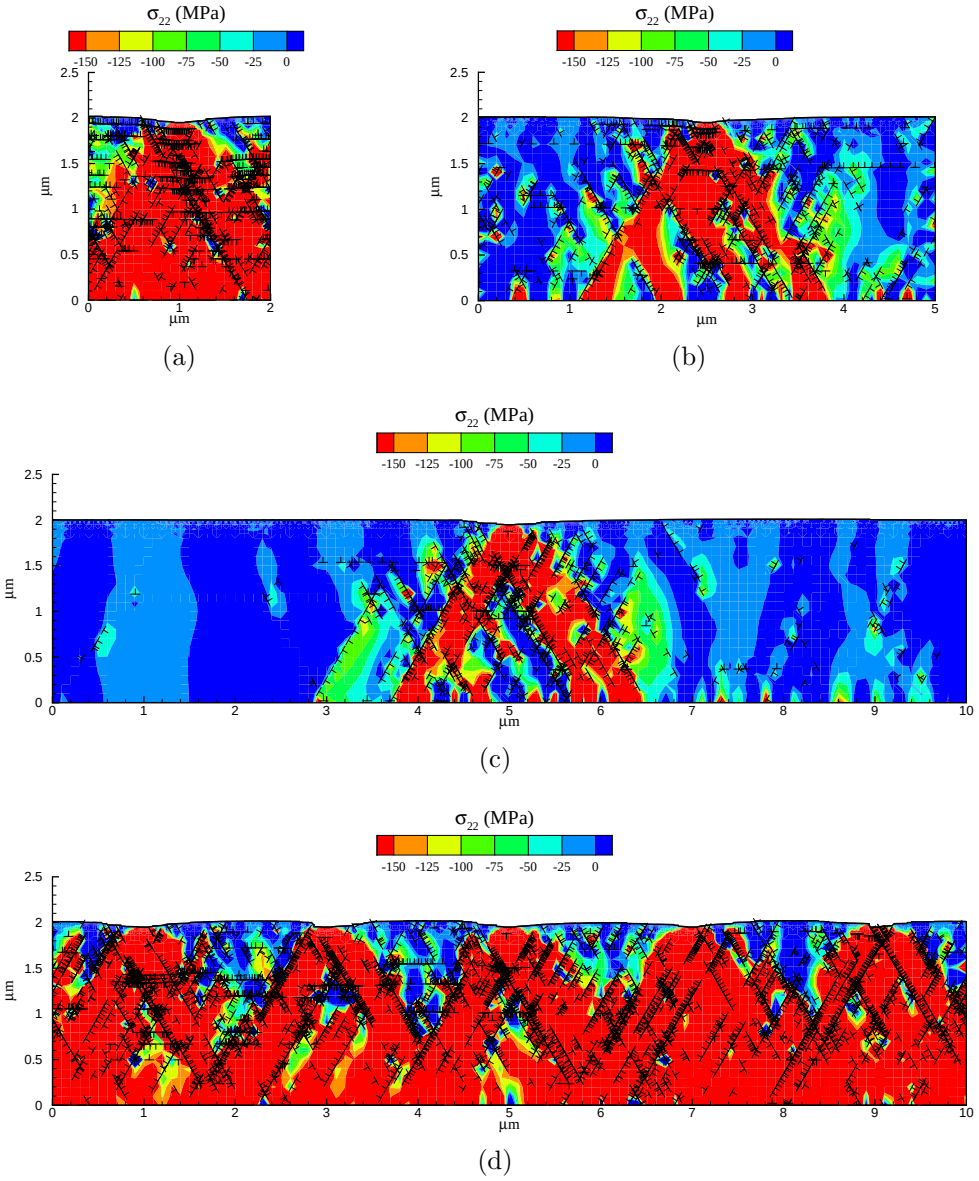

Figure 7.3. The stress distribution at the maximum imprinting depth $u = 0.05$ μm for (a) $a/w = 0.1/2$, (b) $a/w = 0.1/5$, and (c) $a/w = 0.1/10$ and (d) $5 \times a/5w = 5 \times 0.1/10$.

there is some finer roughness that has accumulated from the slip steps created when dislocations left the material through the free surface. Upon unloading,

the induced dislocation structure dissolves partially but even after relaxation a dislocation structure remains. The final roughness of the surface, comprising the remanent imprints and nearby material pile-ups, is shown in Fig. 7.2b, where the vertical displacements are magnified by a factor 20 for ease of visualization. We choose to describe the roughness of the obtained surface profiles by mean of the root-mean-square surface roughness R_{m}, defined as

$$R_{\mathrm{m}} = \sqrt{\frac{1}{N}\sum_{i=1}^{N}(h_i - h_{\mathrm{m}})^2}, \tag{7.7}$$

where N is the total number of top surface nodes, h_i is the vertical coordinate of node i and h_{m} is the mean surface height; and the height-height correlation function $H_{\mathrm{r}}(r)$, defined as

$$H_{\mathrm{r}}(r) = \frac{1}{N}\sum_{i=1}^{N}\left[(h(x_1(i)+r) - h_i)^2\right], \tag{7.8}$$

where $0 < r < w$; $x_1(i)$ is the x_1-coordinate of the ith node, and $h(x_1(i))$ is its height ($= h_i$). This correlation gives insight in the sharpness of the surface roughness.

Figure 7.4 shows the evolution of the roughness R_{m} during nanoimprinting, unloading and relaxation and the height-height correlation functions at $t = 3$ μs. The general trend seen in Fig. 7.4a is that the roughness at maximum load increases with decreasing w. The film with $w = 1$ μm is an exception in that the elastic spring back is larger than for the other cases (see also Fig. 7.2) due to a very strong interaction between plastic zones. The height-height correlation functions after relaxation in Fig. 7.4a show a bimodal behavior: when contacts are closer together than $w = 7$ μm, the curve has a single peak, while two peaks are typical for more spaced contacts. The single peak signifies that the roughness increases with the wave length, i.e. there is a distinct central imprint with material being piled up at the borders of the unit cell. In other words, the shape of the final surface resembles a wave that has the same periodicity as the spacing between indenters w (see also Fig. 7.3d). For films with $w > 5$ μm the largest material pile-up is not located centrally between contacts but closer to the imprint.

7.3 Flattening of the rough surfaces

In this section the rough surfaces obtained by the imprinting process are compressed by a rigid flat platen. A sketch of the model is shown in Fig. 7.5. It

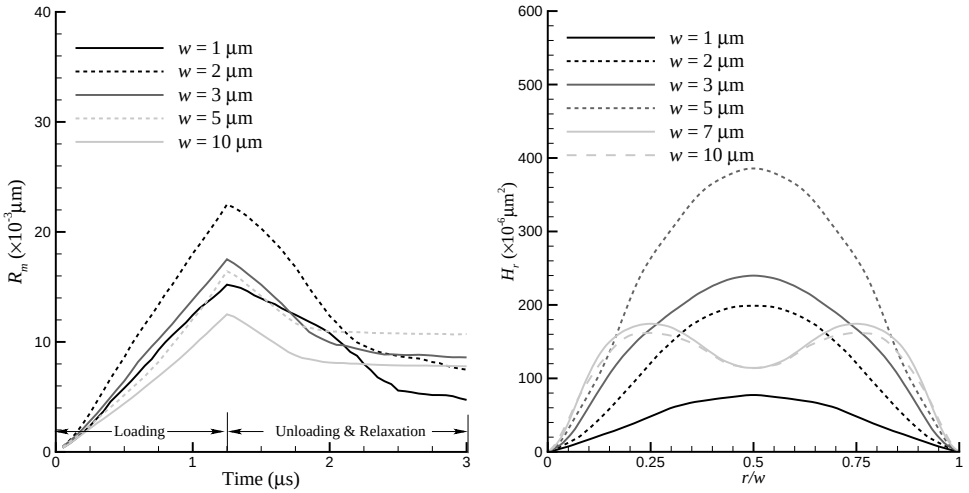

(a) (b)

Figure 7.4. (a) Roughness R_{m} during imprinting, unloading and relaxation. (b) Height-height correlation functions $H_{\mathrm{r}}(r)$ at $t = 3$ μs for films with various values of w, namely $w = 1$ μm, $w = 2$ μm, $w = 3$ μm, $w = 5$ μm and $w = 10$ μm.

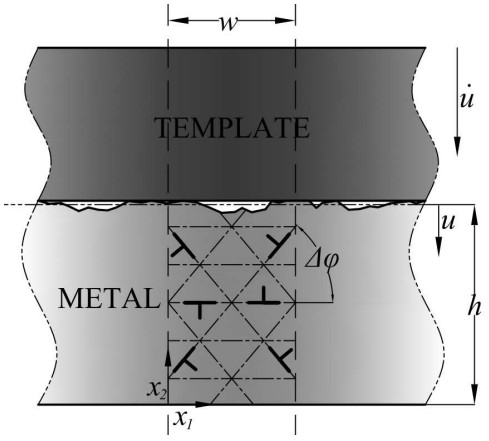

Figure 7.5. Two-dimensional model of a metal single crystal compressed by a rigid flat platen. The unit cell has the same width w as in the imprinting simulations.

is noted that the compression depth u is taken to be zero at the original film surface height (before imprinting). Therefore, the first contact between rigid platen and surface asperities occurs at negative values of u. When $u = 0$ the vertical coordinates of all surface points are smaller or equal to $h = 2$ μm. The unit cell on which the boundary conditions are prescribed has the same width w used for the imprinting simulations.

7.3.1 Contact between rough surface and rigid platen

It is recalled that imprinting was performed under sticking contact conditions. This was done to maximize the surface roughness: the constraint on unit cell expansion during imprinting is such that part of the material is squeezed upwards to create material pile-ups around the indenter. Compression is performed here for the same sticking contact conditions, but also when assuming frictionless contact between rough surface and platen. These opposite limiting conditions are chosen because of the lack of an appropriate model for the real friction conditions between the two bodies; the real behavior is expected to be in between the limiting cases treated.

To model sticking and frictionless contacts, respectively, the following boundary conditions are prescribed at the points of contact S_u between the rough surface $h(x_1)$ and the rigid flat indenter:

$$\begin{aligned} &\text{(a) perfect sticking:} \quad u_1(x_1, h(x_1)) = 0, \qquad u_2(x_1, h(x_1)) = -\int \dot{u} dt; \\ &\text{(b) frictionless:} \qquad \sigma_{12}(x_1, h(x_1)) = 0, \qquad u_2(x_1, h(x_1)) = -\int \dot{u} dt. \end{aligned} \tag{7.9}$$

The periodic boundary conditions when the contact is sticking can remain as in (7.6) but need to be changed when the contact is frictionless, since then the material can expand freely in the lateral (x_1)-direction. With reference to (Nicola et al., 2007) for details, the periodicity conditions for frictionless contacts are:

$$u_1(0, x_2) = u_1(w, x_2) + U_1 \qquad u_2(0, x_2) = u_2(w, x_2) \tag{7.10}$$

where the value of the uniform expansion U_1 is determined from the condition that lateral expansion takes place freely,

$$\frac{1}{h} \int_0^h \sigma_{11}(x_1, x_2) \mathrm{d}x_2 = 0 \qquad \forall x_1 \,. \tag{7.11}$$

7.3.2 Effect of contact conditions on flattening

A thin film that was previously imprinted by a template with $w = 2$ μm is flattened here by a rigid platen to $u = 0.05$ μm, unloaded and relaxed. The contrast in response under sticking versus frictionless contact is shown in Fig. 7.6. As shown in Fig. 7.6a, the compression force for perfect sticking boundary conditions raises steeply to about 4000 μN/μm at maximum compression. The contact area increases rapidly under sticking contact such that at $u = 0.02$ μm the contact is almost complete, as shown in Fig. 7.6b. Together with the fact that the unit cell cannot expand, a high hydrostatic pressure state is generated inside the film, which leads to the slope of the force response being close to the elastic solution. By contrast, under frictionless contact, lateral expansion allows the entire film to yield. As a consequence the contact force remains much lower (less than 300 μN/μm), resulting in a maximum contact length of only about $0.4w$.

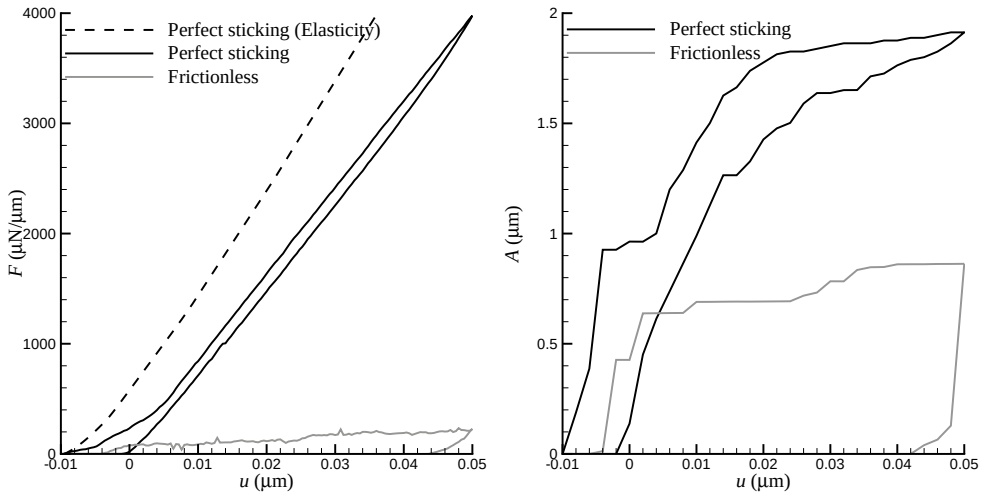

Figure 7.6. (a) Force response and (b) evolution of contact area A during compression of a previously imprinted film with $w = 2$ μm under either perfect sticking or frictionless contact.

The effect of contact conditions on the efficiency of flattening can be also seen in Figure 7.7a, which shows the profile of the initial rough surface before compression, at maximum compression depth, and in the final, unloaded and relaxed state. The top surface compressed with perfect sticking contact is

much flatter than with frictionless contacts. The sticking rigid platen is more effective in flattening out the surface asperities, Fig. 7.7b, although it requires a very high load. Also note that under these conditions, the average thickness is close to the pristine value of $h = 2$ μm, while permanent thinning of the film has occurred when flattened under frictionless conditions due to yield of the entire film. Figure 7.8 shows the evolution of the roughness R_{m} for sticking

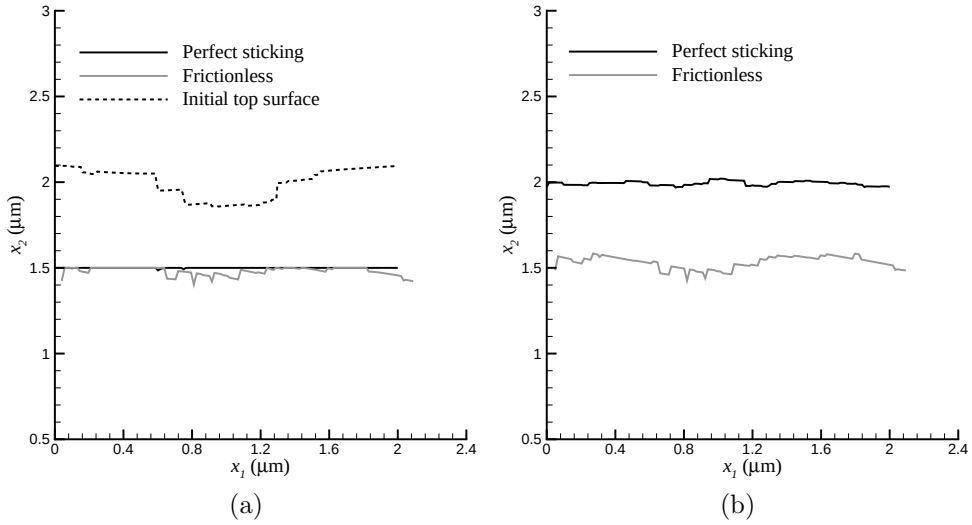

Figure 7.7. Profile of top surface of the films reported in Fig. 7.6 for different boundary conditions (a) at maximum compression depth $u = 0.05$ μm; (b) after unloading and relaxation. The vertical displacement is magnified by a factor 10.

and frictionless contact as well as the height-height correlation function $H_{\mathrm{r}}(r)$. While the roughness decreases significantly during compression when the contact is sticking, it decreases much less when the contact is frictionless. Since the contact area achieved under sticking contact at the maximum imprinting depth is larger, $A = 1.93$ μm, than that achieved under frictionless contact, $A = 0.86$ μm, we perform an additional simulation under sticking contact to also achieve a maximum contact area of $A = 0.86$ μm. The corresponding height-height correlation function is included in Fig. 7.8b. Results show that if the same contact area is achieved, i.e. for a similar flattening of the asperities, the contact conditions are not so critical in determining the roughness after unloading: $R_{\mathrm{m}} = 3.93 \times 10^{-3}$ μm for sticking and $R_{\mathrm{m}} = 3.56 \times 10^{-3}$ μm for frictionless compression. Moreover the height-height correlation functions

are closer, but have a different shape. Thus, the contact conditions affect surface evolution and topography rather significantly. With reference to Fig. 7.7 it is noteworthy that for either contact condition the topography of the final surface profiles does not show any resemblance to the original surface profiles.

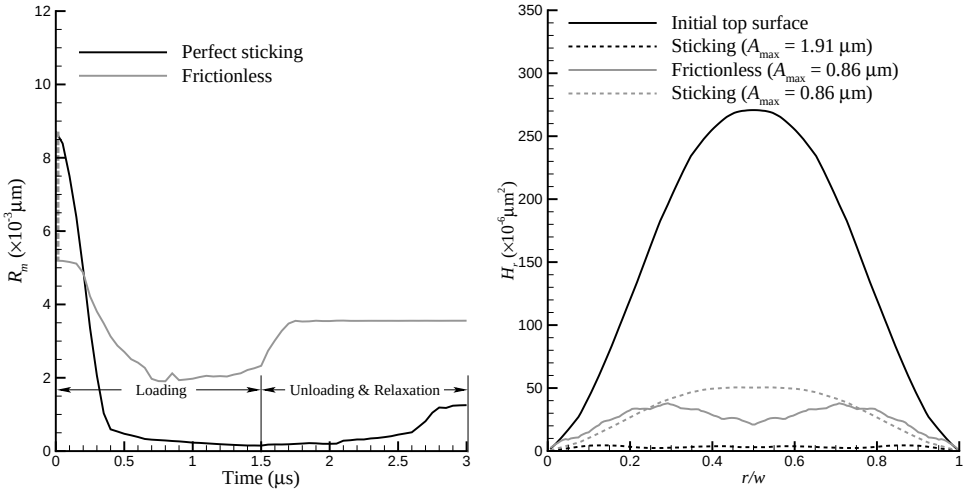

Figure 7.8. (a) The evolution of surface roughness R_{m} during compression under sticking and frictionless contacts. (b) $H_{\mathrm{r}}(r)$ after unloading and relaxation, corresponding to Fig. 7.7. The film was previously imprinted with $w = 2$ μm to $u_{\max} = 0.05$ μm.

7.3.3 Effect of loading history

The initial condition for the film studied in the previous section was equal to the final state immediately after it had been imprinted. This means that it contained the dislocations and the residual stress due to previous imprinting. This initial state could assist the flattening process, but might also obstruct it. To investigate this, we study the compression of all films imprinted in section 7.2.2 and contrast them with results obtained by compressing films with the same surface profiles but cleared of initial dislocations and residual stresses. Experimentally, this might be done, at least partly, by a heat treatment. We again consider the limiting cases of sticking and frictionless contacts.

Flattening of the surface by a sticking platen

For the case of sticking contact we will limit the maximum compression depth to $u_{\max} = 0.01$ μm to avoid the regime where unrealistic high stresses build up and the rough surface gets squashed flat completely, as was observed in Fig. 7.6. Figure 7.9 shows the evolution of compression force and contact area for the films. The films without initial dislocations and stresses consistently need a larger force to be flattened by the sticking contact. A clear trend cannot be seen in the development of contact area, i.e. the contact area for films that start dislocation- and stress-free do not systematically develop a smaller or larger real contact area with the platen. On the other hand, the evolution of surface roughness R_{m} (Fig. 7.10a) shows a connection between the presence of initial dislocations and roughness: all films that started dislocation- and stress-free are less flattened by the compression and develop a larger roughness during unloading and relaxation. It appears therefore that the presence of dislocation and stresses favours the squeezing of the aperities. The height-

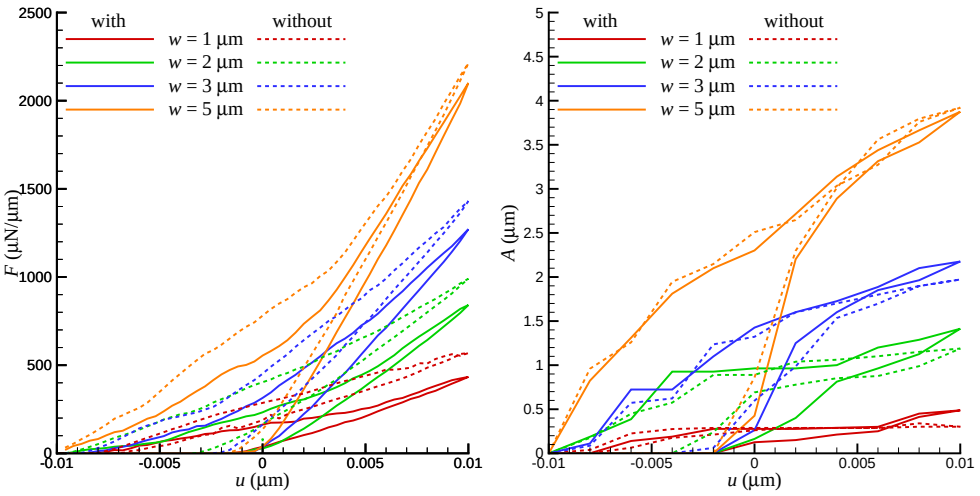

Figure 7.9. The evolution of (a) compression force F and (b) contact area A with u for sticking boundary contact between platen and rough surface in the presence of the residual dislocations and stresses (labeled 'with') and after their removal (labeled 'without').

height correlation functions in Fig. 7.10b reveal lower and broader peaks for the flattened films compared to the imprinted films (see Fig. 7.4b) for all

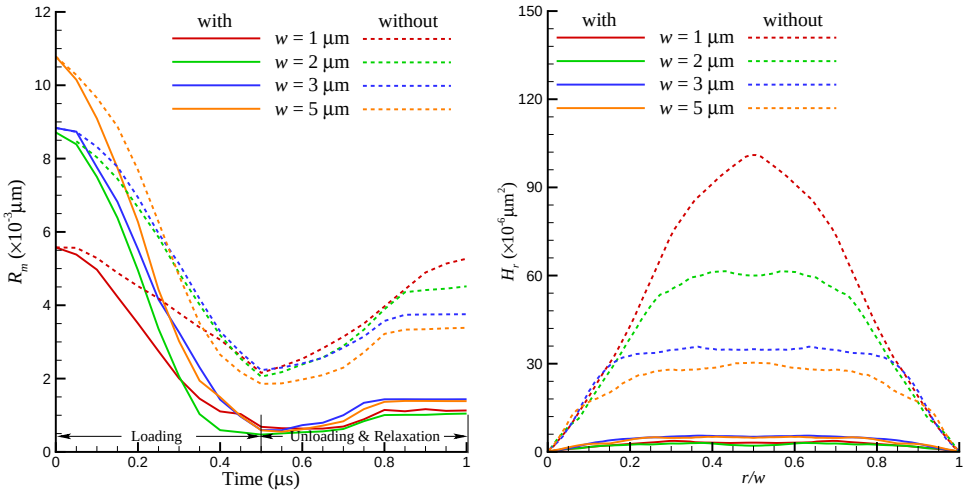

Figure 7.10. The evolution of (a) roughness R_{m} with compression time for different widths under perfect sticking contact. (b) Height-height correlation functions at the end of the process.

starting conditions. Broader peaks correspond to a more homogeneous surface roughness, which together with a lower value of R_m means a more flattened surface.

It is noteworthy that the films with the dislocations retained after imprinting have a more homogeneous surface roughness; this indicates that the flattening of the surface has been aided by the presence of dislocations. This can be better seen in Fig. 7.11, which shows the surface profiles obtained after flattening one of the films, namely the $w = 3$ μm film. The case without initial dislocations resembles the as-imprinted profile more than the case with initial dislocations. For the same film the dislocation structure before and after compression is shown in Fig. 7.12. The dislocation structure in Fig. 7.12b, which represents the film compressed from the film in Fig. 7.12a, shows little resemblance with the structure in the original as-imprinted film. During compression, the retained dislocations have left the free surface and facilitated the squeezing of the imprint. On the other hand the flattening of the film without initial dislocations in Fig. 7.12c has been more difficult; at the beginning of compression dislocations were not available to glide and by that help flattening the imprint. Only at a later stage of compression dislocations have been nucleated in the film in relation to the stress singularity at the corners of

the imprint (these dislocations are indicated by the lines in Fig. 7.12c). The evolution of the dislocation density during compression for all the films analysed can be seen in Fig. 7.13. The films with retained dislocations obviously start from a higher dislocation density, but this decreases almost monotonically during compression, unloading and relaxation. Initially dislocation-free films, however, accumulate dislocation density during compression and reach a similar density at the end of the process.

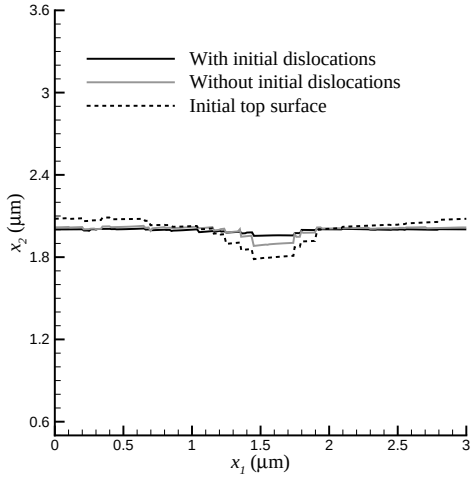

Figure 7.11. Surface profiles after compression under sticking contact conditions of the film with $w = 3$ μm.

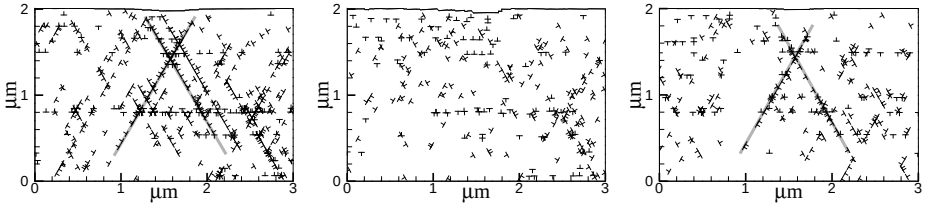

Figure 7.12. Dislocation structure in the film $w = 3$ μm (a) before and after compression for the case (b) with and (c) without initial dislocations.

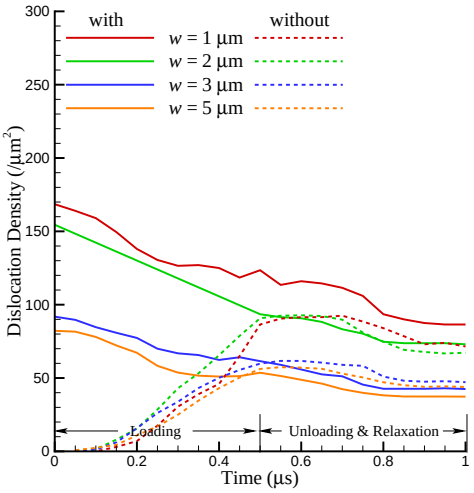

Figure 7.13. Evolution of the dislocation density in films with and without initial dislocations under sticking contact for various initial surface profiles.

Flattening rough surfaces by a frictionless platen

The imprinted films are also compressed without friction (to the same $u = 0.01$ μm). The corresponding force-displacement curves and contact area evolution are shown in Fig. 7.14. Films with the same profile but different history –i.e. with or without initial dislocations and stresses– exhibit different force displacement curves, i.e. the presence of initial dislocations gives rise to a softer response. A similar trend cannot be seen in the evolution of the contact area, which appears to depend on starting conditions but without a clear tendency. These observations are qualitatively similar to those made in the previous subsection on sticking contacts. Also consistent with the results obtained with sticking conditions, the change in roughness R_{m} during compression and the height-height correlation functions at the end of the process, presented in Fig. 7.15, show how for each film the flattening process is facilitated by the presence of dislocations retained by the imprinting process. Differently from the cases with sticking contact, though, all films with retained dislocations are not flatter than the initially dislocation-free films. Moreover, the difference in roughness between the films with and without retained dislocations is lower than for the sticking contact. A smaller influence of the loading history can be seen also by contrasting the final profiles for the film with $w = 3$ μm, Fig. 7.16a, with those for the same films under sticking com-

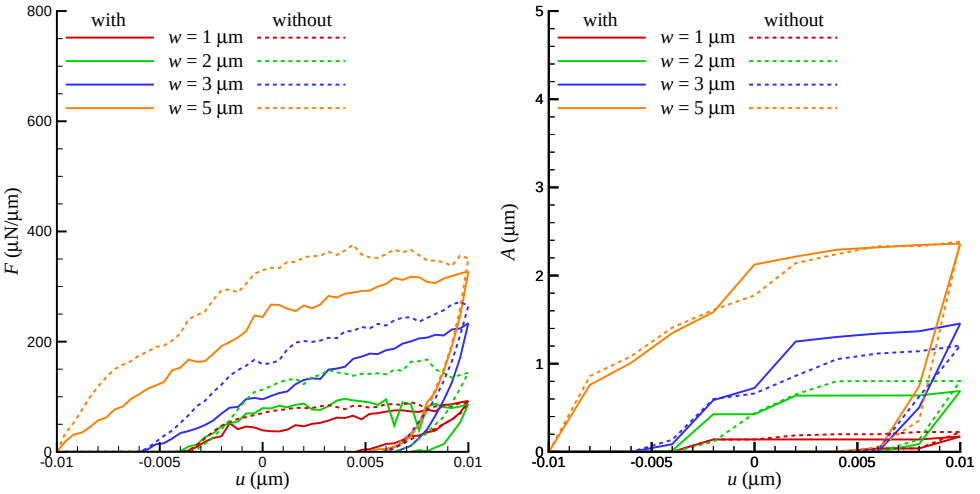

Figure 7.14. The evolution of (a) compression force F; (b) contact area A with compression depth u for different widths under frictionless contact. The maximum indentation depth is $u = 0.01$ μm.

pression in Fig 7.11. The dislocation density in Fig. 7.16b for the films with retained dislocations decreases less during the process than that for the sticking contact in Fig. 7.13. All the observations lead to the conclusion that the presence of retained dislocations aid the flattening of asperities compressed under all friction conditions, but the effect is smaller if there is no friction.

The situation changes slightly when the films are flattened to a larger compression depth, i.e. $u = 0.05$ μm. Both the change in roughness R_{m} during compression and the height-height correlation functions at the end of the process, presented in Fig. 7.17, have lost their dependence on the presence or absence of initial dislocations. For all films, the final surface roughness is rather homogeneous, as indicated by the broad height-height correlation functions. Thus, under frictionless contact the presence of initial dislocations does facilitate flattening of the surface only at smaller compression depths, when the contact area is about one third of the surface area. When the contact area becomes larger, the film is subjected to a uniform compression which leads to yielding of the metal and a much higher and less localized dislocation activity. Consequently, the dislocation density peaks at maximum compression depth, as seen in Fig. 7.18. This is consistent with the observation in Fig. 7.6 that with these contact conditions, the film can yield as a whole.

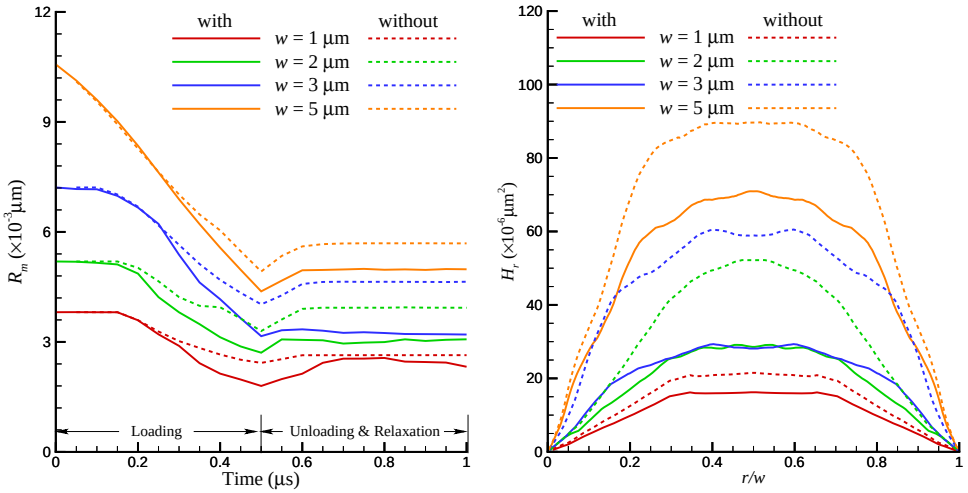

Figure 7.15. (a) Roughness evolution with frictionless compression of pre-imprinted films with and without initial dislocations. (b) $H_{\mathrm{r}}(r)$ after unloading and relaxation ($t = 3$ μs). The maximum indentation depth is $u = 0.01$ μm.

The reader is reminded here that in the simulations dislocation nucleation occured from Frank-Read sources and that nucleation of dislocations from surface steps was not considered. Also, geometry changes were not accounted for other than in the evolution of the contact area. It is forseeable that if the model would be improved by including geometry changes and dislocation nucleation from the surface, a larger density of glide planes would be activated and the final surface profile would be smoother. This is expected especially in the case of frictionless contact. However, the effect of retained dislocations gliding and aiding the flattening is not expected to be reduced.

7.4 Conclusions

We have performed discrete dislocation plasticity simulations of the flattening of surface roughness obtained by nanoimprinting thin metal films. The imprinting simulations have shown that the imprints are much wider than the indenters that produced them. The shape of the indents is determined primarily by the density of dislocation sources. The metal surface in between imprints is also affected by the dislocation activity, namely through disloca-

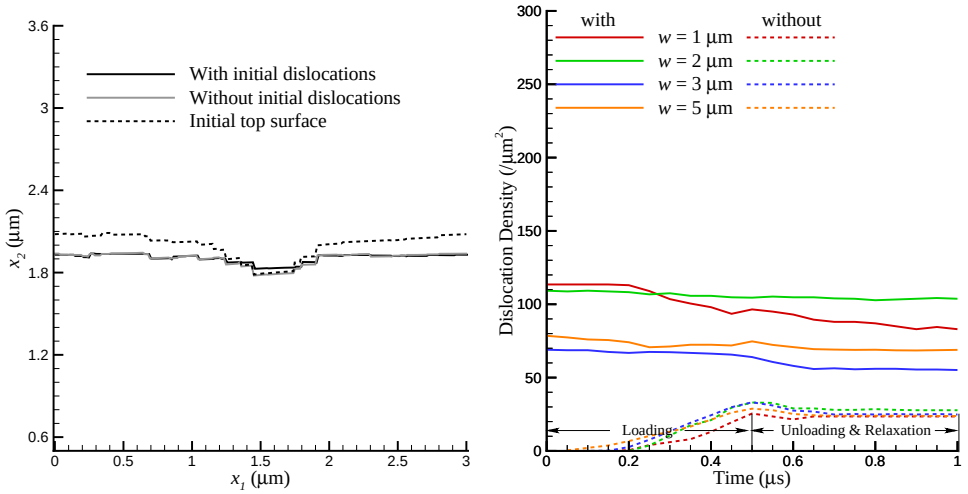

Figure 7.16. (a) Final profiles for the $w = 3$ μm film and (b) evolution of dislocation density during compression and relaxation of films flattened by a frictionless contact to $u = 0.01$ μm.

tions that exit the metal thus leaving rather pronounced displacement steps at the surface. Also, the interaction between neighboring plastic zones contributes to the final roughness of the surface. Specifically, surfaces indented by contacts that are closer than the material dependent length of $w = 7$ μm exhibit squeezing-up of material in the region between neighboring indents. In other words, the shape of the final surface resembles a wave that has the same periodicity of the spacing between indenters w.

Flattening of the films has been achieved by compressing the rough surface obtained by nanoimprinting using both frictionless and sticking contact conditions. The results differ quite significantly when the surfaces are flattened to the same depth (which corresponds to a rather different contact area): the sticking contact leads to a more pronounced flattening of the surface asperities, albeit at a much higher contact pressure.

The focus of this study has been on contrasting the behavior of the as-imprinted film surfaces –with stresses and dislocations produced by the nanoimprinting process– with those of films with the same surface profiles but freed of dislocations and stresses. For both sticking and frictionless contact, and for compression depths that cause only partial flattening of the surface, the evolution of the surface topography depends strongly on the loading history,

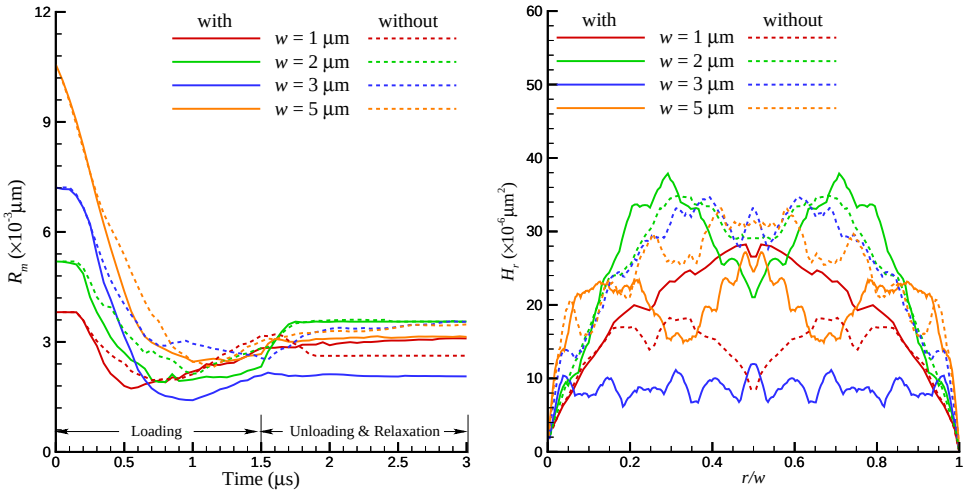

Figure 7.17. (a) Roughness evolution with frictionless compression down to $u = 0.05$ μm of pre-imprinted films with and without initial dislocations. (b) $H_{\mathrm{r}}(r)$ after unloading and relaxation ($t = 3$ μs).

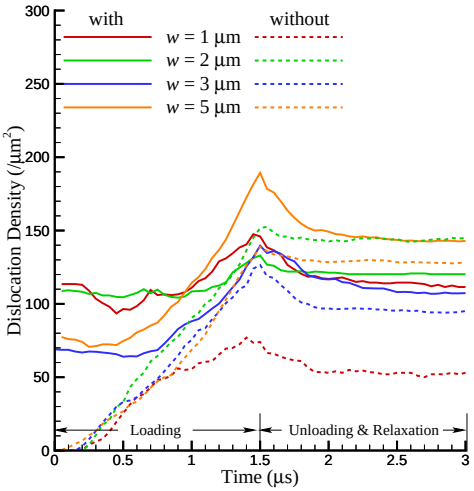

Figure 7.18. Evolution of dislocation density during compression and relaxation of films flattened by a frictionless contact down to $u = 0.05$ μm.

i.e. the presence or absence of dislocations retained during imprinting. More precisely, the presence of initial dislocation favours the squeezing of asperities. This observation is obviously not sufficient to claim that the presence of dislocations in the subsurface region favors flattening of the asperities in general, since the dislocation structure created during imprinting is characteristic of this specific deformation process only. On the other hand it can be concluded that the loading history strongly affects the deformation of the surface profile during contact. This indicates that an accurate description of the surface profile is not sufficient to predict initial deformation of the surface during contact of rough surfaces, independently of friction conditions. Therefore, models that aim at predicting rough surface evolution should not only strive to a precise description of the rough surface, but also acquire a similarly accurate knowledge of subsurface dislocation structure.

Acknowledgement

LN is grateful to the Dutch National Scientific Foundation NWO and Dutch Technology Foundation STW for their financial support (VENI grant 08120).

References

Bakolas, V., 2003. Numerical generation of arbitrarily oriented non-gaussian three–dimensional rough surfaces. Wear 254, 546–554.

Ciavarella, M., Delfine, G., Demelio, G., 2006. A revitalized greenwood and williamson model of elastic contact between fractal surfaces. J. Mech. Phys. Solids 54, 2569–2591.

Gao, Y.F., Bower, A.F., 2006. Elastic-plastic contact of a rough surface with weierstrass profile. Proc. R. Soc. London, Ser. A 462, 319–348.

Greenwood, J.A., Williamson, J.B.P., 1966. Contact of nominally flat surfaces. Proc. R. Soc. London, Ser. A 295, 300–319.

Jackson, R.L., Green, I., 2006. A statistical model of elasto-plastic asperity contact between rough surfaces. Tribol. Int. 39, 906–914.

Majumdar, A., Bhushan, B., 1991. Fractal model of elastic-plastic contact between rough surfaces. J. Tribol. 113, 1–11.

Nicola, L., Bower, A.F., Kim, K.S., Needleman, A., Van der Giessen, E., 2007. Surface versus bulk nucleation of dislocations during contact. J. Mech. Phys. Solids 55, 1120–1144.

Nicola, L., Bower, A.F., Kim, K.S., Needleman, A., Van der Giessen, E., 2008. Multi-asperity contact: A comparison between discrete dislocation and crystal plasticity predictions. Philos. Mag. 88, 3713–3729.

Nicola, L., Van der Giessen, E., Needleman, A., 2004. Relaxation of thermal stress by dislocation motion in passivated metal interconnects. J. Mater. Res. 19, 1216–1226.

Patir, N., 1978. A numerical procedure for random generation of rough surfaces. Wear 47, 263–277.

Rice, J.R., 1987. Tensile crack tip fields in elastic-ideally plastic crystals. Mech. Mater. 6, 317–323.

Van der Giessen, E., Needleman, A., 1995. Discrete dislocation plasticity: a simple planar model. Modell. Simul. Mater. Sci. Eng. 3, 689–735.

Wilson, W.E., Angadi, S.W., Jackson, R.L., 2009. Surface separation and contact resistance considering sinusoidal elastic-plastic multi-scale rough surface contact. Wear 268, 190–201.

Wu, J.J., 2000. Simulation of rough surfaces with fft. Tribol. Int. 33, 47–58.

Yan, W., Komvopoulos, K., 1998. Contact analysis of elastic-plastic fractal surfaces. J. Appl. Phys. 84, 3617–3624.

Summary and conclusions

This thesis addresses the feasibility of a new nanotechnology, direct metal nanoimprinting. The main aim of this work is to investigate, by means of computer simulations, the possibility to create reproducible patterns in a metal layer by plastically deforming it with a rigid template.

Chapter 2 presents a direct comparison between nanoimprinting experiments and discrete dislocation plasticity simulations. A gold single crystal is imprinted by a template made of differently spaced tungsten lines. The combination of experiments and simulations demonstrates that good pattern transfer can be achieved when 200 nm wide lines are spaced from each other at a distance of about 1 μm. If the lines are closer to each other, individual imprints cannot be retained and the lines act as a single wide indenter. The reason for this behavior is the discrete nature of dislocations and dislocation sources and their limited availability at the sub-micron scale. Even when lines are sufficiently spaced to leave imprints, the edges of the obtained grooves are not smooth but stepped, due to dislocations gliding out of the edges and leaving displacement steps at the surface.

Chapter 3 is devoted to investigate the effect on imprinting of the interface between the metal film and the substrate on which it is coated. Two limiting situations are considered: the interface is either perfectly penetrable or impenetrable to dislocations. Interface conditions between film and substrate are found to be essential in determining the success of the imprinting process: if the interface is perfectly penetrable to dislocation motion the retained imprints are the deepest achievable. Thus, to the end of creating well-defined nanopatterns, an interface that absorbes dislocations is clearly the preferable choice.

The effect of template shape is investigated in Chapter 4. Thin films are imprinted by a rigid template, made of an array of equispaced indenters of various shape, i.e. rectangular, wedge and circular. The geometry of the indenters is chosen such that the contact area is approximately the same at final imprinting depth. Results show that rectangular indenters require the lowest imprinting force and achieve the deepest retained imprints. Nevertheless for all template shapes the final patterns strongly depend on the dislocation activity and each imprint differs from the neighboring ones. Material pile-

ups between indents are very pronounced. It appears therefore not possible to transfer a specific template shape at the submicron scale to the metal by plastic deformation only.

An analysis of metal nanoimprinting when the template is patterned with lines as small as a few nanometers is presented in Chapter 5. The problem is addressed by molecular dynamics simulations and the main findings are rather unexpected: many simulations show a competition between dislocation motion and crack formation upon retraction of the template. The most interesting finding is that this competition, for certain loading conditions and geometry of the crystals, is driven by thermal fluctuations of the atomic velocities. Local events, namely atomic fluctuations and dislocation nucleation, determine the global mechanical response of the system, i.e. whether an imprint is obtained or not. The relevance of thermal fluctuations is confirmed by the fact that any of the simulations presented in the chapter, if repeated at 10 K, leads to a brittle material behavior.

Chapter 6 is an analysis of wedge indentation. Attention centers on the relation between the lattice rotation fields caused by the indenter and the size dependent material hardness. The question is whether or not the lattice rotation sectors, that can nowadays be measured experimentally, and that are related to the density of geometrically necessary dislocations, can be directly related to the hardness. This study is carried out by means of discrete dislocation plasticity simulations, for which the indentation size effect is expected to have similar origin to that observed experimentally. The hardness in the simulations is found to be affected only minorly by dislocation obstacles. However, the formation of the lattice rotation sectors is found to be controlled by obstacles. As a conclusion, in discrete dislocation plasticity simulations the lattice rotation sectors have no correspondence with the hardness and therefore with the indentation size effect. Assuming that DDP is indeed capable of capturing all mechanisms that cause an indentation size effect in experiments, also the lattice rotation measured experimentally cannot be related to the indentation size effect. The lattice rotation sectors measured experimentally can be coupled to material hardness only at a sufficiently large indentation depth, where hardness is size independent.

Chapter 7 has a different focus compared to previous chapters: it deals with the plastic behavior of an imprinted metal surface during contact loading. As observed in previous chapters, direct nanoimprinting leads to a pattern but also to irregular surface roughness caused by dislocation glide. Surface roughness plays a crucial role during metal forming processes, since it controls the friction properties until the moment that possibly all asperities are flattened.

The goal of this study is to understand to which extent the loading history and the presence of dislocations affects deformation and surface roughness during contact loading. The contact is taken to be either sticking or frictionless. Results show that when the imprinted surface is flattened such that the contact area is up to about one third of the surface area, the loading history strongly affects the flattening. Specifically, the presence of initial dislocations facilitates the squeezing of asperities independently of the friction conditions of the contact. For larger contact areas, the initial conditions affect only sticking contacts, while frictionless contacts lead to a homogeneous flattening of the asperities due to yield of the metal film. In all cases studied the final surface profile obtained after flattening has little to no resemblance with the original imprinted surface.

Samenvatting en conclusies

Deze dissertatie behandelt de geschiktheid van een nieuwe nanotechnologie: het direct nanoimprinten van metaal. Het hoofddoel van dit werk is door middel van computersimulaties de mogelijkheid te onderzoeken om, gebruikmakend van een onvervormbaar indenter sjabloon ('template'), door plastische deformatie reproduceerbare patronen te creëren in een metaallaag.

In hoofdstuk 2 wordt een directe vergelijking gemaakt tussen nanoimprinting experimenten en discrete dislocatie plasticiteit (DDP) simulaties. Het imprinten van een goudkristal gebeurt door middel van een sjabloon bestaand uit wolfraam lijnen met verschillende onderlinge afstand. Een vergelijking van experimenten en simulaties toont aan dat een goede patroonoverdracht kan worden bereikt met een sjabloon met 200 nm dikke lijnen en een onderlinge afstand van circa 1 μm. Wanneer de onderlinge afstand kleiner is, blijven de individuele imprints niet behouden en gedragen de lijnen zich als een enkelvoudige, brede indenter. De reden hiervoor is het discrete karakter van dislocaties en dislocatiebronnen en de beperkte beschikbaarheid hiervan op sub-micronschaal. Zelfs wanneer de onderlinge afstand van de lijnen voldoende is om imprints achter te laten, zijn de hoeken van de verkregen groeven niet glad maar vertonen ze stappen door de dislocaties die in de hoeken uit het materiaal bewegen en hierbij het oppervlak stapsgewijs veranderen.

Hoofdstuk 3 is gewijd aan het effect van het interface tussen de metaalfilm en het substraat op het imprinten. Twee uiterste situaties zijn bekeken: het interface is ofwel volledig doordringbaar ofwel volledig ondoordringbaar voor dislocaties. De interfacecondities blijken essentieel te zijn voor het succes van het imprintingproces: wanneer het interface volledig doordringbaar is voor dislocaties, zijn de verkregen imprints op hun diepst. Hieruit volgt dat om een goed gedefinieerd nanopatroon te creëren een interface dat dislocaties absorbeert duidelijk de voorkeur heeft.

Het effect van de sjabloonvorm is onderzocht in hoofdstuk 4. Dunne films worden imprinted door een onvervormbaar sjabloon bestaande uit een gelijkgespatieerde array indenters. Verschillende indentervormen zijn bekeken, namelijk rechthoekig, wigvormig en rond. De geometrie van de indenters is zo gekozen dat de contactoppervlakken op de uiteindelijke imprintdiepte bij benadering gelijk zijn. De resultaten laten zien dat rechthoekige indenters

een lagere imprintingkracht nodig hebben en de diepste blijvende imprints veroorzaken. Voor alle sjabloonvormen zijn de uiteindelijke patronen echter sterk afhankelijk van de dislocatieactiviteit en verschilt iedere imprint van de naastgelegen imprints. Materiaalophoping tussen imprints is significant. Het lijkt daarom niet mogelijk te zijn om een specifieke sjabloonvorm over te brengen naar het metaal door plastische deformatie op sub-micron schaal.

Hoofdstuk 5 analyseert metaal-nanoimprinting waarbij de sjabloon een patroon met lijnen van enkele nanometers breed heeft. Het onderwerp is bestudeerd met behulp van moleculaire dynamica-simulaties en de belangrijkste resultaten zijn tamelijk onverwacht: veel simulaties laten een competitie zien tussen dislocatiebeweging en scheurvorming tijdens het terugtrekken van de sjabloon. Het interessantste verschijnsel is dat deze competitie voor zekere belastingcondities en kristalgeometrieën sterk door thermische fluctuaties van de atomaire snelheden wordt beïnvloed. Lokale grootheden, voornamelijk snelheidsfluctuaties en dislocatienucleatie, blijken de uiteindelijke mechanische respons van het systeem, namelijk of wel of niet een imprint wordt verkregen, te bepalen. De relevantie van thermische fluctuaties hierin wordt bevestigd door het effect van temperatuurverandering: wanneer iedere simulatie van dit hoofdstuk herhaald wordt op een zeer lage temperatuur (10 K), wordt een bros materiaalgedrag gevonden: scheurgroei wint het systematisch van plastische deformatie en blijvende imprints worden altijd verkregen.

In hoofdstuk 6 wordt wigvormige indentatie onderzocht. De aandacht gaat uit naar de relatie tussen roosterrotatievelden veroorzaakt door de indenter en de grootteafhankelijke materiaalhardheid. De vraag is of de roosterrotatiesectoren, die tegenwoordig experimenteel gemeten kunnen worden en samenhangen met de GND-dichtheid (geometrisch noodzakelijke dislocaties), direct gerelateerd kunnen worden aan de hardheid. Deze studie is gedaan met behulp van DDP-simulaties, waarin volgens verwachting de grootteafhankelijkheid van de indentatie dezelfde zal zijn als de experimenteel waargenomen. De resultaten van de simulaties tonen aan dat de hardheid slechts voor een klein deel beïnvloed wordt door dislocatieobstakels. Echter, de formatie van de roosterrotatiesectoren blijkt wel bepaald te worden door obstakels. Hieruit volgt dat in DDP-simulaties de roosterrotatiesectoren niet corresponderen met de hardheid en dus ook niet met de grootteafhankelijkheid van indentatie. Uitgaande van de aanname dat DDP daadwerkelijk in staat is om alle mechanismen te beschrijven die grootte-afhankelijkheid van indentatie in experimenten veroorzaken, kan de experimenteel gemeten roosterrotatie niet gerelateerd zijn aan de grootteafhankelijkheid van indentatie. De experimenteel gemeten roosterrotatiesectoren kunnen alleen gekoppeld worden aan de mate-

riaalhardheid op een voldoend grote indentatiediepte, waar hardheid grootte-onafhankelijk is.

Hoofdstuk 7 heeft een andere focus dan de eerdere hoofdstukken: het behandelt het plastische gedrag van een imprinted metaaloppervlak gedurende contactbelasting. Zoals geconcludeerd in de eerdere hoofdstukken wordt door rechtstreekse nanoimprinting een patroon verkregen, maar wordt ook onregelmatige oppervlakteruwheid veroorzaakt door dislocaties. Oppervlakteruwheid speelt een cruciale rol in metaalvormingprocessen, aangezien het de wrijvingseigenschappen verandert totdat de oneffenheden ('asperities') die de ruwheid veroorzaken zijn afgevlakt.

Het doel van deze studie is om te begrijpen in hoeverre de mechanische belasting in het verleden en de aanwezigheid van dislocaties de deformatie en oppervlakteruwheid beïnvloeden tijdens contactbelasting. Het contact wordt daarbij verondersteld ofwel volledig adhesief ofwel wrijvingsloos te zijn. De resultaten laten zien dat wanneer het imprinted oppervlak dusdanig is afgevlakt dat het contactoppervlak circa een derde van het totale oppervlak bedraagt, de belastinggeschiedenis de afvlakking sterk beïnvloedt. Meer specifiek gesteld, de aanwezigheid van initiële dislocaties faciliteert het samenpersen van de oneffenheden onafhankelijk van de wrijvingscondities in het contact. Voor een groter contactoppervlak is de materiaalrespons uitsluitend afhankelijk van de initiële condities voor perfect adhesieve contacten, terwijl wrijvingsloze contacten leiden tot homogene afvlakking van de oneffenheden veroorzaakt door het plastisch deformeren van de metaalfilm. In alle bestudeerde situaties heeft het uiteindelijke oppervlakteprofiel na afvlakking weinig tot geen overeenkomst meer met het originele imprinted oppervlak.

Acknowledgements

When I begin to write this acknowledgement I suddenly realize there are so many friends having helped me.

Firstly, I want to send my sincere appreciations to my daily supervisor, Dr. Nicola Lucia. You spent a lot time on supervising my project. Thanks for your patience and your suggestions during our daily discussions. I had a very pleasant and enjoyable cooperation with you during my four-year PhD research. I also want to thank my current promoter Prof. dr. Barend J. Thijsse. You helped me a lot in my last paper on molecular dynamics simulation, which is included as Chapter 5 in this thesis. You also gave me a lot of helpful suggestions on my PhD thesis.

I am very grateful to the contribution of Jiangnan Zhang and Dr. Jun Lou from Rice University, and Dr. Nathan A. Mara from Los Alamos National Laboratory on the experimental part in Chapter 2. Your excellent job provides a strong support to my following simulation research on nanoimprinting.

I am grateful to the advises of Prof. dr. Erik Van der Giessen from University of Groningen on Chapter 7. Your wise suggestions helped me finishing my first journal publication.

I am also grateful to Dr. Yanfei Gao from University of Tennessee. You proposed the attractive topic on lattice rotation in Chapter 6 and worked together with us for the publication.

I want to extend my deep gratitude to my friend Dr. Liliang Wang. I came to the Netherlands on the early Christmas when most of the people were in holiday. You helped me quickly adapting the new life and starting my project.

I am so pleased to be able to have a helpful discussion with my colleagues Fengwei Sun, Kelvin Wei Siang Ng, Robert-Jan Dikken, and Sebastian Echeverri Restrepo when I drop in troubles in my research. I appreciate your brilliant suggestions. Thanks for my initial promoter, Prof. dr. Ian Richardson. You gave me an initial impression on a successful PhD candidate. I also want to thank the warm and friendly helps from Dr. Chuangxin Zhao, Dr. Marcel J. M. Hermans, Dr. Murugaiyan Amirthalingam, and Dr. Vera Popovich on my daily researching work. You provided many professional advices to me. Especially, I am grateful to our secretaries Anneke van Veen and Anke Kerklaan-koene. My researching activities became much more convenient un-

der your aids.

I want to thank for my PhD friends Dr. Anand Ramasamy, Bo Song, Dr. Guoliang Zhu, Dr. Haiyang Cui, He Gao, Dr. Hua Zhong, Junchao Shi, Dr. Liang Zhang, Masoud Akbari Pazooki, Meng Wang, Dr. Yu Pan, Dr. Yue Chen, Dr. Qiang Xu, Dr. Qingshi Song, Weihai Yuan, Dr. Yingxia Qu, Dr. Yuan Ren, and Dr. Zhan Zhang. Thank you for your suggestions on my publications and your helps on my life. I also want to thank the helps from my friends Boya Dai, Chenxiang Ning, Jing Chu, Xiaochen Liu, Xinan Zhu, Yaxun Wu.

I have experienced some tough time during my PhD research. I am grateful to the support from my parents. Their understanding and encouragement are the best plasebo to release my stress.

I also want to thank Miss Mimi (a cat). You accompanied me every night and never left me alone.

Finally, I want to give my thanks to my soccer teammates. We share the best time on the playground after work. My apologies for being unable to list all your names here.

Curriculum Vitae

Personal information

Name	Yunhe Zhang
Birthday	25–08–1983
Place of birth	Tianjin, China

Education

2008–2012, Ph.D candidate in Material Science

Delft University of Technology, Delft, The Netherlands, Faculty of Mechanical, Maritime and Materials Engineering, Group of Virtual Materials and Mechanics

Project: "Modelling of metal nanoimprinting"

supervisor: Barend Thijsse, Lucia Nicola

2006–2008, M.Sc in Solid Mechanics

Zhejiang University, China, Faculty of Aeronautics and Astronautics, Department of Mechanics, Center for Engineering and Scientific Computation

Thesis: "Study of the vibration behaviors of the stiffened shell and plane structure"

supervisor: Yao Zheng, Jifa Zhang

2002–2006, B.Sc in Solid Mechanics

Zhejiang University, China, Faculty of Mechanical and Energy Engineering, Department of Mechanics

Thesis: "Simulation of metal cutting using finite element and study of the separation criteria"

supervisor: Chongyang Gao

Publications

- Y. Zhang, E. Van der Giessen and L. Nicola, Dislocation dynamic simulations of metal nanoimprinting, 2009 MRS Fall Meeting
- Y. Zhang, E. Van der Giessen and L. Nicola, Discrete dislocation simulations of the flattening of nanoimprinted surfaces, Modelling and Simulation in Materials Science and Engineering 18 (2010) 034006
- Y. Zhang and L. Nicola, Effect of template shape on metal nanoimprinting: a dislocation dynamics study, Journal of Zhejiang University-Science A 11 (2010) 722-726
- J. Zhang, Y. Zhang, N.A. Mara, J. Lou, L. Nicola. Direct nanoimprinting of single crystalline gold: experiments and dislocation dynamics simulations, Applied Surface Science 290 (2014) 301-307
- Y. Zhang, Y. Gao and L. Nicola. Lattice rotation caused by wedge indentation of a single crystal: dislocation dynamics compared to crystal plasticity simulations. Journal of the Mechanics and Physics of Solids (accepted)
- Y. Zhang, B. Thijsse and L. Nicola. Competition between dislocations and cracks in molecular dynamics simulations of metal nanoimprinting. Computational Materials Science (accepted)
- L. Wang, Y. He, Y. Zhang, J. Cai, J. Zhou, J. Duszczyk and L. Katgerman, Modeling of double action extrusion-a novel extrusion process for friction characterization at the billetdie bearing interface, Tribology International 43 (2010) 2084-2091